Hydrodynamic Interactions among Ships Moving in a Single-File Formation

PhD Thesis

Fengshen Zhu

Hydrodynamics & Ocean Renewable Laboratory
Department of Naval Architecture, Ocean & Marine Engineering
University of Strathclyde, Glasgow

February 11, 2025

Abstract

To minimize energy expenditure for each individual, animals adopt distinctive formations, such as fish schooling, 'V' formation by flying birds, and single-file formation by waterfowls. The phenomenon of ducklings following their mothers in a single-file configuration has been revealed by the mechanism of wave-riding and wave-passing. Drawing inspiration from this phenomenon, an investigation is undertaken on ships moving in a single-file formation. This thesis explores two scenarios: ships advancing on calm water without connections and ships advancing in waves with connections (marine trains). An in-house code, MHydro, based on potential flow theory, is developed to analyze the wave-making and seakeeping problems. Additionally, a series of experimental tests are conducted to investigate the complex interference between ships moving on calm water.

Firstly, the wave drag and wave patterns of ships in a single-file formation on calm water are examined using MHydro. It is found that when constructive wave interference occurs in a two-ship formation, the wave resistance of the trailing ship increases and the leading ship experiences a decrease in its wave drag, especially when the two ships are in close proximity. Mutual benefit arises when destructive wave interference occurs between two ships. In addition, increasing the size of the trailing vessel facilitates the effect of wave-riding by leading ship, but this effect becomes less pronounced as the speed increases. In a multi-ship formation configuration, changing the size of the leading ship will have a localized effect on the wave-passing, but the fleet will eventually tend to a dynamic equilibrium. When the position of the first trailing vessel is changed, there is similarly a localized effect on the wave-passing. Adjusting the first trailing ship to the position of the constructive wave interference is not favorable to reduce its own drag but enhances the wave-riding effect of its close follower. Finally, to achieve wave-passing, the trailing ship does not necessarily have to occupy an optimum position. This can still be accomplished if the trailing ship moves backward by an integer multiple of wavelength.

Next, a series of experiments are conducted to measure the total resistance of ships moving individually and in two-ship formations on calm water. The results indicate that the form of the bow has a more significant impact on the total resistance of single ships than the form of the stern. Specifically, the total resistance of a single ship with a transom stern is nearly identical to that of a ship with a sharp stern. However, ships with a flat bow exhibit significantly higher total resistance compared to those with a sharp bow. In a two-ship formation, the hydrodynamic pressure resistance of both the leading and trailing ships is significantly reduced when the gap between the two ships is small. This reduction occurs because the air hollow created by flow separation is filled by the bow waves of the trailing ship. When the trailing ship is positioned in the divergent-wave zone within the wake of the leading ship, wave interference between the two ships becomes the dominant factor influencing the variance in the total resistance of the trailing ship. As the gap between the two ships increases further, the wave interference weakens; however, the trailing ship still experiences a substantial reduction in resistance due to weakened flow separation and bubble drag reduction within the turbulent-bubble mixed flow region.

Finally, the hydrodynamic responses of marine trains—ships connected together in a single-file formation—advancing in waves are investigated numerically. The sliding-hinged connection is found to be the most suitable for marine trains, as it effectively avoids high vertical shear forces compared to rigid or hinged connections. Additionally, this connection type enables the entire ship formation to be powered by the leading ship. For marine trains consisting of five ships, the motion responses in heave and pitch increase significantly as the advancing speed increases. Changing the horizontal positions of the joints has minimal effect on the motion responses of each ship. Similarly, adjusting the gaps between the ships has a small impact on the motion responses from an engineering perspective, as the gaps between ships are generally not large.

Contents

List of Figures

List of Tables

List of Nomenclatures

Abbreviations

ACDR	Air Cavity Drag Reduction
ADC	Analog-to-digital converter
ALDR	Air Layer Drag Reduction
AUV	Autonomous Underwater Vehicle
BDR	Bubble Drag Reduction
BEM	Boundary Element Method
CFD	Computational Fluid Dynamics
IHVDT	Incompressible Highly Variable Density Turbulence
iLES	Implicit Large Eddy Simulation
LCM	Longitudinal-Cut Method
RANS	Reynolds-Averaged Navier-Stokes
RAO	Response amplitude operators
TBL	Turbulent Boundary Layer
TMF	Turbulent Mass Flux
URANS	Unsteady Reynolds-averaged Navier-Stokes

USV	Unmanned Surface Vehicle
WEC	Wave Energy Converter

Greek Letters

η_j	Radiation wave amplitude
λ	Wavelength
ν	Kinematic viscosity
η_0	Incident wave amplitude
ω_0	Incident wave frequency
ω_e	Encounter wave frequency
ρ	Water density
φ_0	Incident velocity potential
φ_7	Diffraction velocity potential
φ_j	Radiation velocity potential
ζ	Wave elevation
η_7	Diffraction wave amplitude
τ	Brard number
β	Wave direction
φ	Velocity potential

Roman Symbols

C_{DR}^T	Total drag reduction coefficient
F_r	Froude number

k_{yy}	Radius of inertia for pitch
KG	Centre of gravity above base
KR	Centre of rotation above base
Re	Reynolds number
V	Displacement
$\mathbf{K}$	Restoring matrix
$\mathbf{M}$	Generalised mass matrix
$\mathbf{n}$	Unit normal vector
g	Gravitational acceleration
c	Wave velocity
F_{coj}	Internal constraint force
F_{exj}	Wave excitation force
h	Water depth
k	Wave number
C_W	Wave-making resistance coefficient
C_{AA}	Air resistance coefficient
C_{DR}	Wave drag reduction coefficient
C_F	Frictional resistance coefficient
C_T^s	Total resistance coefficient
D	Constraint matrix
F_T	Draft Froude number

R_F	Frictional resistance
R_s	Wave-making resistance
S	Wetted body surface
B	Breadth of the ship
L	Length of the ship
T	Draught of the ship
U	Advancing speed

List of Publications

Journal Articles

1. **Zhu, F.**, Yuan, Z.* (2024). Wave drag and wave patterns by ships moving in a single-file formation. *Physics of Fluids*. DOI: 10.1063/5.0210836. (Based on Chapter 4 of this thesis)

2. **Zhu, F.**, Dai S., Yuan, Z.*. Resistance experiments on ships in a leader-follower formation. *Physics of Fluids*, DOI: 10.1063/5.0249171. (Based on Chapter 5 of this thesis)

Conference papers

1. **Zhu, F.**, Yuan, Z.* (2024). Effects of movement speeds and hull forms on wave drag reduction in a single-file formation. *The 15th International Conference of Hydrodynamics*. Roma, Italy. (Based on Chapter 4 of this thesis)

Acknowledgements

I am deeply grateful to my supervisor, Dr. Zhiming Yuan, for his invaluable guidance, continuous support, and patience throughout my study. His profound expertise, sharp thinking, and positive attitude have been instrumental in shaping this work, fostering my personal and academic growth, and helping me reach this important milestone.

I would also like to extend my sincere thanks to the China Scholarship Council (CSC201906950057) for covering my living expenses, and to the Faculty of Engineering and the Department of Naval Architecture, Ocean, and Marine Engineering for their generous scholarship support.

My sincere gratitude goes to Dr. David Dai and Dr. Laibing Jia for their significant contributions to my research. Dr. Dai provided essential guidance during my experiments. Dr. Jia proposed insightful suggestions that greatly enhanced the depth and quality of this work.

My heartfelt thanks go to my colleagues—Ming Zhang, Guangwei Zhao, Yihan Liu, Kwang Sic Chung, Deqing Zhang, Shuanrui Yu, Haitao Wu, Boyu Liao, Wanru Deng, and Maokai Sun—whose academic and personal support greatly enriched this journey of exploration, discovery, and growth.

I am profoundly grateful to my girlfriend, Na Li, for her tolerance, encouragement and trust, which make me feel confident and keep smiling in life. I offer my deepest thanks to my parents for their selfless dedication, which allows me to move forward with unwavering determination.

Chapter 1

Introduction

1.1 Background and motivation

As global demand for resources continues to grow, the exploitation and utilization of marine resources have become increasingly essential, especially as land-based resources become more limited. This shift has led to a surge in maritime activities, requiring innovative approaches to enhance the efficiency and sustainability of ship operations. One promising approach is the strategic formation of ships, which can significantly reduce hydrodynamic resistance, thereby decreasing fuel consumption and environmental impact.

The phenomenon of ducklings following their mother in a single-file formation was explained by Yuan et al. (2021) through the mechanisms of wave-riding and wave-passing. In this arrangement, the first duckling effectively rides on the waves generated by its mother, which are then transferred to the subsequent ducklings. By positioning themselves optimally, the following ducklings can move forward with minimal effort, as they benefit from the wave energy initially created by the mother duck. The wave energy, initiated by the mother duck, passes through the entire formation, from the first to the last duckling, finally dispersing in the form of a Kelvin wave pattern.

Drawing inspiration from this natural phenomenon, recent studies, such as those by Yuan (2022) and Ellingsen (2022), have highlighted the potential for waterborne traffic to similarly harness these hydrodynamic benefits. By advancing in a single-file formation, ships can significantly reduce resistance, leading to improved fuel efficiency and lower operational costs. This concept, rooted in biomimicry, offers a promising solution for optimizing maritime operations in an era where sustainability and resource efficiency are paramount.

In a related but distinct application, the U.S. Defense Advanced Research Projects Agency proposed the "Sea Train" concept in 2020 (DARPA, 2020). This concept envisions multiple ships moving together in waves, either mechanically connected or not, with the goal of reducing fuel consumption and enhancing mobility for military operations. However, the operational scenarios differ: the single-file formation for ducklings or ships typically occurs in calm water, while the Sea Train concept is designed for more challenging conditions, such as sea waves.

Initially proposed to enhance military capabilities, the Sea Train concept also holds significant potential for commercial shipping. In this system, ships are physically connected to form a marine train, where the leading ship, or "engine", provides the necessary propulsion for the entire formation. The following ships, acting as "carriages", do not require their own power. Upon arrival at a port, individual carriages can be unloaded or loaded independently, without delaying the rest of the formation, thereby greatly improving transport efficiency. For large ships carrying diverse cargo for multiple ports, unloading at one port often leaves the vessel in a half-load or partial-load state, resulting in inefficient fuel consumption as it continues to the next destination. In contrast, a sea train system avoids this issue by offloading individual barges while maintaining a full load, thereby reducing fuel consumption and improving efficiency.

In light of these insights, this research is motivated by the need to explore the potential of ship formation strategies to enhance resistance reduction efficiency in calm water. Additionally, when marine trains move in waves, the motion responses become complex, arising not only from hydrodynamic interactions between vessels but also from the dynamic coupling between interconnected components. Accurate prediction of these hydrodynamic responses is crucial to ensuring the safety and efficiency of marine operations, as interactions between ships can amplify the motion responses of the marine train system and potentially damage the mechanical connections.

1.2 Aim and objectives

This thesis aims to investigate the hydrodynamic interactions of ships in a single-file formation, both without and with mechanical connections, in calm water and sea waves. An in-house code, MHydro, is adopted to analyze wave-making and seakeeping problems based on potential flow theory. Additionally, a specific module for interconnected ships is developed using the constraint matrix method. However, as MHydro does not account for water viscosity, complementary experimental studies are necessary. To achieve this aim, the following objectives are established:

- The wave drag reduction of individual ships in various configurations is quantified, and several wave patterns by ships in a single-file formation are identified using the in-house code MHydro.
- The contributions of wave and viscous interference to the total drag reduction of individual ships in various configurations are quantified through resistance experiments in leader-follower formations. The drag reduction mechanism of such formations is analyzed using MHydro, the ITTC (1957) correlation line, and experimental data.
- The hydrodynamic performance of a marine train with two ships advancing in waves is evaluated, considering both non-physical connections and different connection styles. In addition, the effects of advancing speed, joint positions, and inter-ship gaps on the motion responses of a marine train configuration comprising five ships are investigated.

1.3 Novelty and contribution to the knowledge

The novelty of this research can be summarized as follows:

- Ducklings swimming in a single-file formation reduce wave drag and can even generate propulsion, conserving energy through wave-riding and wave-passing mechanisms. Inspired by this, the thesis extends the duckling model to ships in similar formations, exploring wave drag reduction across various configurations through the in-house code MHydro.

- A series of experiments are conducted to measure the resistance of individual ships with varying hull forms, both moving independently and within formations with different configurations, to quantify the contributions of wave and viscous interference to total drag reduction.

- The hydrodynamic interactions among ships moving in waves are predicted using the in-house code MHydro, with a constraint matrix method employed to model various mechanical connection configurations between the ships.

The contributions to knowledge from this research are as follows:

- The mechanisms of wave-riding and wave-passing are applied for the first time to ships moving in a single-file formation, with three new wave patterns related to wave-passing identified.

- This is the first study to quantify the contributions of wave and viscous interference to the total drag reduction of ships moving in a single-file formation. Three critical zones of complex interference are identified when the trailing ship moves within the wake of the leading ship.

- The utilization of the flow wake behind a ship has not been explored previously. This thesis is the first to discover that flow separation behind the transom stern can be transformed into a beneficial factor for drag reduction in ship formations, where the generation of turbulent flow and air bubbles can be exploited to reduce ship resistance.

- This is the first study to consider the effects of advancing speed and various mechanical connections on the motion response of marine trains.

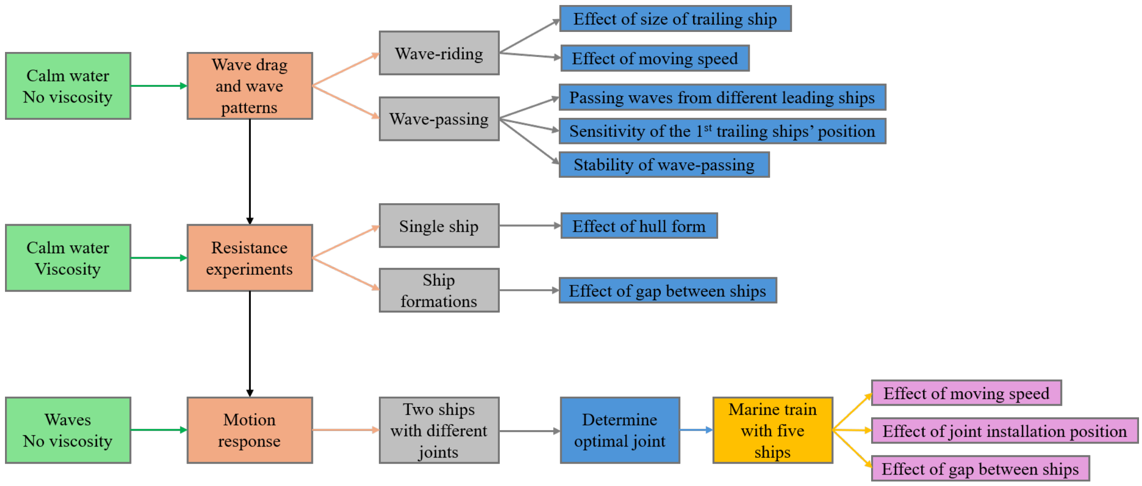

Figure 1.1: Outline of the research contents.

1.4 Outline of the thesis

Chapter 1 presents the background and motivation for the research, outlines the aims and objectives, highlights the novelty and contribution to the field, and provides an overview of the thesis structure.

Chapter 2 provides a comprehensive literature review, focusing on four key aspects: formations in nature, human and navel architecture; prediction and minimisation of ship resistance; flow wake behind transom stern and air lubrication; and hydrodynamic interactions between multiple bodies in waves.

Chapter 3 introduces the core framework of the in-house code MHydro, consisting of two main parts: the first part covers the general formulations of potential theory and associated boundary conditions, while the second part focuses on the Rankine source panel method, the difference scheme, and radiation conditions.

Chapter 4 investigates wave drag and wave patterns generated by ships in a single-file formation, examining the phenomena of wave-riding and wave-passing across different ship formations.

Chapter 5 decouples the total resistance of ships in formations using the form factor method and quantifies the contributions of viscous and wave interference to total drag reduction through a series of experimental tests.

Chapter 6 investigates the hydrodynamic responses of marine trains in waves, comparing the motion responses of ships with different connections. This thesis also examines the effects of varying speeds, joint positions, and gaps between ships on their motion responses.

Chapter 7 summarizes the main conclusions of this PhD research and provides recommendations for future studies.

Chapter 2

Literature Review

In this chapter, a comprehensive review is presented on distinct formations found in nature, human beings, and naval architecture. The state-of-the-art approaches for predicting and minimizing ship resistance are then revisited, with a critical examination of the flow wake behind transom sterns and air lubrication techniques. Finally, the hydrodynamic responses of multi-body systems and marine trains with various configurations in waves are reviewed.

2.1 Formations in nature, humans and naval architecture

Animals in nature often migrate in distinctive formations, which can reduce energy expenditure and enhance their locomotion performance. Schooling fish increases their migratory endurance by adjusting their swimming posture and effectively harnessing the energy from environmental vortices generated by neighboring individuals (Weihs, 1973; Liao et al., 2003; Weihs, 2004; Li et al., 2020). Birds fly in a 'V' formation to minimize individual effort by utilizing the upwash of the vortex region behind their fellow companion's wingtips (May, 1979; Hummel, 1983; Hainsworth, 1987; Cutts and Speakman, 1994; Andersson and Wallander, 2004; Maeng et al., 2013; Portugal et al., 2014). Ducklings swimming in a single-file formation can significantly reduce their metabolic exertion by efficiently transferring momentum from the mother duckling to the smaller ones through the generation and utilization of vorticity (Fish, 1994, 1995).

However, a new insight was provided by Yuan et al. (2021) to shed light on this bio-imprinting behavior, attributing it to wave-riding and wave-passing. Their numerical results revealed that small ducklings could achieve up to 100% wave drag reduction by adjusting their positions to optimal locations.

Inspired by the collective locomotion behaviors of animals, athletes frequently employ the "drafting" strategies in endurance competitions. This tactic not only enables athletes to achieve a specific pace but also helps them conserve energy by moving in a sheltered position behind pace-setters. The impact of drafting in cross-country skiing was assessed by monitoring heart rate responses. The results showed that heart rates were significantly reduced when skiing behind a leader (Bilodeau et al., 1995). The benefits of drafting were also observed in inline skating, with energy expenditure reduced in all drafting conditions, particularly at high velocities and when cornering (Millet et al., 2003). Blocken et al. (2013) used Computational Fluid Dynamics (CFD) to simulate two drafting cyclists in upright, dropped, and time-trial positions with varying separation distances. They found that the trailing cyclist can achieve substantial aerodynamic drag reduction, and the leading cyclist can also reduce aerodynamic drag when the separation distance is short. Blocken et al. (2018) investigated the aerodynamic drag reduction of a cycling peloton with 121 cyclists using high-resolution CFD simulations, with the aid of wind tunnel testing. They found that for a cyclist positioned in the mid-rear of a tightly packed peloton, with multiple rows of riders providing shelter from the wind, aerodynamic drag is reduced to just 5% - 10% of that experienced by an isolated rider. Polidori et al. (2020) analyzed the drafting positions employed by Kenenisa Bekele during the 2019 Berlin Marathon. Their findings revealed that Bekele's drafting strategy led to a reduction in drag resistance and aerodynamic power by 38.5% - 57.3%.

Array configurations are commonly used in wind farms, wave power plants, and autonomous underwater vehicle (AUV) formations to improve power output or reduce energy expenditure. The turbulent wakes generated by upwind turbines can significantly reduce the momentum and energy extraction of downstream wind turbines. Su et al. (2021) proposed triangular and truss configurations for vertical axis wind turbines, which can enhance the power performance of downstream turbines. Cossu (2021) examined three spanwise-periodic rows of wind turbines and determined that tilting the rotors of the turbines in the upwind rows can enhance the total power extracted from the wind by replacing wakes with high-speed streaks. Constructive wave interference between wave energy converters (WECs) can significantly enhance power production. De Andrés et al. (2014) investigated various array layouts, such as linear, triangular, rhombus, and square configurations. The study determined that triangular arrays are ideal for multidirectional wave regimes, whereas square arrays are best suited for unidirectional climates. Chen et al. (2016) studied wave interference between WECs and discovered that positioning the fixed platform at the center of a triangular array notably amplifies constructive effects. Rattanasiri et al. (2014) investigated a fleet of towed AUVs and identified seven zones of dominant spacing between two AUVs based on drag characteristics: parallel, echelon, no gain, push, drafting, low interaction, and no interaction. The energy consumption of a fleet of AUVs can be minimized by arranging them in optimal arrays with the ideal spacing. Zhang et al. (2019) analysed the hydrodynamic interactions between two AUVs and concluded that the tandem array is more efficient for drag reduction compared to the parallel array.

In recent years, various ship formations have been increasingly explored to enhance fuel efficiency in maritime operations. He et al. (2022) adopted the Shear Stress Transport (SST) $k-\omega$ turbulence model to analyze three distinctive ship formations. They found that tandem formation was the most energy efficient, followed by triangular and parallel formation. Dong et al. (2022) studied the echelon formation of unmanned surface vehicles (USVs), analyzing how different spacing configurations influence their friction and pressure resistances. They categorized the aft wedge region into five zones, distinguishing them by calculating the positive and negative attributes of the energy consumption index. A leader-follower ship fleet was studied by Ma et al. (2023), via a 4-point model and Neumann-Michell potential computation. They derived the destructive wave interference region for the follower under different speeds and found the destructive interference was invalid at low or high Froude numbers. Liu et al. (2023) explored the wave resistance and flow field of two KRISO Container Ships (KCS) moving in a line at various speeds and intervals, utilizing the Reynolds-Averaged Navier-Stokes (RANS) method. They attributed the reduction in wave drag for the trailing ship to the superposition of waves around the following vessel with the transverse waves created behind the leading ship.

It is noted that ships traveling in tandem, in a line, or in a leader-follower formation adopt similar configurations, analogous to ducklings swimming in a single-file formation. The key difference is that existing research on ship formations typically involves a limited number of ships, all modeled with identical dimensions, whereas in nature, many smaller ducklings follow their mother. However, variations in the size and number of ships within formations can affect the hydrodynamic interference among them. Additionally, these studies only focus on the effects of speed and spacing between ships on drag reduction, while neglecting the application of wave-riding and wave-passing mechanisms.

2.2 Prediction and minimization of ship resistance

To date, numerous researchers have devoted extensive efforts to the numerical calculations and experimental measurements of the ship resistance. Froude and Froude (1888) conducted measurements and analyses of ship resistance, proposing that the total resistance of a ship comprises frictional resistance and residual resistance. Based on the thin-ship approximation, Michell (1898) derived the wave resistance of a ship moving at a steady speed on calm water. Since the beginning of the 20th century, many researchers have done a lot of analytical calculations based on thin ship theory. Wigley (1926), Havelock (1932) and Weinblum (1959) presented sample computations of Michell's integral and compared it with experiments. Michell's theory forecasts peaks and troughs in the curve depicting wave-resistance coefficients when plotted against the Froude number; however, the curve of residuary-resistance coefficients for a ship model exhibits markedly less oscillation. The flow around a real ship was described by Guilloton (1964) within the framework of linearized wave, while Wehausen (1967) derived the higher-order boundary conditions. Hsiung (1981) expressed the wave resistance of catamarans in quadratic form by introducing a set of “tent” functions. Noblesse et al. (2008) proposed Michell-Kelvin linearized free-surface boundary condition to calculate the wave resistance experienced by ships.

Although the thin ship theory can predict the wave resistance with satisfactory accuracy (Tuck, 1989), it is not very popular in practical engineering due to its limitations of geometric assumptions. The strip ship theory overcomes this limitation by longitudinally segmenting the ship into strips. Originally proposed by Kriloff (1896), it was not widely recognized until Weinblum and Denis (1950) brought it to prominence in 1950. Owing to the efforts of Jacobs et al. (1960), the application of the strip theory became feasible in 1960. Since then, numerous variants of the strip ship theory have been advanced by researchers (Ogilvie and Tuck, 1969; Faltinsen, 1971; Beck, 1989; Bertram, 2011; Newman, 2018). Among these, the slender ship theory has gained popularity for its ability to account for the effects of forward speed and longitudinal interference (Newman, 1964). It is the work of Hess and Smith (1964) that lays the foundation for the calculation of arbitrary three-dimensional bodies. Incorporating the Boundary Element Method (BEM), a variety of 3D panel methods have been formulated and employed (Korsmeyer et al., 1993; Pinkster, 2004; Xiang and Faltinsen, 2011a; Zhou et al., 2012; Yuan et al., 2015).

With the advancement of high-performance computing, CFD technology has been increasingly utilized to analyze the components of ship resistance, taking the viscous effects into account (Sadat-Hosseini et al., 2013; Zha et al., 2014; Riesner and el Moctar, 2018; Terziev et al., 2019). Experimental tests often provides highly accurate and reliable data, serving as a benchmark for comparing different theories, models, or simulations. Many experiments for the measurements of wave resistance have been carried out in world-leading tanks: DTMB (Olivieri et al., 2006),force Technology (Joncquez et al., 2008), HSVA (Moctar et al., 2017), RIAM (Kashiwagi et al., 2019). In the experimental tests, the longitudinal-cut method (LCM) was extensively investigated to measure the wave resistance by analyzing the wave profile parallel to the model's velocity (Newman, 1963; Eggers, 1967; Moran and Landweber, 1972; Tsai and Landweber, 1975; Lalli et al., 1998, 2000).

Several correlation lines (Schoenherr, 1932; CWB, 1999; Katsui, 2005) have been formulated to predict the frictional resistance of a smooth plate. The correlation line proposed by ITTC (1957) is commonly adopted in calculating the frictional resistance of a vessel. For a ship with a three-dimensional shape, the form resistance is associated with frictional resistance, viscous pressure resistance, and flow separation (Faltinsen, 2005). The form factor method was first proposed by Hughes (1954), in which the total resistance is the sum of form resistance, frictional resistance, and wave resistance. This method was later improved by ITTC (1978), considering the contributions of roughness allowance and air resistance.

To minimize the total wave drag, multi-hull vessels are designed to harness the cancellation effects between waves generated by the hulls. Wilson et al. (1992) conducted both analytical predictions and towing basin validation experiments for the wave cancellation multihull of a trimaran at the David Taylor Model Basin. Suzuki and Ikehata (1995) determined the optimal positions of trimaran outriggers by mathematically representing the hull form with cosine waterlines and parabolic frame lines. Based on the thin ship theory, Tuck and Lazauskas (1998) studied a family of multihull ships by varying the number of hulls, their placement, and beams, while maintaining the total displacement of the vessel as well as the individual length and shape of each hull constant. The optimum configurations for two, three, and four-hulled vessels were determined, considering both configurations with and without longitudinal stagger, across a broad spectrum of speeds. Similarly, Peng (2001) investigated the effect of wave interference on the wave resistance of a family of multihull ships within the framework of thin ship theory. The study focused on the steady motion of ships on an unbounded free surface of deep water and the wave resistance and wave patterns are computed and analyzed by varying relative positions of the hulls. Yu et al. (2017) explored the prospective optimal di-hull configurations, which involve two ships moving in parallel at specific longitudinal and lateral distances from each other, using towing-tank tests and longitudinal wave-cut analysis. The resistance reduction predicted by the thin ship theory was evaluated by comparing it with experimental results, and the usefulness and limits of the theory are examined. The wave interference effects between the outriggers and center-hull on the resistance of a trimaran are researched by Yildiz et al. (2020), based on the turbulence model of unsteady Reynolds-averaged Navier-Stokes (URANS).

It is essential to consider the intervals between hulls and their speed of movement, as these aspects significantly influence wave interference effects (Soding, 1997; Yeung and Wan, 2008). Numerical and experimental studies have revealed that, typically, wave interference between the hulls of a catamaran results in a marked increase in total resistance, especially within the range of Froude numbers from 0.45 to 0.65, in comparison to a monohull (Zaghi et al., 2011; Broglia et al., 2014; He et al., 2015). However, by arranging two hulls in an asymmetric di-hull system and setting the stagger at half the ship's length to induce destructive interference, the overall resistance can be significantly reduced, especially when travelling at speeds close to a Froude number of 0.4 (Faltinsen, 2005; Soding, 1997; Yeung et al., 2004). In trimaran design, the longitudinal and transverse distance between the main hull and the outriggers are paramount for minimising resistance. Mynard and his colleagues investigated the wave resistance and patterns of Model 9 in the AMECRC series (Mynard et al., 2008). Utilising the CFD suite SHIPFLOW, slender body theory, and a series of experiments, they identified the optimal longitudinal positions for the outriggers at various operational speeds. By integrating the analytical expression of the characteristics of linear wave resistance with the steepest descent method, Wang et al. (2021) introduced an efficient method for optimizing the layout of trimaran outriggers. The results demonstrate a high level of accuracy in finding the optimal solution and a significant improvement in computing efficiency when compared to conventional enumeration methods. Nazemian and Ghadimi (2021) studied the trimaran hull optimization by using a multi-objective optimization platform. The Arbitrary Shape Deformation technique and Simcenter SHERPA algorithm were applied for geometry optimization.

The optimal spacing between hulls at specific speeds is typically determined based on wave drag reduction or total drag reduction. However, few studies have accounted for the role of viscous drag reduction in determining the optimal positioning between hulls. This consideration is equally relevant for ships traveling in a single-file formation. To design optimal ship formations, it is essential to quantify the individual contributions of wave interference and viscous interference to total drag reduction. Furthermore, as speed and spacing vary, the viscous and wave interactions between ships also change. Therefore, it is crucial to reveal these mechanisms to effectively reduce total drag.

2.3 Flow wake behind transom stern and air lubrication

Streamlined ships are designed to reduce resistance, while transom stern designs are widely used for commercial vessels, especially container ships, due to their ease of construction. However, the wake behind the transom stern is complex, which poses challenges for the prediction of ship resistance. Earlier studies primarily focused on the macroscopic characteristics of the wake. Flow separation at the transom stern can generate partial or complete ventilation, resulting in a hollow cavity on the free surface. A wet or dry transom stern lead to hydrostatic resistance due to the absence of hydrostatic pressure on the transom face. To estimate this hydrostatic resistance, Doctors and his colleges (Doctors and Beck, 2005; Maki et al., 2006; Doctors, 2006; Doctors and of New South Wales, 2007; Maki et al., 2007) proposed two sets of regression formulas based on experimental tests to predict the drop in the water level and the length of the hollow cavity behind the transom. A typical technique for handling transom flow in numerical simulations was to impose the Kutta condition at the trailing edge, ensuring a smooth detachment of the wave flow from the stern (Tulin and Hsu, 1986; Nakos and Sclavounos, 1994; Mola et al., 2017).

With improvements in computational methods and experimental techniques, significant effort has been devoted to studying the microscopic characteristics of the wake behind the transom stern. The closure of the hollow or the reattachment of the flow is usually accompanied by wave breaking, air entrainment and spray generation, leading to significant energy dissipation and increased resistance. The overturning and breaking of the free surface cause air entrainment, which further generates bubble plumes or bubble clouds. Hendrickson et al. (2019) analyzed the flow structures in the air-water mixed region and the characteristics of air entrainment behind rectangular dry transom sterns using the Lagrangian cavity identification technique and high-resolution implicit large eddy simulation (iLES) . They also characterized the incompressible highly variable density turbulence (IHVDT) in the mixed-phase region by developing an explicit algebraic closure model for the turbulent mass flux (TMF) (Hendrickson and Yue, 2019). Terrill and Taylor (2015) measured the void fraction field by deploying a conductivity probe vertical array at the blunt transom of a full-scale surface ship. Using optical laser beam scattering characteristics, Abbaszadeh et al. (2020) presented the average bubble size and bubble number density distribution in the wake of a transom stern model.

The bubbles generated in the wake of leading ship through air entrainment provide a potential application for air lubrication to reduce frictional resistance of the trailing ship. Based on the working principles, the air lubrication technique can be classified into three types of drag reduction: bubble drag reduction (BDR), air layer drag reduction (ALDR), and air cavity drag reduction (ACDR) (Ceccio, 2010). The BDR method can be achieved by injecting microbubbles into the turbulent boundary layer (TBL), which influences the turbulent transport of momentum (Zhang et al., 2020). Laser Doppler velocimeter measurements by Kato et al. (1999) in a turbulent boundary layer with microbubbles demonstrated a decrease in near-wall velocity and velocity gradient, resulting in reduced shearing stress. Hassan et al. (2005) and Ortiz-Villafuerte and Hassan (2006) employed particle tracking velocimetry to measure the velocity fields of horizontal channel flow, finding that microbubble injection into a turbulent boundary layer can achieve up to 40% drag reduction by dynamically interacting with the turbulence structure and altering the vorticity and viscous sublayer thickness. A hydrofoil bubble generator, developed by Kumagai et al. (2015) and Murai et al. (2020), achieved a net power saving of 5–15% when introduced to the ship hull in a series of full-scale tests.

When sufficient bubbles are injected beneath the flat bottom of a ship, they may coalesce to form an air layer. A complete replacement of the liquid phase with the air phase within the boundary layer substantially reduces total drag. Friction drag reduction exceeding 80% can be achieved when bubbles form a thin, stable, continuous gas film beneath the surface of a long flat plate at the lowest inflow speed and highest air injection rate (Sanders et al., 2006; Elbing et al., 2008). However, ALDR is sensitive to inflow conditions; at high flow speeds, the air layer becomes unstable and fragile. The ACDR method can mitigate this disadvantage by modifying the hull design, particularly through the use of stepped hulls on planing crafts. Lay et al. (2010) examined the ventilated cavity flow formed downstream of a backward-facing step and found that stable cavities were produced, reducing skin drag by more than 95%.

Flow separation behind a transom stern generates a turbulent wake, increasing drag for the individual ship. Air lubrication techniques, which often involve hull modifications or additional pumps to generate air bubbles, can reduce drag but may compromise structural integrity or raise energy consumption. In a single-file formation, trailing ships can potentially exploit the disturbed wake of the leading ship, including air cavities or bubbles, to reduce drag. This approach offers a promising alternative to traditional air lubrication methods, providing a more energy-efficient solution.

2.4 Hydrodynamic responses of multi-body systems in waves

Multi-body systems are essential in designing and analyzing offshore structures, ensuring the functionality and safety of marine operations. To analyze the multi-body systems, two primary approaches are commonly employed. The first approach involves initially solving the hydrodynamic interactions among multiple bodies while assuming no constraints exist between them. Once wave loads and hydrodynamic coefficients are determined, the constraints introduced by various mechanical connections are incorporated into the equations of motion (Langley, 1984; Ó'Catháin et al., 2008; Sun et al., 2011). Koo and Kim (2005) analyzed the coupling effects of two floating platforms connected by elastic lines in the time domain. Using a 12×12 hydrodynamic coefficient matrix, they developed an exact method that accounted for vessel and line dynamics, revealing significant differences in sway and roll modes compared to conventional approximation methods. Sun et al. (2012) explored diffraction-induced interaction effects between a large-volume substructure and an installation barge during float-over operations through a two-stage approach. Feng and Bai (2017) introduced a constraint matrix method to simulate interactions between two floating barges. Their findings underscored the significant contribution of second-order responses to the nonlinearity of middle-hinge connections by decomposing higher harmonic components. Huang et al. (2018) investigated the response of a passive telescopic gangway between a monohull flotel and an FPSO in a nonparallel side-by-side configuration. They modeled the gangway's rotation and extension using rigid-body dynamics. The second approach directly addresses discontinuous deflections of multi-body systems with mechanical joints by employing the mode expansion technique, offering greater efficiency (Newman, 1994; Lee and Newman, 2000; Taghipour and Moan, 2008). The motion responses of floating interconnected structures can be characterized by "wet" modes in waves, including six rigid-body motions (surge, sway, heave, roll, pitch, yaw), and "dry" modes in air, shaped by mechanical connections. Hong et al. (2005) analyzed the motion and drift forces of side-by-side moored LNG FPSO and LNGC using a higher-order boundary element method (HOBEM) combined with a generalized mode approach. Their findings, validated by experimental data, demonstrated the feasibility of this numerical method in predicting complex multi-body interactions.

The hydrodynamic interactions between these floating structures and the mechanical influences of their connectors result in significantly different response characteristics. Gao et al. (2011) investigated the effect of the placement and rotational stiffness of flexible line connections on the hydroelastic response of very large floating structures (VLFS). Their findings indicated that hinge-line connectors, when optimally positioned, are more effective than rigid connectors in minimizing both hydroelastic responses and stress resultants. Ren et al. (2019) explored the impact of various outermost connector designs on the hydrodynamic performance of modular multi-purpose floating structures (MMFS). Their results showed that the hydrodynamic responses of the MMFS system are influenced by connector type, wave phase, and wavelength. Additionally, the hinge-type connector design is found to play a key role in reducing bending moments and shear forces on connectors under extreme marine conditions. Bispo et al. (2022) developed a numerical model to study wave interactions with a moored articulated VLFS, finding that the rotational stiffness of the hinges significantly influenced both the vertical displacement of the structure and the mooring line tensions. Zhang et al. (2023) analyzed the motion behavior of large arrays formed by multiple floaters connected by hinges, observing that while hinge constraints significantly suppressed heave motion, they also induced strong pitch motion across a broader range of wavelengths. Li et al. (2023) conducted a hydroelastic and expansibility analysis of a Modular Floating Structure (MFS) with multi-directional hinge connections. Their findings highlighted that greater stiffness results in a more pronounced structural response, with the system's reactions intensifying as stiffness increases. Additionally, they observed that smaller module sizes cause larger vertical displacements and reduced moments, while the hydroelastic behavior remains largely unaffected by module size in long-wave conditions.

Marine trains are complex multi-body systems, involving not only hydrodynamic interactions among ships but also dynamic coupling between interconnected components. Within the marine train concept, two primary approaches are typically utilized. The first involves directly linking multiple consecutive vessels using physical connectors, ensuring stable and coordinated transit operations. The second approach utilizes compressive forces, facilitated by a specially designed hull form, to keep the vessels aligned and connected without the need for physical connectors. A notable example is the Seasnake concept (Anderson, 2013), where a tractor unit pulls multiple barge modules connected by a ball-and-socket coupling. The Articulated Tug Barge (ATB) system (Brown and Runyon, 2022), however, uses a tugboat to push load-carrying barges, with articulated connectors securing the tug within a notch in the barge. The U.S. Navy's Improved Navy Lighterage System (INLS) (Guha et al., 2013) employs small warping tugs to propel barges connected by a bull-nose and socket arrangement, with a flexor tension member that allows each unit to pitch relative to the others. However, large forces that can develop between units pose challenges for mechanical connections. In response, the U.S. Navy's Transoceanic Connectorless Seatrain Concept (Karafiath et al., 2009) features sharp bows that fit into V-shaped notches in the sterns of adjacent units, relying on compressive forces to maintain connection. Each unit is equipped with water jets at the transom, positioned on either side of the notch, to assist with alignment and control during transit. This system, however, presents challenges in designing bumpers and fenders to manage the forces and prevent damage during transit.

Resistance reduction, turning performance, shear forces at joints, and motion response are key considerations in the design of marine trains. Mizine and Karafiath (2015) designed a high-speed trimaran sea train with a ball-and-opening socket arrangement between units. Their model tests demonstrated that a four-unit sea train reduced resistance per unit by 24% to 30% within the 10 to 30-knot speed range. Additionally, they found that the maximum turning diameter of the assembled sea train was approximately three times the total length of the system. Zhang et al. (2021) tested an articulated pusher-barge system and observed that both the ATB system and the pusher experienced significant increases in sinkage at higher speeds and shallow drafts. To further investigate the vertical forces on the coupling of a pusher tug-barge system in waves, Mumford (1993) developed a numerically fast three-dimensional solution method based on the unified slender body theory. This method considered the interactions between the two hulls in coupled modes of motion at zero speed. Miller et al. (2001) conducted integrated tug-barge (ITB) model tests and found that the maximum longitudinal, transverse, and vertical connection forces occurred at wave encounter angles of 0°, 45°, and 225°, respectively. Qin et al. (2023) employed STAR-CCM+ to investigate a conceptual sea train featuring a small water-plane-area trimaran in heading waves. They analyzed two configurations: one with physical connections allowing relative pitch motion between vessels and another with non-physical connections. Their results indicated that the drag reduction between the two configurations was minimal, while the physically connected system significantly reduced the pitch motion of each vessel.

Although significant work has been done to understand the motion responses of interconnected floating structures, these studies only focused on stationary multi-body systems, without accounting for moving speed. However, moving speed is a critical factor in the design of marine trains, as it influences the encounter wavelength and, consequently, the hydrodynamic interactions between individual vessels. Additionally, existing studies have mainly investigated hinged connections for marine trains moving in waves. These connections, however, may experience high shear forces that could damage the mechanical joints. Therefore, it is essential to consider various connection types and their impact on both motion responses and shear forces to determine the optimal mechanical connection when designing such systems.

2.5 Summary and research gaps

This chapter reviews previous studies on distinctive formations, wave and viscous interference among ships, and hydrodynamic interactions among multiple floating bodies in waves. Inspired by the phenomenon that ducklings swim in a single-file formation, several studies explored ships moving in such formations. However, these studies do not take the potential for utilising wave-riding and wave-passing mechanisms into account. Furthermore, the optimal spacing between hulls in multi-hull ships and ships in formations has typically been determined based on either total drag reduction or wave drag reduction. Nevertheless, viscous interference also plays a crucial role in determining optimal positions, particularly for transom stern configurations operating at high speeds. In such scenarios, flow separation can result in intense turbulent flow, accompanied by air entrainment and the generation of air bubbles, which is generally unfavorable for minimizing ship resistance. Nevertheless, this phenomenon offers a potential solution for resistance reduction through air lubrication for ships operating within this flow. Finally, while previous studies explored the motion response of floating multi-body systems, they focused on stationary states in waves. The effects of moving speed and mechanical connection styles, which are crucial for understanding the motion response of marine trains, remain underexplored. Therefore, the following chapters of this thesis aim to address these gaps.

Chapter 3

Numerical Implementation of 3-D Potential Flow

3.1 Introduction

The methodology chapter outlines the computational framework used to predict the wave-making resistance of ships in calm water, as well as their wave-induced motions and loads in waves. By employing three-dimensional potential flow theory, this thesis focuses on analysing hydrodynamic interactions among multiple ships in a row, while simplifying the problem by neglecting viscous effects. The Rankine source panel method forms the core of the numerical approach, enabling efficient solutions to boundary value problems. Advanced numerical techniques, such as the upwind difference scheme, are implemented to enhance stability, while the improved Sommerfeld radiation condition ensures realistic representation of wave behaviour at the domain boundaries. This chapter begins with a description of the governing equations and boundary conditions that define the hydrodynamic problem. It then elaborates on the numerical methods, detailing the Rankine source panel method and its implementation. Stability improvements and boundary treatments are also discussed, highlighting their role in ensuring computational accuracy and reliability. These techniques form the core of the in-house code MHydro.

3.2 General formulations of potential flow theory

3.2.1 Reference systems

When ships move in calm water or waves, two sets of right-handed coordinate systems are adopted. The first is a global reference system, denoted as o-xyz, which is fixed to the earth. The second is a local reference system, denoted as O_n-$X_nY_nZ_n$ ($n = 0, 1, 2, \ldots, N$), which is fixed to each ship, as shown in Figure 3.1. "n" represents the number of each individual, while "N" represents the last trailing ship. The plane Z=0 represents an undisturbed free surface with a positive Z-axis upwards and a positive Y-axis to the starboard. The leading ship and trailing ships are assumed to move with the same speed U and the same direction along the negative X-axis. The direction of the incident wave is defined by the angle β between the direction of wave propagation and the direction of the ship's movement. β=90, 135 and 180 degrees correspond to beam, oblique and head seas, respectively. The six degrees of freedom in vessel motion include the translational motions of surge (parallel to the X-axis), sway (parallel to the Y-axis), and heave (parallel to the Z-axis), as well as the rotational motions of roll (around the X-axis), pitch (around the Y-axis), and yaw (around the Z-axis).

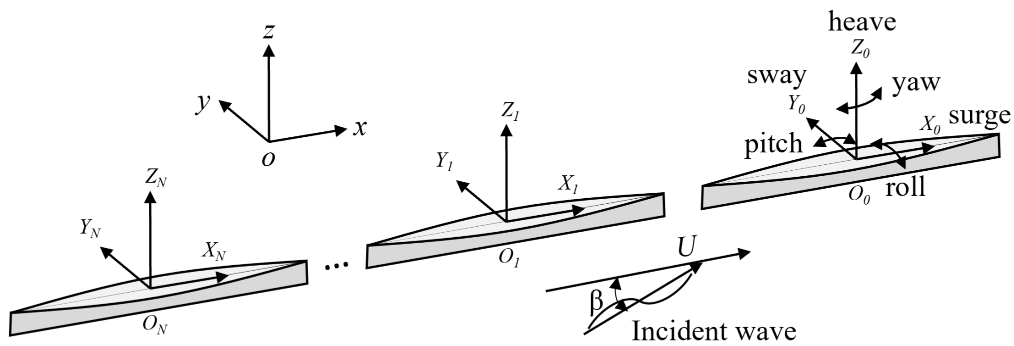

Figure 3.1: Coordinate systems.

3.2.2 Wave-making problems

Assuming the fluid is incompressible, inviscid, and the flow is irrotational, there exists a velocity potential φ that satisfies the three-dimensional Laplace equation,

$$\frac{\partial^2\varphi}{\partial x^2}+\frac{\partial^2\varphi}{\partial y^2}+\frac{\partial^2\varphi}{\partial z^2}=0. \tag{3.1}$$

In the local reference system, the kinetic free-surface condition can be expressed by

$$\frac{\partial\varphi}{\partial t}+g\zeta-U\frac{\partial\varphi}{\partial x}+\frac{1}{2}\left(\frac{\partial^2\varphi}{\partial x^2}+\frac{\partial^2\varphi}{\partial y^2}+\frac{\partial^2\varphi}{\partial z^2}\right)=0. \tag{3.2}$$

where g is the gravitational acceleration. The dynamic boundary condition on the free surface is expressed by

$$\frac{\partial\zeta}{\partial t}-U\frac{\partial\zeta}{\partial x}+\frac{\partial\varphi}{\partial x}\frac{\partial\zeta}{\partial x}+\frac{\partial\varphi}{\partial y}\frac{\partial\zeta}{\partial y}=\frac{\partial\varphi}{\partial z}. \tag{3.3}$$

It is worth noting that the leading ship and trailing ships are assumed to move with the same speed U and the same direction, so the vessel encountering or overtaking will not take place. The shallow water effect is not considered in the present numerical calculations and the velocity potential is time-independent in the body-fixed frame. Since the ship moving speed is constant, the hydrodynamic interaction can be handled by a steady state problem. By combining kinetic and dynamic free-surface conditions, it satisfies the time-independent linearized steady Neumann-Kelvin free surface condition (Newman, 2018):

$$U^2\frac{\partial^2\varphi_s}{\partial x^2}+g\frac{\partial\varphi_s}{\partial z}=0, \quad \text{on } z=0. \tag{3.4}$$

where φ_s represents steady velocity potential. The boundary condition of the ship surface should meet that there is no flow through the body surface,

$$\frac{\partial\varphi_s}{\partial n}=U\mathbf{n}, \quad \text{on the ship surface.} \tag{3.5}$$

where $\mathbf{n}=(n_1,n_2,n_3)$ is the unit vector inward on the wetted body surface. In addition, a radiation condition is applied to the control surface to ensure that the wave disappears at infinity:

$$\varphi_s \to 0, \zeta \to 0, \text{ as } \sqrt{x^2 + y^2} \to \infty, \tag{3.6}$$

where ζ is the wave elevation. The boundary condition on the seafloor can be expressed by

$$\frac{\partial \varphi_s}{\partial n} = 0, \quad \text{on the seafloor.} \tag{3.7}$$

As this thesis focuses on the fundamental analysis of complex wave interference phenomena, the linearized Bernoulli's equation is employed to simplify the approach. Once the unknown potential φ_s is solved, the steady pressure over the wetted hull surface can be calculated by

$$p_s = \rho U \frac{\partial \varphi_s}{\partial x}, \tag{3.8}$$

where ρ is the water density. Integrating the pressure on the wetted hull surface, the force (or moment) can be obtained by

$$F_j = \iint p_s \mathbf{n}_j \, ds \quad j = 1, 2, \ldots, 6, \tag{3.9}$$

where $j = 1, 2, \ldots, 6$ represent surge, sway, heave, roll, pitch and yaw, respectively.

The wave-making resistance is equal to the component of the force in the surge direction Yuan et al. (2019). From the boundary conditions of the dynamic free surface, the wave elevation can be derived in the form,

$$\zeta = \frac{U}{g} \frac{\partial \varphi_s}{\partial x}. \tag{3.10}$$

3.2.3 Seakeeping problems

For a fleet of ships with forward speed in waves, the wave-induced motions and loads are computed using linear diffraction and radiation theory. The velocity potential in the flow field can be decomposed into

$$\Phi_T(x, y, z, t) = -Ux + \varphi_s(x, y, z) + \Phi(x, y, z, t) \tag{3.11}$$

On the right-hand side, the sum of the first and second terms represents the steady flow potential, while the third term denotes the wave velocity potential.

$$\Phi(x, y, z, t) = \Phi_0 + \Phi_7 + \Phi_j = \Re\left\{[\varphi_0(x, y, z) + \varphi_7(x, y, z) + \varphi_j(x, y, z)]e^{-i\omega_e t}\right\} \tag{3.12}$$

where Φ_0, Φ_7, and Φ_j (with $j = 1, 2, \ldots, 6$) represent the spatial velocity potentials of the incident wave, diffracted wave, and radiated wave, respectively. ω_e is the encounter wave frequency. The time-independent velocity potentials are φ_0, φ_j and φ_7, respectively. The corresponding boundary conditions are discussed in the following sections.

Incident wave

According to Faltinsen (1993), the incident velocity potential is expressed by

$$\varphi_0 = -\frac{ig\eta_0}{\omega_0}\frac{\cosh k(z+h)}{\cosh kh}e^{i[k(x\cos\beta + y\sin\beta)]} \tag{3.13}$$

where ω_0 is the incident wave frequency and η_0 is the incident wave amplitude. The encounter wave frequency can be obtained by

$$\omega_e = \omega_0 - Uk\cos\beta \tag{3.14}$$

If the water depth h is given, the wave number k can be determined using the dispersion relation

$$\frac{\omega_0^2}{g} = k \cdot \tanh(kh) \tag{3.15}$$

The real and imaginary parts of incident wave potential are expressed by

$$Re[\varphi_0(x,y,z)] = \frac{g\eta_0}{\omega_0} \cdot \frac{\cosh(k(z+h))}{\cosh(kh)} \cdot \sin(k(x\cos\beta + y\sin\beta)) \tag{3.16}$$

$$Im[\varphi_0(x,y,z)] = -\frac{g\eta_0}{\omega_0} \cdot \frac{\cosh(k(z+h))}{\cosh(kh)} \cdot \cos(k(x\cos\beta + y\sin\beta)) \tag{3.17}$$

where Re represents the real part, and Im represents the imaginary part. The normal induced velocity of the incident wave can be derived from the partial derivatives of both the real and imaginary components of the incident wave potential (Li, 2001).

$$\frac{\partial Re[\varphi_0(x,y,z)]}{\partial x} = \eta_0\omega_0\cos\beta \cdot \frac{\cosh(k(z+h))}{\sinh(kh)} \cdot \cos\left[k(x\cos\beta + y\sin\beta)\right] \tag{3.18}$$

$$\frac{\partial Re[\varphi_0(x,y,z)]}{\partial y} = \eta_0\omega_0\sin\beta \cdot \frac{\cosh(k(z+h))}{\sinh(kh)} \cdot \cos\left[k(x\cos\beta + y\sin\beta)\right] \tag{3.19}$$

$$\frac{\partial Re[\varphi_0(x,y,z)]}{\partial z} = \eta_0\omega_0 \cdot \frac{\sinh(k(z+h))}{\sinh(kh)} \cdot \sin\left[k(x\cos\beta + y\sin\beta)\right] \tag{3.20}$$

$$\frac{\partial Im[\varphi_0(x,y,z)]}{\partial x} = \eta_0\omega_0\cos\beta \cdot \frac{\cosh(k(z+h))}{\sinh(kh)} \cdot \sin\left[k(x\cos\beta + y\sin\beta)\right] \tag{3.21}$$

$$\frac{\partial Im[\varphi_0(x,y,z)]}{\partial y} = \eta_0\omega_0\sin\beta \cdot \frac{\cosh(k(z+h))}{\sinh(kh)} \cdot \sin\left[k(x\cos\beta + y\sin\beta)\right] \tag{3.22}$$

$$\frac{\partial Im[\varphi_0(x,y,z)]}{\partial z} = -\eta_0\omega_0 \cdot \frac{\sinh(k(z+h))}{\sinh(kh)} \cdot \cos\left[k(x\cos\beta + y\sin\beta)\right] \tag{3.23}$$

Diffraction wave

When ships are stationary in waves, the incident waves will be influenced by the ships, generating diffracted waves. The diffraction waves are evaluated by fixing ships ($n = 0, 1, 2, \ldots, N$) in incident waves. Based on the study of Inoue and Kamruzzaman (2008), the diffraction wave potential can be determined by solving the following boundary value problems:

$$\nabla^2\varphi_7 = 0 \tag{3.24}$$

$$g\frac{\partial\varphi_7}{\partial z} - \omega_e^2\varphi_7 + 2i\omega_e U\frac{\partial\varphi_7}{\partial x} + U^2\frac{\partial^2\varphi_7}{\partial x^2} = 0, \quad (z=0) \tag{3.25}$$

$$\left.\frac{\partial \varphi_7}{\partial \mathbf{n}}\right|_{S_n} = -\left.\frac{\partial \varphi_0}{\partial \mathbf{n}}\right|_{S_n}, \quad (n = 0, 1, 2, ..., N) \tag{3.26}$$

$$\left.\frac{\partial \varphi_7}{\partial \mathbf{n}}\right|_{z \to -h} = 0 \tag{3.27}$$

Additionally, a radiation condition must be applied to the boundary value problem, which will be discussed in Section 3.3.3.

Radiation wave

Radiation waves are generated by the forced oscillation of each ship, and the radiation wave force experienced by one ship can be influenced not only by its own oscillations but also by the oscillations of other ships. Within the framework of linearized theory, the radiation wave potential can be expressed as

$$\varphi_j(x, y, z) = \Re \sum_{n=0}^{N} \sum_{j=1}^{6} [\varphi_j^n(x, y, z)\eta_j^n] \tag{3.28}$$

Here, η_j $(j = 1, 2, \ldots, 6)$ is the corresponding motion amplitude in six degrees of freedom, respectively: η_1, surge; η_2, sway; η_3, heave; η_4, roll; η_5, pitch; η_6, yaw.

The radiated wave potential per unit velocity for the j-th motion mode of ship n can be obtained by satisfying the body surface conditions for ship n when it is in motion, while all other ships remain stationary (Fang and Kim, 1986).

$$\nabla^2 \varphi_j^n = 0 \tag{3.29}$$

$$g\frac{\partial \varphi_j^n}{\partial z} - \omega_e^2 \varphi_j^n + 2i\omega_e U \frac{\partial \varphi_j^n}{\partial x} + U^2 \frac{\partial^2 \varphi_j^n}{\partial x^2} = 0, \quad (z = 0) \tag{3.30}$$

$$\left.\frac{\partial \varphi_j^n}{\partial \mathbf{n}}\right|_{S_n} = -i\omega_e \mathbf{n}_j^n + U m_j^n \tag{3.31}$$

$$\left.\frac{\partial \varphi_j^{n'}}{\partial \mathbf{n}}\right|_{S_{n'}} = 0, \quad \text{on other ships} \tag{3.32}$$

$$\left.\frac{\partial \varphi_j^n}{\partial \mathbf{n}}\right|_{z \to -h} = 0 \tag{3.33}$$

The generalised normal vectors can be given by

$$n_j = \begin{cases} \mathbf{n}, & \text{if } j = 1, 2, 3 \\ \mathbf{x} \times \mathbf{n}, & \text{if } j = 4, 5, 6 \end{cases} \tag{3.34}$$

where $\mathbf{x} = (x, y, z)$ is the position vector on the body surface. The m-term m_j considers the effect of the steady flow on the radiation boundary condition, which can be expressed as:

$$m_j = \begin{cases} -(\mathbf{n} \cdot \nabla)\nabla\varphi_s, & \text{if } j = 1, 2, 3 \\ -(\mathbf{n} \cdot \nabla)(\mathbf{x} \times \nabla\varphi_s), & \text{if } j = 4, 5, 6 \end{cases} \tag{3.35}$$

This thesis adopts the Neumann-Kelvin linearization (Newman, 2018) to simplify the m-term,

$$\begin{aligned} (m_1, m_2, m_3) &= (0, 0, 0) \\ (m_4, m_5, m_6) &= (0, n_3, -n_2) \end{aligned} \tag{3.36}$$

The added mass and damping coefficients of ship n in the j-th mode, induced by the oscillatory motion of ship n' in the j'-th mode, can be expressed as follows:

$$\mu_{jj'}^{nn'} = -\frac{\rho}{\omega_e} \iint_{S_n} \left(Im[\varphi_{j'}^{n'}] - \frac{U}{\omega_e} \frac{\partial Re[\varphi_{j'}^{n'}]}{\partial \mathbf{x}} \right) \mathbf{n}_j \, dS, \tag{3.37}$$

$$\lambda_{jj'}^{nn'} = -\rho \iint_{S_n} \left(Re[\varphi_{j'}^{n'}] + \frac{U}{\omega_e} \frac{\partial Im[\varphi_{j'}^{n'}]}{\partial \mathbf{x}} \right) \mathbf{n}_j \, dS, \tag{3.38}$$

Coupled motion equations

Once the diffraction and radiation velocity potential are solved, the pressure on the body surface can be obtained based on Bernoulli's equation:

$$p = -\rho \left[i\omega_e \eta\varphi + \nabla(\varphi_s - Ux) \cdot \nabla\eta\varphi \right], \tag{3.39}$$

The wave excitation force in six degrees of freedom on ship n can be determined by integrating the pressure distributions of both the incident and diffracted waves over the wetted body surface.

$$F_j^n = \iint_{S_n} (p_0^n + p_7^n)\,\mathbf{n}_j\,dS, \quad j = 1, 2, \ldots, 6, \tag{3.40}$$

According to Newton's second law, the motion components in the frequency domain can be obtained by

$$\left[-\omega_e^2\left(\mathbf{M}^n + \mu_{jj}^{nn}\right) + i\omega_e\lambda_{jj}^{nn} + \mathbf{K}^n\right]\eta_j^n + \sum_{n'=0,n'\neq n}^{N}\left\{\left[-\omega_e^2\mu_{jj'}^{nn'} + i\omega_e\lambda_{jj'}^{nn'}\right]\eta_j^n\right\} = F_j^n \tag{3.41}$$

where $\mathbf{M}$ and $\mathbf{K}$ represent the generalised mass matrix and restoring matrix. The mass matrix and restoring force matrix are calculated by

$$\mathbf{M} = \begin{bmatrix} m & 0 & 0 & 0 & mz_G & 0 \\ 0 & m & 0 & -mz_G & 0 & mx_G \\ 0 & 0 & m & 0 & -mx_G & 0 \\ 0 & -mz_G & 0 & I_{44} & 0 & I_{46} \\ mz_G & 0 & -mx_G & 0 & I_{55} & 0 \\ 0 & mx_G & 0 & I_{64} & 0 & I_{66} \end{bmatrix} \tag{3.42}$$

$$\mathbf{K} = \begin{bmatrix} 0 & 0 & 0 & 0 & 0 & 0 \\ 0 & 0 & 0 & 0 & 0 & 0 \\ 0 & 0 & \rho g A_w & 0 & -\rho g M_w & 0 \\ 0 & 0 & 0 & \rho g(I_{w1} + V_{ZB}) & 0 & \rho g(I_{w2} + V_{ZB}) \\ 0 & 0 & -\rho g M_w & 0 & 0 & 0 \\ 0 & 0 & 0 & \rho g(I_{w2} + V_{ZB}) & 0 & 0 \end{bmatrix} \tag{3.43}$$

where m denotes the body mass and (x_G, y_G, z_G) represents the center of gravity. The roll, pitch, and yaw moments of inertia are given by I_{44}, I_{55}, and I_{66} respectively, with the roll-yaw moment of inertia satisfying the symmetry relation $I_{46} = I_{64}$. Additionally, A_w corresponds to the water plane area, while M_w is the first moment of the water plane about the y-axis. The second moments of the water plane about the x-axis and y-axis are denoted as I_{w1} and I_{w2}, respectively. Furthermore, V represents the underwater volume and z_B the vertical center of buoyancy.

Once the response amplitudes in six degrees of freedom of each ship are determined, the wave elevation on the free surface can be calculated using the dynamic free surface boundary condition expressed as:

$$\begin{aligned}\zeta = \sum_{n=0}^{N} \frac{1}{g} &\left[i\omega_e \Re \left(\eta_j^n \varphi_j^n + \eta_0^n \varphi_0^n + \eta_7^n \varphi_7^n \right) \right. \\ &\left. + \nabla(\varphi_s - U\mathbf{x}) \cdot \nabla \Re \left(\eta_j^n \varphi_j^n + \eta_0^n \varphi_0^n + \eta_7^n \varphi_7^n \right) \right], \quad j = 1, 2, \ldots, 6.\end{aligned} \tag{3.44}$$

where η_7 represent the amplitudes of the diffraction wave, respectively. The wave amplitude can be calculated by :

$$|\zeta| = \sqrt{\mathrm{Re}(\zeta)^2 + \mathrm{Im}(\zeta)^2} \tag{3.45}$$

3.3 Numerical implementation

The panel method (Erickson, 1990) is a widely used numerical technique for calculating potential flow, divided into the constant panel method and the higher-order panel method. The constant panel method is advantageous due to its simplicity and ease of implementation. However, accurately modeling complex geometries requires a large number of panels, making it computationally intensive. The higher-order panel method addresses this limitation by achieving the same accuracy with fewer panels but complicates the eveluation of influence coefficients.

Since its introduction by Hess and Smith (1964), the constant panel method has been widely used to predict hydrodynamic loads on ships and offshore structures. In this thesis, the constant panel method is used to discretize the boundary integral. Exact formulas are derived to calculate the velocity components at spatial points induced by a planar quadrilateral source element with unit source density.

3.3.1 Rankine source panel method

When discretizing the boundary integral, two common methods are the Rankine source method and the free surface Green function method. The Rankine source method requires distributing singularity sources on the body surface, free surface, and control surface, which leads to high computational demands. In contrast, the free surface Green function method only requires singularity sources on the body surface, making it more computationally efficient. However, for ship-ship traveling with forward speed, the Rankine source method proves to be more accurate than the free surface Green function method (von Graefe et al., 2015).

Figure 3.2 illustrates the distribution of the collocation point and the quadrilateral panel. Two sets of coordinate systems are used: the reference coordinate system $O-XYZ$, which handles the input data and influence coefficients, and the element coordinate system $O'-\xi\eta\zeta$, which is used for calculating the exact induced velocity components. The source density of panel Q is denoted as $\sigma(Q)$. The distance between the center of the source panel and the field point is calculated by

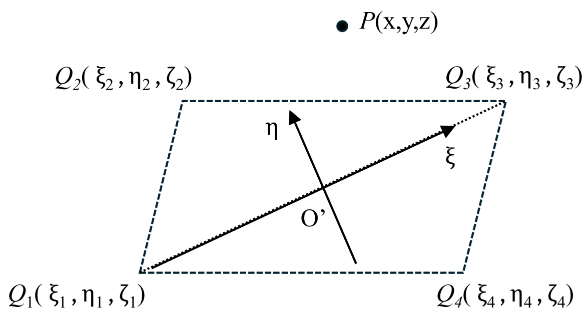

Figure 3.2: Quadrilateral element coordinate system.

$$r=\sqrt{(x-\xi)^2+(y-\eta)^2+(z-\zeta)^2} \tag{3.46}$$

The expression of the Rankine source is given by

$$G(\vec{\boldsymbol{X}},\vec{\boldsymbol{\xi}})=\frac{1}{r}+\frac{1}{r'}, \tag{3.47}$$

where the source point $\vec{\boldsymbol{X}}=(x,y,z)$ and the field point $\vec{\boldsymbol{\xi}}=(\xi,\eta,\zeta)$. Here, the method of images is adopted to consider the sea bottom boundary condition. The second term on the right hand represents the distance between the image source point and the field point, where

$$r' = \sqrt{(x-\xi)^2 + (y-\eta)^2 + (z+2h+\zeta)^2} \tag{3.48}$$

The velocity potential at Point P induced by the panel Q is expressed as

$$\varphi_{Q,P} = \sigma(Q) \iint_Q G_{Q,P} \, d\xi \, d\eta \tag{3.49}$$

Given that $\sigma(Q)$ is a constant, the velocity components at point P are:

$$\frac{\partial \varphi_{Q,P}}{\partial \xi} = \sigma(Q) \iint_Q \frac{\partial G_{Q,P}}{\partial \xi} \, d\xi \, d\eta \tag{3.50}$$

$$\frac{\partial \varphi_{Q,P}}{\partial \eta} = \sigma(Q) \iint_Q \frac{\partial G_{Q,P}}{\partial \eta} \, d\xi \, d\eta \tag{3.51}$$

$$\frac{\partial \varphi_{Q,P}}{\partial \zeta} = \sigma(Q) \iint_Q \frac{\partial G_{Q,P}}{\partial \zeta} \, d\xi \, d\eta \tag{3.52}$$

Hess and Smith (1964) derived the accurate solutions of the above integrals:

$$\frac{\partial \varphi_{Q,P}}{\partial \xi} = -\sigma(Q) \cdot \sum_{i=1}^{4} \frac{\eta_{i+1} - \eta_i}{l_{i,i+1}} \ln \frac{r_i + r_{i+1} + l_{i,i+1}}{r_i + r_{i+1} - l_{i,i+1}} \tag{3.53}$$

$$\frac{\partial \varphi_{Q,P}}{\partial \eta} = \sigma(Q) \cdot \sum_{i=1}^{4} \frac{\xi_{i+1} - \xi_i}{l_{i,i+1}} \ln \frac{r_i + r_{i+1} + l_{i,i+1}}{r_i + r_{i+1} - l_{i,i+1}} \tag{3.54}$$

$$\frac{\partial \varphi_{Q,P}}{\partial \zeta} = \sigma(Q) \cdot \sum_{i=1}^{4} \left(\arctan \frac{m_{i,i+1} e_i - h_i}{z r_i} - \arctan \frac{m_{i,i+1} e_{i+1} - h_{i+1}}{z r_{i+1}} \right) \tag{3.55}$$

$$\varphi_{Q,P} = \sigma(Q) \cdot \sum_{i=1}^{4} \frac{(\xi_{i+1} - \xi_i)(y - \eta_i) - (\eta_{i+1} - \eta_i)(x - \xi_i)}{l_{i,i+1}} \times \ln \frac{r_i + r_{i+1} + l_{i,i+1}}{r_i + r_{i+1} - l_{i,i+1}} + z \cdot \frac{\partial \varphi_{Q,P}}{\partial \zeta} \tag{3.56}$$

where

$$r_i = \sqrt{(x-\xi_i)^2 + (y-\eta_i)^2 + Z^2} \tag{3.57}$$

$$l_{i,i+1} = \sqrt{(\xi_{i+1} - \xi_i)^2 + (\eta_{i+1} - \eta_i)^2} \tag{3.58}$$

$$m_{i,i+1} = \frac{\eta_{i+1} - \eta_i}{\xi_{i+1} - \xi_i} \tag{3.59}$$

$$e_i = z^2 + (x - \xi_i)^2 \tag{3.60}$$

$$h_i = (y - \eta_i)(x - \xi_i) \tag{3.61}$$

It should be noted that in Eq. 3.55, a singular value occurs as the point P approaches a position in the same plane as the panel Q. In such a case,

$$\frac{\partial \varphi_{Q,P}}{\partial \zeta} = \begin{cases} 2\pi, & \text{if } P \text{ is within the quadrilateral;} \\ 0, & \text{otherwise.} \end{cases} \tag{3.62}$$

For the free surface boundary conditions, the second partial derivatives of the velocity potential are required. The accurate solutions of these derivatives are as follows:

$$\frac{\partial^2 \varphi_{Q,P}}{\partial \xi^2} = -2z\sigma(Q) \cdot \sum_{i=1}^{4} \frac{(\eta_{i+1} - \eta_i)(r_i + r_{i+1})}{r_i r_{i+1} \left[(r_i + r_{i+1})^2 - l_{i,i+1}^2 \right]} \tag{3.63}$$

$$\frac{\partial^2 \varphi_{Q,P}}{\partial \eta^2} = 2z\sigma(Q) \cdot \sum_{i=1}^{4} \frac{(\xi_{i+1} - \xi_i)(r_i + r_{i+1})}{r_i r_{i+1} \left[(r_i + r_{i+1})^2 - l_{i,i+1}^2 \right]} \tag{3.64}$$

$$\frac{\partial^2 \varphi_{Q,P}}{\partial \zeta^2} = -2\sigma(Q) \cdot \sum_{i=1}^{4} \frac{[(\xi_{i+1} - \xi_i)(y - \eta_i) - (\eta_{i+1} - \eta_i)(x - \xi_i)](r_i + r_{i+1})}{r_i r_{i+1} \left[(r_i + r_{i+1})^2 - l_{i,i+1}^2 \right]} \tag{3.65}$$

The above implementation is performed in the elemental coordinate system and requires a transformation matrix to transform all physical quantities to the reference coordinate system.

Figure 3.3 illustrates the discretization of the entire boundaries into numerous quadrilateral panels. The body surface, free surface, and control surface are divided into N_b, N_f, and N_c panels respectively, with a total of N' panels.

$$S = \sum_{j=1}^{N_b} \Delta s_j + \sum_{j=1}^{N_f} \Delta s_j + \sum_{j=1}^{N_c} \Delta s_j \tag{3.66}$$

The velocity potential at any point $\vec{\mathbf{x}}_i$ on the boundary of the computational domain is given by

$$\varphi(\vec{\boldsymbol{X}}_i) = \sum_{j=1}^{N'} \sigma_j \iint_{S_b+S_f+S_c} G(\vec{\boldsymbol{X}}_i, \vec{\boldsymbol{\xi}})\, dS_\xi = \sum_{j=1}^{N'} \sigma_j G_{i,j}, \quad i = 1, 2, \ldots, N', \tag{3.67}$$

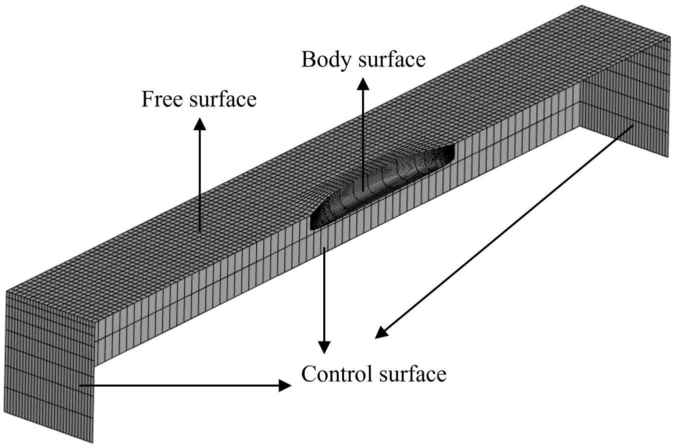

Figure 3.3: Boundary discretization.

The influence coefficients $G_{i,j}$ can be determined using analytical formulas derived from Eq. 3.56. Similarly, the other components in the boundary integral formulations for both velocity and acceleration can be expressed as follows:

$$\frac{\partial \varphi}{\partial n}(\vec{\boldsymbol{X}}_i) = 2\pi\sigma_i + \sum_{\substack{j=1 \\ j\neq i}}^{N'} \sigma_j \iint_{S_b+S_f+S_c} \frac{\partial}{\partial n_i} G(\vec{\boldsymbol{X}}_i, \vec{\boldsymbol{\xi}}) dS_\xi = 2\pi\sigma_i + \sum_{\substack{j=1 \\ j\neq i}}^{N'} \sigma_j G^n_{i,j}, \tag{3.68}$$

$$\frac{\partial \varphi}{\partial x}(\vec{\boldsymbol{X}}_i) = 2\pi\sigma_i + \sum_{\substack{j=1 \\ j\neq i}}^{N'} \sigma_j \iint_{S_b+S_f+S_c} \frac{\partial}{\partial x_i} G(\vec{\boldsymbol{X}}_i, \vec{\boldsymbol{\xi}}) dS_\xi = 2\pi\sigma_i + \sum_{\substack{j=1 \\ j\neq i}}^{N'} \sigma_j G^x_{i,j}, \tag{3.69}$$

$$\frac{\partial \varphi}{\partial z}(\vec{\boldsymbol{X}}_i) = 2\pi\sigma_i + \sum_{\substack{j=1 \\ j\neq i}}^{N'} \sigma_j \iint_{S_b+S_f+S_c} \frac{\partial}{\partial z_i} G(\vec{\boldsymbol{X}}_i, \vec{\boldsymbol{\xi}}) dS_\xi = 2\pi\sigma_i + \sum_{\substack{j=1 \\ j\neq i}}^{N'} \sigma_j G^z_{i,j}, \tag{3.70}$$

$$\frac{\partial^2 \varphi}{\partial x^2}(\vec{\boldsymbol{X}}_i) = \sum_{j=1}^{N'} \sigma_j \iint_{S_b+S_f+S_c} \frac{\partial G(\vec{\boldsymbol{X}}_i, \vec{\boldsymbol{\xi}})}{\partial x_i^2} dS_\xi = \sum_{j=1}^{N'} \sigma_j G_{i,j}^{xx}, \quad i = 1, 2, \ldots, N' \tag{3.71}$$

The influence coefficients $G_{i,j}^{n}$, $G_{i,j}^{x}$, and $G_{i,j}^{z}$ can be determined from Eqs. 3.53 to 3.55, and $G_{i,j}^{xx}$ is obatained by Eqs. 3.63 to 3.65. By applying Eqs. 3.67 to 3.71 to the boundary conditions of the body, free, and control surfaces, an equation system for the source density σ can be established as follows:

$$[\mathbf{P}_{i,j}]\,\{\boldsymbol{\sigma}_j\} = [\mathbf{Q}_i]\,, \quad i = 1, 2, \ldots, N; \quad j = 1, 2, \ldots, N \tag{3.72}$$

where $\mathbf{P}_{i,j}$ represents the coefficient matrix and $\mathbf{Q}_i$ is the matrix comprising the boundary conditions for each panel. Once $\boldsymbol{\sigma}_j$ is determined, the potential, velocity, and acceleration at any point within the computational domain can be calculated using Eqs. 3.67 to 3.71.

3.3.2 Difference scheme

In numerical calculations, the wave elevation can become unstable if it relies solely on the exact solutions derived from Eqs. 3.53 to 3.71 without implementing preventive measures. Because of the high concentration of fast-moving fluid particles in certain areas, particularly near the wave crests, saw-tooth patterns were superimposed on the physical waves. To address this instability, a common solution is to introduce a low-pass numerical filter (Huang, 1997). Another effective technique is to apply difference schemes to the free surface boundary conditions.

Two widely adopted approaches are the upwind difference scheme and the central difference scheme. The upwind difference scheme relies on points from the upstream side, whereas the central difference scheme incorporates points from both sides of the desired derivative. Bunnik (1999) conducted an analysis on numerical damping and dispersion to assess the reliability of these schemes. Yuan (2014) examined the stability of these schemes by analyzing wave patterns on the free surface. Both studies concluded that the upwind difference scheme tends to provide better results compared to the central difference scheme. Bunnik (1999) explained this through physical phenomena, noting that new information about wave patterns predominantly originates from the upstream side, especially at high speeds, while the downstream side primarily contains outdated information.

In this thesis, the upwind difference scheme is employed to address numerical instability. The tangential space derivatives of the potential on the free surface are represented by:

$$\frac{\partial \varphi}{\partial x}(\vec{\boldsymbol{X}}_i) = \frac{\varphi_{(\vec{\boldsymbol{X}}_{i+1})} - \varphi_{(\vec{\boldsymbol{X}}_i)}}{\Delta x} \tag{3.73}$$

$$\frac{\partial^2 \varphi}{\partial x^2}(\vec{\boldsymbol{X}}_i) = \frac{1}{\Delta x^2}\left[\frac{1}{4}\varphi_{(\vec{\boldsymbol{X}}_{i+4})} - 2\varphi_{(\vec{\boldsymbol{X}}_{i+3})} + \frac{11}{2}\varphi_{(\vec{\boldsymbol{X}}_{i+2})} - 6\varphi_{(\vec{\boldsymbol{X}}_{i+1})} + \frac{9}{4}\varphi_{(\vec{\boldsymbol{X}}_i)}\right] \tag{3.74}$$

3.3.3 Radiation condition

When using the Rankine source method to solve boundary value problems, the computational domain cannot be infinite and must be truncated at a specific boundary. To prevent waves from reflecting and propagating back toward the ship, a special condition must be imposed at this truncation point to absorb the waves. One commonly used method is to implement a damping zone on the free surface, where the damping strength increases linearly from zero at the start of the zone to the maximum at the truncation point, thereby avoiding sudden, discontinuous changes that could cause reflections (Bunnik, 1999). However, for longer wavelengths, the damping zone must be enlarged, which increases the number of panels and the computational time.

Another effective technique is to apply Sommerfeld's radiation condition to a vertical boundary that connects the free surface and the sea bottom, known as the control surface (Sommerfeld, 1949). Das and Cheung (2012) improved the Sommerfeld radiation condition by accounting for the Doppler shift of the scattered waves at the control surface, ensuring that all scattered waves normal to the control surface are outgoing. Yuan et al. (2014) further extended Das and Cheung's study to address ship-to-ship interactions with low forward speed. Here, we employed the radiation conditions developed by (Das and Cheung, 2012) on the control surface.

Figure 3.4 illustrates the Doppler shift affecting the scattered wave field generated by a vessel moving at a constant speed U in the positive x direction. As the vessel moves from point B to point O, the scattered waves propagate from point B to point D. The waves reaching point D on the control surface are rotated by an angle θ from the radial axis. Denoting the velocity of the scattered waves as c , we have:

$$\frac{BD}{c} = \frac{BO}{U} \tag{3.75}$$

Let the coordinates at point D be denoted as $(\xi_1, \xi_2, 0)$. The above equation then becomes:

$$\frac{\xi_2 U}{c} = \sqrt{\xi_1^2 + \xi_2^2}\sin\theta \tag{3.76}$$

The speed of the scattered waves at point D is given by

$$c = \frac{\omega'}{k'} \tag{3.77}$$

where ω' represents the angular frequency of the scattered waves from a global reference coordinate system, given by

$$\omega' = \omega_e + Uk'\cos\left[\tan^{-1}\left(\frac{\xi_2}{\xi_1}\right) - \theta\right] \tag{3.78}$$

where k' denotes the local wave number at the coordinates $(\xi_1, \xi_2, 0)$ and ω_e represents the encounter frequency in the body-fixed coordinate system. The local dispersion relation for the scattered waves is given by

$$\omega' = \sqrt{gk'\tanh(k'h)} \tag{3.79}$$

When the vessel's speed surpasses the group velocity of the scattered waves, a calm region forms ahead of the vessel, and the potential becomes constant on the corresponding control surface. Due to the Doppler shift, the scattered waves rotate relative to the radial axis by an angle θ, leading to the following expression for the radiation condition.

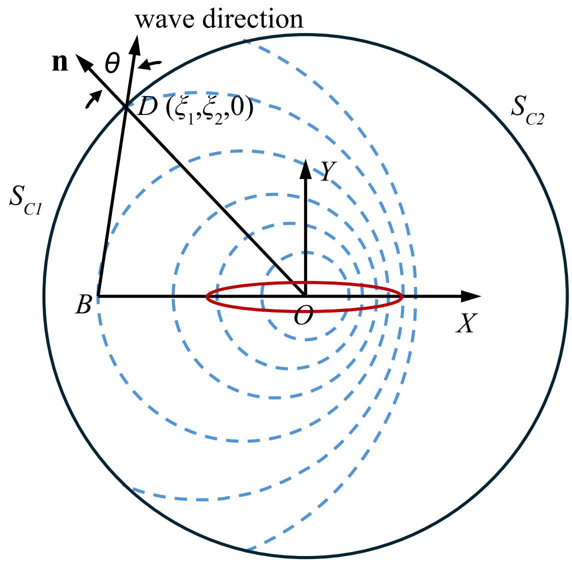

Figure 3.4: Schematic of Doppler shift and control surface radiation conditions.

$$\begin{cases} \dfrac{\partial \varphi}{\partial n} - ik'\varphi\cos\theta = 0 & \text{on } S_{C_1}, \\ \varphi = 0 & \text{on } S_{C_2} \end{cases} \tag{3.80}$$

where S_{C_1} and S_{C_2} represent the sections of S_C with and without the scattering waves, respectively. At zero forward speed, where $\theta = 0$ and $k' = k$, the effects of the Doppler shift disappear, and Eq. 3.80 simplifies to the Sommerfeld radiation condition.

$$\frac{\partial \varphi}{\partial n} - ik\varphi = 0 \quad \text{on } S_C, \tag{3.81}$$

3.4 Summary

Based on the 3-D potential flow theory, the wave-making and seakeeping problems of multi-body interactions are solved using the boundary element method. Specifically, the general formulations of the 3-D potential flow are first introduced, followed by the Rankine source panel method to discretize the boundary integral. Then, the exact solutions of the induced velocity components at points in the flow field are derived. Finally, the upwind difference scheme and radiation conditions are implemented on the free surface and control surface, respectively.

Chapter 4

Wave Interference by Ships Moving in a Single-File Formation

4.1 Introduction

The US Defense Advanced Research Projects Agency has proposed the Sea Train (DARPA, 2020) concept in 2020, closely akin to ducklings in a single file formation. As illustrated in Figure 4.1, it envisages a formation of four or more unmanned surface vehicles aligned in a row to minimize collective wave-making resistance, effectively creating "the equivalent of a long parallel mid-body". Compared to a vessel with an extended parallel mid-body, the formation of multiple shorter ships in single file can offer numerous advantages, such as enhanced mobility, maneuverability, and flexibility. The research of Yuan et al. (2021) and Yuan (2022) indicated that the wave patterns behind ships/ducklings can be replicated by their followers as long as they maintain an optimal position and maintain uniform separation, termed wave-passing. However, this phenomenon raises several intriguing questions:

- Does the wave-passing phenomenon persist if any trailing ships are not in an optimum position?

- Can trailing ships extract more wave energy by increasing the size of the leading ship?
- Can the leading ship extract more wave energy by increasing the size of the trailing ship?
- Will the drag reduction effect of the other ships get better or worse if the position of one trailing ship in the formation changes?

In this chapter, the steady wave interference by ships moving in a single-file formation in calm water is investigated by adopting a boundary element method with linear free surface boundary conditions, i.e. MHydro. The effects of spacing between two ships and the size of the trailing ship on the wave drag reduction are analyzed when one ship follows another. In a formation comprising more than one trailing ship, the phenomenon of wave-passing is further explored, by considering the size of the leading ship, the position of the initial trailing ship, and the optimal positions for each trailing ship.

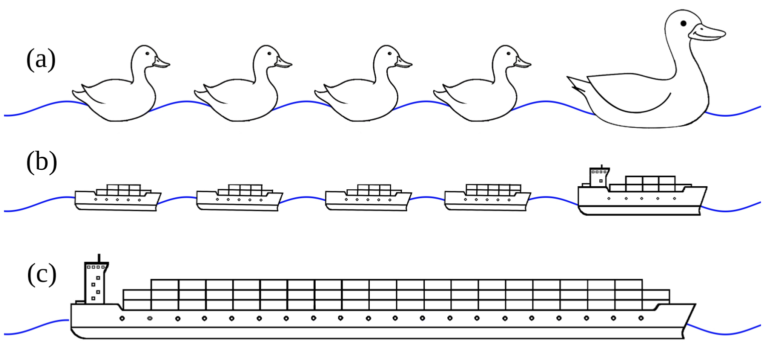

Figure 4.1: Duckling and ships in a single-file formation. (a) Four ducklings following their mother. (b) Four trailing ships following the leading ship. (c) A ship with a very long parallel mid-body.

4.2 Assumptions and simplification of the problem

This thesis mainly focuses on the wave-making resistance, without delving into the analysis of other components of ship resistance. To quantify the wave drag of ships moving in single-file formation, the following assumptions are made:

(1) The frictional resistance depends on the water's viscosity, the surface roughness of the body, and the wetted area. It is assumed that the hull surface is smooth and the hull form is designed to be streamlined. The turbulence in the wake of the leading ship is weak, resulting in no change to the boundary layer of the trailing ships compared to moving individually. Thus, the difference in frictional resistance between sailing alone and sailing in a formation is negligible for vessels moving at the same speed.

(2) The presence of rudders, tail posts, bilge keels, and propeller shaft mounts induces flow separation, leading to the formation of vortices and eddies. However, with proper design, appendage drag and roll damping can be minimized or even reduced to negligible levels.

(3) It is assumed that the ships operate in calm water conditions, with a well-designed substructure to minimize air resistance, making it negligible.

(4) The issue of wave-making can be examined through two perspectives: force and motion. The focus here is on how a ship's resistance changes while in formation movement, excluding aspects related to trimming or sinkage.

(5) It is assumed that the water depth is deep, and therefore the shallow water effect is not taken into account in the numerical calculations.

Based on the above assumptions, it can be inferred that the resistance of a ship mainly originates from two aspects: friction and wave-making. Since the concern here is with the wave-making problem, friction due to viscosity is not considered.

It is worth noting that the leading ship and trailing ships are assumed to move with the same speed and the same direction, so encountering or overtaking between vessels will not occur. In addition, the velocity potential is time-independent in the body-fixed frame. Since the ship moving speed is constant, the hydrodynamic interaction can be handled by a steady state problem. The boundary element method based on a three-dimensional potential flow theory can be used to calculate the wave drag of ships.

The wave drag experienced by a ship moving individually is denoted as R_s and the wave drag of the n-th ship moving in a single-file formation is denoted as R_n. The drag reduction coefficient is defined by

$$C_{DR} = \left(1 - \frac{R_n}{R_s}\right) \times 100\%. \tag{4.1}$$

$C_{DR} > 0$ indicates the wave resistance is reduced in a formation due to the hydrodynamic interaction; whilst $C_{DR} < 0$ represents an increase in wave resistance. No interaction is found at $C_{DR} = 0$, and the wave resistance is the same as that of independent moving. Here, n denotes the number of ships in the formation, and $n = 0$ denotes the leading ship. A value of $C_{DR} = 100\%$ indicates that the wave-making resistance is entirely converted into propulsion force, effectively aiding the ship's motion. Conversely, $C_{DR} = -100\%$ represents a scenario where the wave-making resistance experienced by the ships is doubled compared to ships moving individually.

4.3 Comparison with benchmark experiment

To validate the present code, the case of Wigley-III hull (Journee, 1992) moving on calm water is simulated. The mathematical model is defined as

$$y = \frac{B}{2}\left[1 - \left(\frac{z}{T}\right)^2\right]\left[1 - \left(\frac{2x}{L}\right)^2\right]\left[1 + 0.2\left(\frac{2x}{L}\right)^2\right] \tag{4.2}$$

where L is the ship length , B is the full breadth, and T is the draft, with L/B = 10:1 and B/T = 8:5.

The wave-making resistance coefficient is defined as

$$C_W = \frac{R_s}{\frac{1}{2}\rho U^2 S}, \tag{4.3}$$

where S is the wetted area of the body surface, R_s is the wave making resistance. In Figure 4.2, the results obtained from MHydro are compared with numerical data provided by Xiang and Faltinsen (2011b), as well as experimental results from the

ITTC 1984 (ITTC, 1984), conducted by the Ship Research Institute (SRI) in Tokyo and the University of Tokyo (Tokyo). When the speed is low, some differences between the present results and experimental data are observed. These differences stem from two main factors: First, the Neumann-Kelvin free surface condition used in the in-house code MHydro assumes a constant wetted hull surface, which differs from the experimental setup. Second, the numerical model does not account for higher-order wave resistance components. The performance of the present code could be improved by adopting the Neumann-Michell (NM) theory, as described by Noblesse et al. (2013), and incorporating higher-order terms in the Bernoulli equation. These adjustments would enhance the accuracy of the predictions. While dealing with uncertainty at low speeds remains challenging, the present code offers relatively good results at higher speeds and provides a general trend for the variation of wave-making resistance with changing speed.

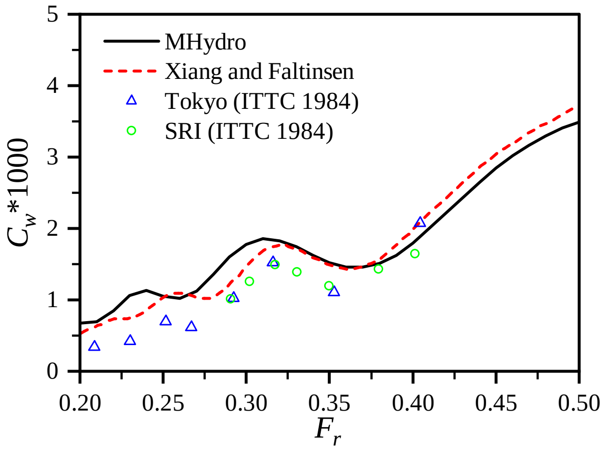

Figure 4.2: Wave making resistance of the Wigley III hull.

4.4 Convergence test

A blunt Wigley hull with $L/B = 5:1$ and $L/T = 10:1$ is adopted in the numerical calculation. The main dimensions of the blunt Wigley III hull are presented in Table 4.1. This ship model will also be employed in the case studies discussed in Chapter 6.

The convergence study analyzes the wave drag reduction of the trailing ship when

Table 4.1: Main dimensions of blunt Wigley III hull

Parameter	**Value**
Length, L (m)	4
Breadth, B (m)	0.8
Draught, T (m)	0.4
Displacement, V (m^3)	0.588
Centre of rotation above base, KR (m)	0.4
Centre of gravity above base, KG (m)	0.26
Radius of inertia for pitch, k_{yy} (m)	1

two identical ships move at $F_r = 0.3$ in a single-file formation with varying gaps. F_r is the Froude number, which can be expressed by

$$F_r = \frac{U}{\sqrt{gL}}. \tag{4.4}$$

The gap between the stern of the leading ship and the bow of the trailing ship is denoted by G_{01}, as illustrated in Figure 4.4. The convergence of the mesh size on the free surface is verified by varying the element size in the x and y directions. Three mesh size schemes are selected, i.e., $L/dx \times B/dy = 30 \times 5$ (coarse mesh), 40×10 (intermediate mesh), 50×15 (fine mesh), where dx and dy denote the length and width of each mesh. In Figure 4.3(a), the differences between fine and medium meshes in the amplitude of the C_{DR} peak values are: $\Delta\mu_1/\mu_{11} = 7.3\%$ and $\Delta\mu_2/\mu_{21} = 10.6\%$. In addition, the differences between fine and medium meshes in the wavelength of the C_{DR} peak values are: $\Delta\chi_1/\chi_{11} = 3.4\%$ and $\Delta\chi_2/\chi_{21} = 3.4\%$. These discrepancies are attributed to the numerical dispersion and damping inherent in the Rankine source method (Kim et al., 2005). For a fair comparison of computational costs, a single case with zero gap between the ships is selected. The computation times for different mesh standards are shown in Table 4.2. As observed in Table 4.2, the computation time increases significantly as the mesh size becomes finer. The time required for a 50 $\times$ 15 mesh is notably longer compared to the smaller dimensions, indicating that the computational cost grows nonlinearly with mesh refinement. For optimal computation accuracy and efficiency, a grid configuration of 40×10 is employed. Similarly, the mesh configuration of $L/dx \times D/dz = 40 \times 10$, where dz represents the mesh size in the

z-direction, is applied to the body surface, with results compared in Figure 4.3(b).

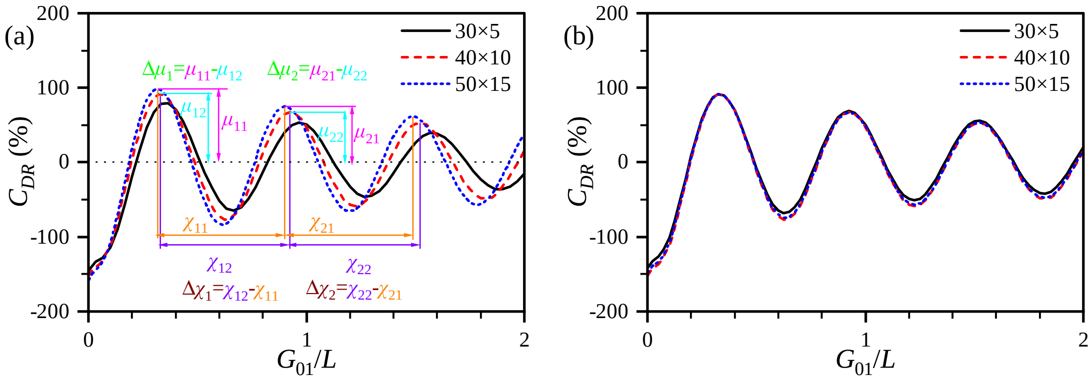

Figure 4.3: Convergence study of mesh size for two ships moving in a single file at $F_r = 0.3$. (a) Free surface; (b) Body surface.

Table 4.2: Computation time for different mesh standards of the free surface

Mesh standard	**Computation time (min:sec)**
30 × 5	2:53
40 × 10	6:31
50 × 15	24:30

Figure 4.4 illustrates the panel distribution of the free surface and wetted body surface of two navigating ships in a single-file formation. To save computational resources, only half of the computational domain is modeled. Additionally, to simulate the full Kelvin wave pattern and to avoid the wave reflection, the computational domain is extended to $1L$ upstream from the center of the leading ship, $3L$ downstream from the center of the trailing ship, and $8B$ sideways from the center of both ships.

4.5 Wave-riding phenomenon

4.5.1 Wave-riding by trailing ships

A single-file ship formation including one leading ship and one trailing ship advancing at $F_r = 0.3$ is investigated. The reduction in wave resistance for each ship can be obtained by placing the leading ship at the origin and by changing the position of the trailing ship from $-1L$ to $-4L$.

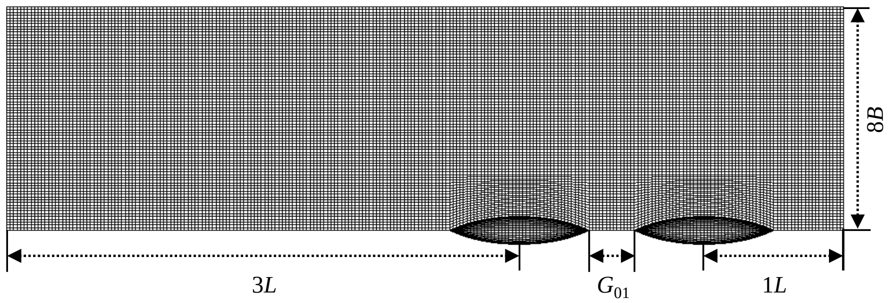

Figure 4.4: Computational domain and panel distribution of two ships navigating in a single file formation. There are 15440 panels distributed over the entire computational domain: 13840 panels on the free surface, 800 panels on the wet surface of each ship.

Figure 4.5(a) illustrates the variations in wave drag reduction for both the leading ship and the trailing ship across different spacings, along with the wave patterns along the centerline in the wake of the leading ship. $C_{DR}0$ represents the wave drag reduction of the leading ship, while $C_{DR}1$ represents the wave drag of the trailing ship. X/L_0 denotes the position of the trailing ship in the local coordinate system of the leading ship. Within the distance range of $-1L$ to $-4L$, the wave drag reduction of the trailing ship demonstrates a periodic oscillation around zero, with the oscillation amplitude decreasing as the distance between the vessels increases. This rate of attenuation is consistent with the diminishing wave patterns generated by the leading ship, which spread and decay as they travel downstream. Notably, when the vessels are in closer proximity, the leading ship benefits from a substantial reduction in wave drag. However, as the gap widens, the leading ship has a diminishing advantage in wave reduction resistance. This is because, at larger gaps, the bow waves generated by the trailing ship have minimal interference with the waves produced by the leading ship.

There are three distinct positions, labelled as A, B, and C, where various wave interference phenomena occur between the two ships. When the trailing ship (positioned at point A) closely follows the leading ship, the wave drag of the leading vessel is reduced by 67%. On the other hand, the trailing ship experiences a wave drag reduction of -152%, which implies that the trailing ship consumes 1.5 times more energy compared to when it navigates independently. As illustrated in Figure 4.5(b), a high-pressure distribution is observed at the stern of the leading ship and the bow of the trailing ship.

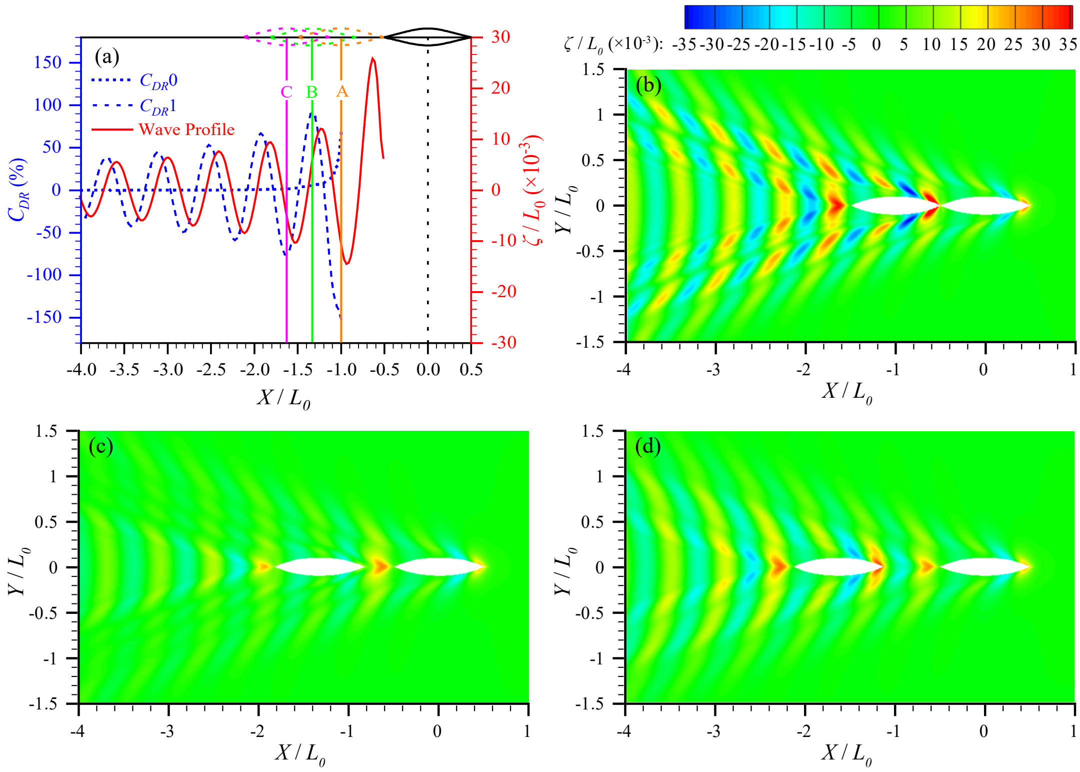

Figure 4.5: Wave drag reduction and wave patterns for both the leading ship and the trailing ship across different spacings. (a) Wave drag reduction of the leading ship (n = 0, blue dot curve) and the trailing ship (n = 1, blue dash curve) with different distances at $F_r = 0.3$. Positions A, B, and C represent the typical positions of wave interference. The wave profile on the center line behind the leading ship is denoted by the red curve. Wave patterns of the trailing ship at (b) Position A, (c) Position B, and (d) Position C, respectively.

This arises due to the superposition of the rear wave generated by the leading ship and the frontal wave produced by the trailing ship. Such a condition proves beneficial for the leading ship in terms of energy conservation, but it is disadvantageous for the trailing ship, impeding its ability to reduce wave resistance.

When the trailing vessel occupies Position B, a win-win scenario arises. The wave drag on the trailing ship is drastically reduced by 91%, indicating that its total wave drag is a mere 9% of that experienced by a solitary ship moving at a similar speed. Simultaneously, the wave drag on the leading ship experiences a reduction of 6%. This mutual benefit is essential for establishing optimal ship formations when attempting to minimize overall wave resistance. Figure 4.5(c) shows the wave pattern when the trailing ship is at position B. The bow of the trailing vessel is positioned at the wave trough, resulting in the cancellation of the bow wave. Conversely, the stern of the trailing vessel is situated at the wave crest, leading to constructive wave interference. The combination of wave cancellation at the bow and wave construction at the stern induces a propulsion force in the vessel, which can counteract much of its own wave resistance.

When the trailing vessel reaches position C, the wave drag experienced by this ship increases by 76%. This phenomenon is depicted in Figure 4.5(d). The phase of the wave generated by the trailing vessel synchronizes with that of the leading ship, resulting in the amplification of the wave amplitude through wave superposition. Consequently, the bow of the trailing ship is positioned atop the crest, whilst its stern resides in the trough. This leads to increased resistance for the ship, which is detrimental to reduce wave drag.

It should be noted that position B is variable, contingent upon the differing velocities. According to Havelock (1908), the wavelength λ on the centerline behind the leading ship is related to the velocity U , which can be expressed by

$$\lambda = \frac{2\pi U^2}{g}. \tag{4.5}$$

Hence, the wavelength has been selected as the primary criterion, given that the complex interplay between the length of a vessel and its corresponding wavelength is important in determining the wave interference observed between two ships.

To minimize the wave drag of the trailing ship, the optimal spacings between the two ships G_{01}/L_0 at different speeds are determined by comparing the wave drag reduction of the trailing ship at different positions. Figure 4.6 illustrates the variations in wave drag experienced by each individual ship as the moving speed increases. The leading ship experiences diminished benefits, with its C_{DR} values approaching zero as the speed increases. The increasing optimal distance between ships with speed, due to the downstream propagation of Kelvin waves, poses a challenge in harnessing wave interference effects. In the C_{DR} values of the trailing ship, three distinct peaks are observed at $F_r = 0.235, 0.29$, and 0.42, which corresponds to λ/L_0 of 0.35, 0.53, and 1.11, respectively. At these specific speeds, the trailing vessel rides approximately 3, 2, and 1 waves, respectively. This allows for sufficient space ahead of the vessel to avoid the wave crests generated by the leading ship, while simultaneously positioning its stern to align with a wave crest.

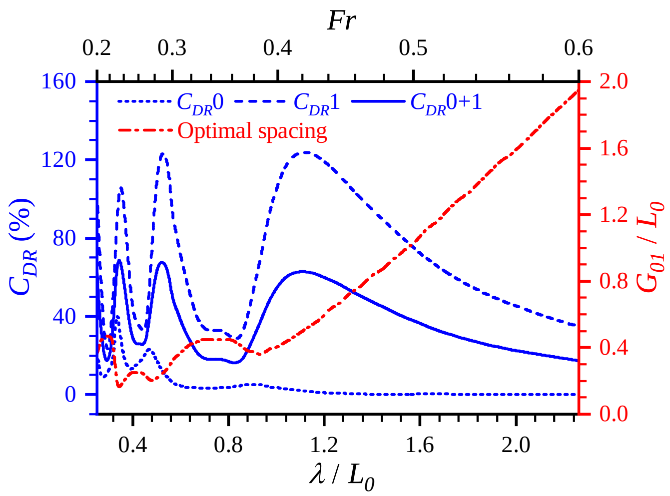

Figure 4.6: Variations in wave drag of the ship formation and optimal distances between two ships for minimizing the wave drag of the trailing ship at different movement speeds.

As depicted in Figure 4.6, when the Froude number exceeds 0.225, the optimal distance between the two ships exhibits an upward, oscillatory pattern with the speed increasing. Additionally, the period of oscillation for the optimal distance markedly lengthens with the increase in movement speed. Figure 4.7 illustrates the progression of optimal distances as the Froude number incrementally rises from 0.285 to 0.385. At $F_r = 0.285$, the trailing ship optimizes its wave-riding benefit by strategically positioning its bow in the trough and its stern on the crest of the wave, despite being in proximity to the stern waves generated by the leading ship. As the speed increases and consequently the wavelength extends, the trailing vessel strategically adjusts its position backwards to ensure its stern aligns with the crest of the wave. This adjustment creates an advantageous pressure differential between the bow and stern, facilitating propulsion. This backward behaviour persists up to a Froude number of 0.325, with the trailing ship attempting to position its stern at the wave crest. At $F_r = 0.345$, the low-pressure zone near the bow wave of the trailing ship starts to approach the low-pressure zone of the leading ship's stern wave. During this phase, positioning the trailing ship's stern closer to the wave crest becomes increasingly difficult. Subsequently, the trailing vessel initiates a forward movement to optimize the alignment of its bow wave's low-pressure zone with that of the leading ship's stern wave. With the further increase in wavelength, the stern of the trailing ship achieves alignment with a wave crest, significantly enhancing the wave-riding effect. This indicates that the adjustment period for the optimal distance of trailing ships experiences a smooth transition from riding on two waves to riding on one wave.

4.5.2 Wave-riding by a leading ship

Various configurations of ships, comprising a leading vessel and a trailing vessel of differing dimensions, are explored. The dimensions of the leading ship remain constant, whilst the size of the trailing ship is proportionally scaled, involving simultaneous alterations in length, breadth, and draught. Here, the scale of the trailing ship relative to the leading ship is indicated by L_1/L_0. As elucidated in chapter 4.5.1, when the trailing ship occupies position A, the leading ship may derive maximal advantage, albeit at the expense of the trailing ship. Conversely, at position B, both the leading and trailing ships may attain mutual benefits. Specifically, the leading ship receives the greatest wave drag reduction when the trailing ship is at position A, while the trailing ship experiences its peak C_{DR} at position B. Consequently, positions A and B are selected for the investigation of the dimensions of the trailing ship on the wave resistance of the leading ship, under varying travel speeds.

Table 4.3: Typical positions of the trailing ship

Position	**Gap between ships**	**Wave interference**	**Benefit**	**Loss**
A	Zero	Constructive	Leading ship	Trailing ship
B	Variable	Destructive	Both leading and trailing ships	None

Figures 4.9(a) and (b) depict the variation in wave resistance of the leading ship as the size of the trailing ship increases from 0.5 to 2.5, positioned respectively at locations

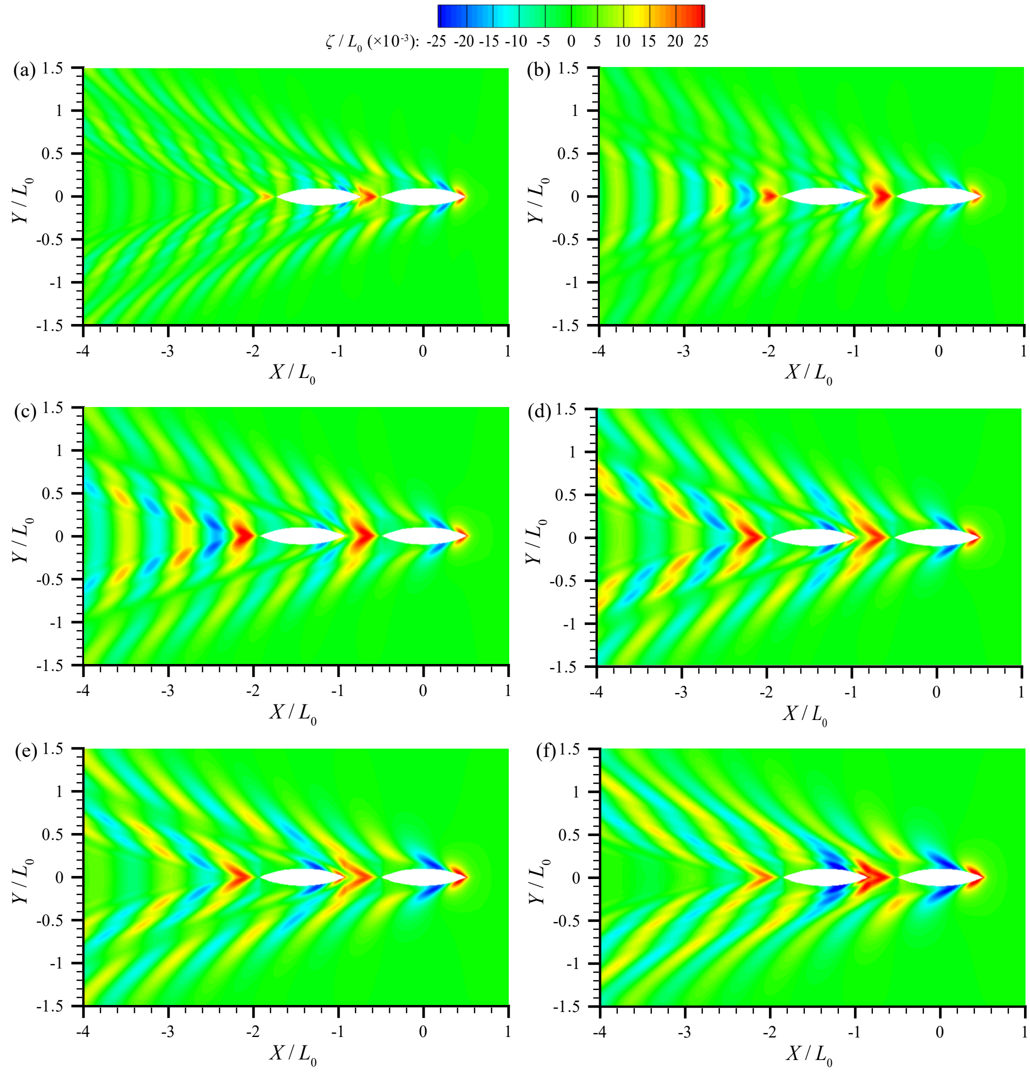

Figure 4.7: Wave patterns of a ship formation, when the trailing ship is at its optimal positions for varying Froude numbers (a) 0.285, (b) 0.305, (c) 0.325, (d) 0.345, (e) 0.365, (f) 0.385, respectively.

A and B. The wavelengths generated by the leading or trailing ship at various velocities are quantified without dimension, in relation to the length of the leading ship, with a range incrementing from 0.25 to 2. The non-dimensional speed (F_r) corresponding to the wavelengths are labelled on the top axis. Owing to the constraints in numerical calculation mesh size, the optimal position B is not ascertained with absolute precision. The selection of the mesh size depends on both numerical accuracy and computational cost. The optimal position of the trailing ship on the free surface cannot be determined with absolute precision due to the mesh size limitations. The mesh size affects the distribution of computational nodes, and this discretization introduces an error in determining the exact position of the trailing ship. Figure 4.8 illustrates the positions of the trailing ship, with P0 representing the precise optimal position for minimizing wave drag reduction, and P1, P2, and P3 representing the ship's positions when centered on three different mesh nodes. As shown, the trailing ship cannot be positioned exactly at P0, as it can only move forward or backward by one mesh node. This introduces an error, but the optimal position lies within the range defined by P1, P2, and P3. Therefore, the wave drag reduction at the optimal position P0 can be approximated by averaging the wave drag reduction values at these three positions. Consequently, an error bar is applied when analysing the position B. However, the gap is zero when the trailing ship is at position A. Thus, there is no need to use an error bar when analysing the position A. The error bar is defined by

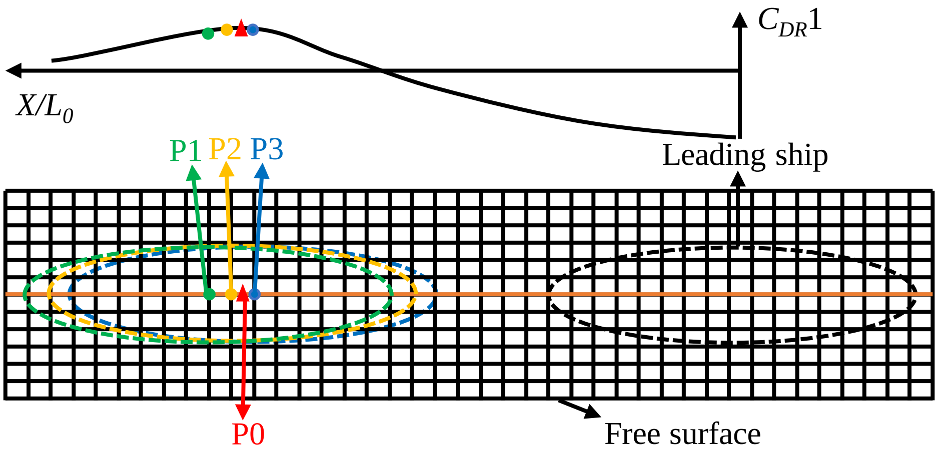

Figure 4.8: Mesh scheme of the in-house code MHydro.

$$\text{Error} = \sqrt{\frac{\sum_{i=1}^{m}(C_{DR_i} - \overline{C_{DR}})^2}{m-1}}. \tag{4.6}$$

Since the optimal position of the trailing ship may not align with a single mesh node, three consecutive mesh positions are considered to ensure the optimal position is covered within this range. The C_{DR} values for each ship are calculated by considering three consecutive mesh positions.Thus, $m = 3$ is used in the error bar calculation and $\overline{C_{DR}}$ represents the mean value of these three C_{DR} values.

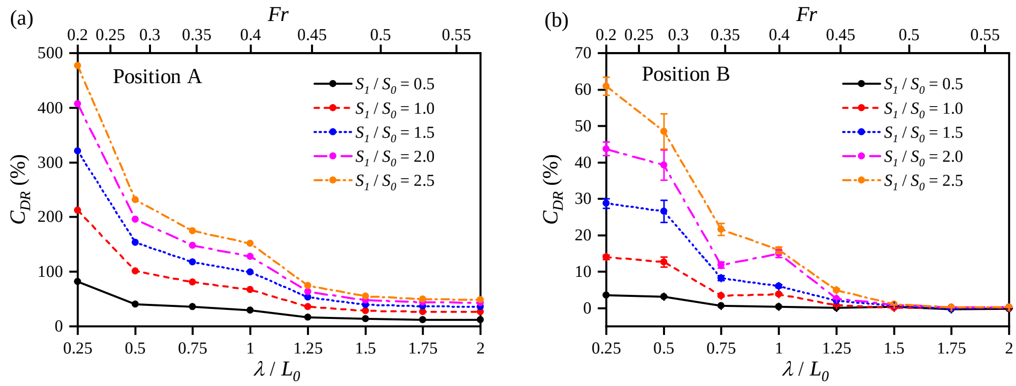

Figure 4.9: Effect of the size of the trailing ship on the drag of the leading ship when the trailing ship is at different positions. (a) Position A; (b) Position B.

At both positions, as the size ratio L_1/L_0 increases, the wave drag reduction tends to increase, especially noticeable for lower travelling speeds. However, there is a large difference in the scale of wave drag reduction between the two positions. Position A exhibits a much higher percentage change in wave drag reduction across all size ratios and speeds compared to Position B. At $\lambda/L_0 = 0.25$, the wave drag reduction values range from 80% to 480% at Position A, whereas the values range from 8% to 60% at Position B. Upon examination of Figure 4.10(a), it becomes apparent that the wave energy present at Position A is considerably greater than that at Position B, particularly within the high-pressure region at the stern of the leading vessel.

At position A, the C_{DR} value of the trailing ship is around 480% with $\lambda/L_0 = 0.25$ and $L_1/L_0 = 2.5$. When the C_{DR} value is over 100%, the wave-making resistance is entirely converted into propulsion force. This indicates the trailing ship does not require any energy expenditure to move forward. Conversely, when the size ratio is 0.5, the propulsion force transmitted from the trailing ship is capable to offset approximately 80% of the wave drag experienced by the leading ship. As shown in Figure 4.10(b), the high-pressure zone at the stern of the leading ship is more expansive and the energy density significantly greater for a size ratio of 2.5 than for a size ratio of 0.5.

Moreover, as the moving speed increases, there is a substantial decline in the wave

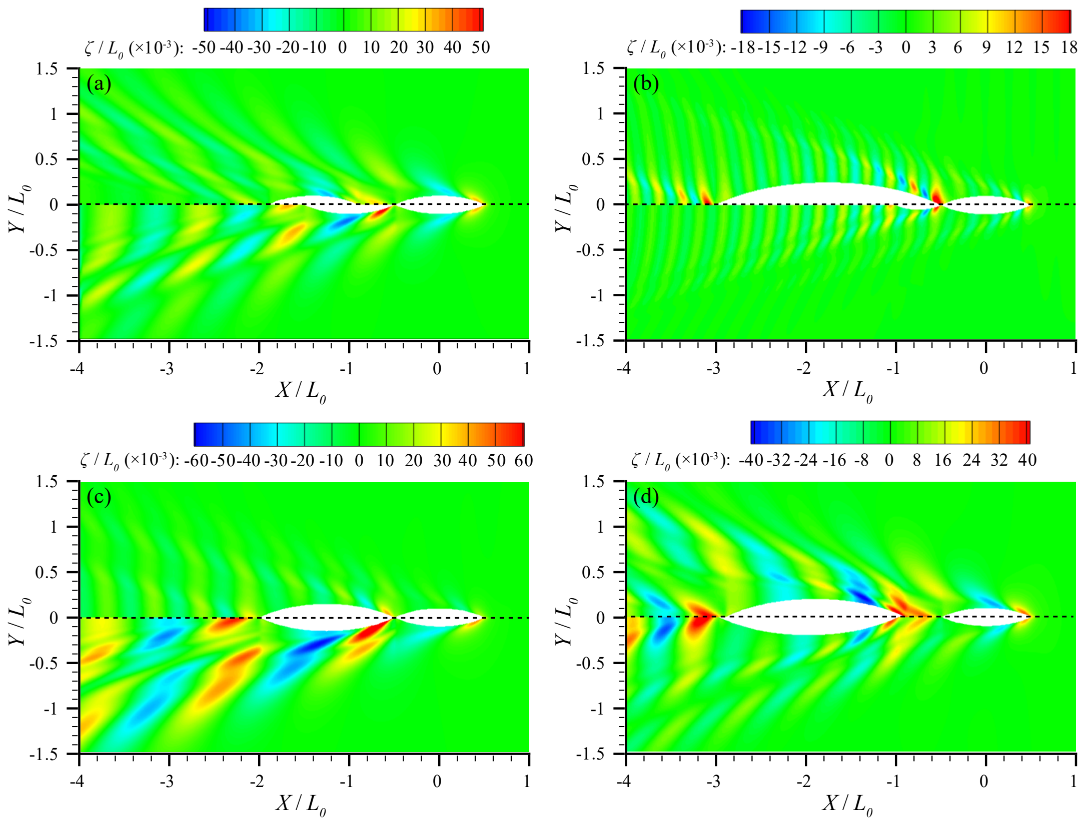

Figure 4.10: Wave patterns of leading ships riding waves generated by trailing ships. (a) Wave patterns of position A (lower) and B (upper) at $\lambda/L_0 = 1$ ($F_r = 0.4$). (b) Wave patterns of $L_1/L_0 = 2.5$ (upper) and 0.5 (lower) at $\lambda/L_0 = 0.25$ ($F_r = 0.2$). (c) Wave patterns of $\lambda/L_0 = 0.5$ ($F_r = 0.28$)(upper) and 1.5 ($F_r = 0.49$)(lower) with $L_1/L_0 = 1.5$. (d) Wave patterns of $\lambda/L_0 = 1$ ($F_r = 0.4$)(upper) and 0.75 ($F_r = 0.345$) (lower) with $L_1/L_0 = 2$.

drag reduction across each size ratio. Concurrently, the differences in C_{DR} between different size ratios diminish, and the curves tend to converge. Figure 4.10(c) offers a comparative visualization of the wave patterns of $\lambda/L_0 = 0.5$ and 1.5 with $L_1/L_0 = 1.5$. The convergence of the C_{DR} is highly relevant to how we define C_{DR} in Equation 4.1. At lower speed (λ/L_0 is small), the denominator in Equation 4.1 is small. A fluctuation of the numerator, which is highly relevant to the hydrodynamic interaction, could result in a very large C_{DR}. As the speed increases, the wave resistance of the trailing and leading ship both increases dramatically. The interaction also becomes more intense. At different moving speeds, the wave drag reduction values stabilize and converge to a constant value, indicating higher speeds will result in more intense hydrodynamic interactions.

Nevertheless, it is observed that some C_{DR} values at lower travelling speeds do not surpass those at higher speeds when at Position B. For instance, the C_{DR} observed at $\lambda/L_0 = 1$ exceeds that at $\lambda/L_0 = 0.75$ for both L_t/L_0 ratios of 2 and 1. This is because the gap between two ships for $\lambda/L_0 = 0.75$ is larger than that for $\lambda/L_0 = 1$, which is detrimental to the formation of a high-pressure zone at the stern of the leading ship, owing to the reduced wave superposition. Figure 4.10(d) illustrates the wave patterns for $\lambda/L_0 = 1$ and 0.75, with a size ratio $L_1/L_0 = 2$, while the trailing ship is at Position B. At $\lambda/L_0 = 1$, the trailing ship is positioned to ride atop two waves. In contrast, for $\lambda/L_0 = 0.75$, the trailing ship is required to move back to take advantage of the wave-riding.

4.6 Wave-passing phenomenon

The research by Yuan et al. (2021) demonstrates how waves generated by a mother duck are passed to its smaller ducklings. Drawing inspiration from this phenomenon, the wave-passing mechanism is now applied to ships moving in a single-file formation. Figure 4.11(a) shows the wave patterns of an optimal ship formation, where the spacing between adjacent ships is nearly uniform. Except for the wave patterns around the first two trailing ships, the wave patterns of the remaining trailing ships are nearly identical and can be replicated sequentially. As shown in Figure 4.11(b), the wave drag reduction for the first two trailing ships is greater than that of the others, with drag reduction for the subsequent ships gradually stabilizing at a constant value. This delicate equilibrium is referred to as the wave-passing. The function of these trailing ships is to sustain and pass the waves to those behind them. Figure 4.11(c) illustrates that, in an optimal "0+7" system, the first seven ships maintain this delicate equilibrium. When a single ship, positioned as the 8th trailing vessel, moves independently, the wave interference between the "0+7" system and the single ship results in wave cancellation. However, as indicated by the wave profiles in Figure 4.11(c), the two wave systems of "0+7" and "8" are not out of phase. The phase angle between them is so delicate that the resultant wave profile of "0+8" is almost identical in amplitude to that of the "0+7" system. When the wave profile of "0+8" shifts upstream by a phase of "G_{78}/L_0", a very good agreement between the wave profiles behind "0+7" and "0+8" is observed, as shown in Figure 4.11(d). This indicates that the waves are successfully sustained and passed over by the "7" trailing ship.

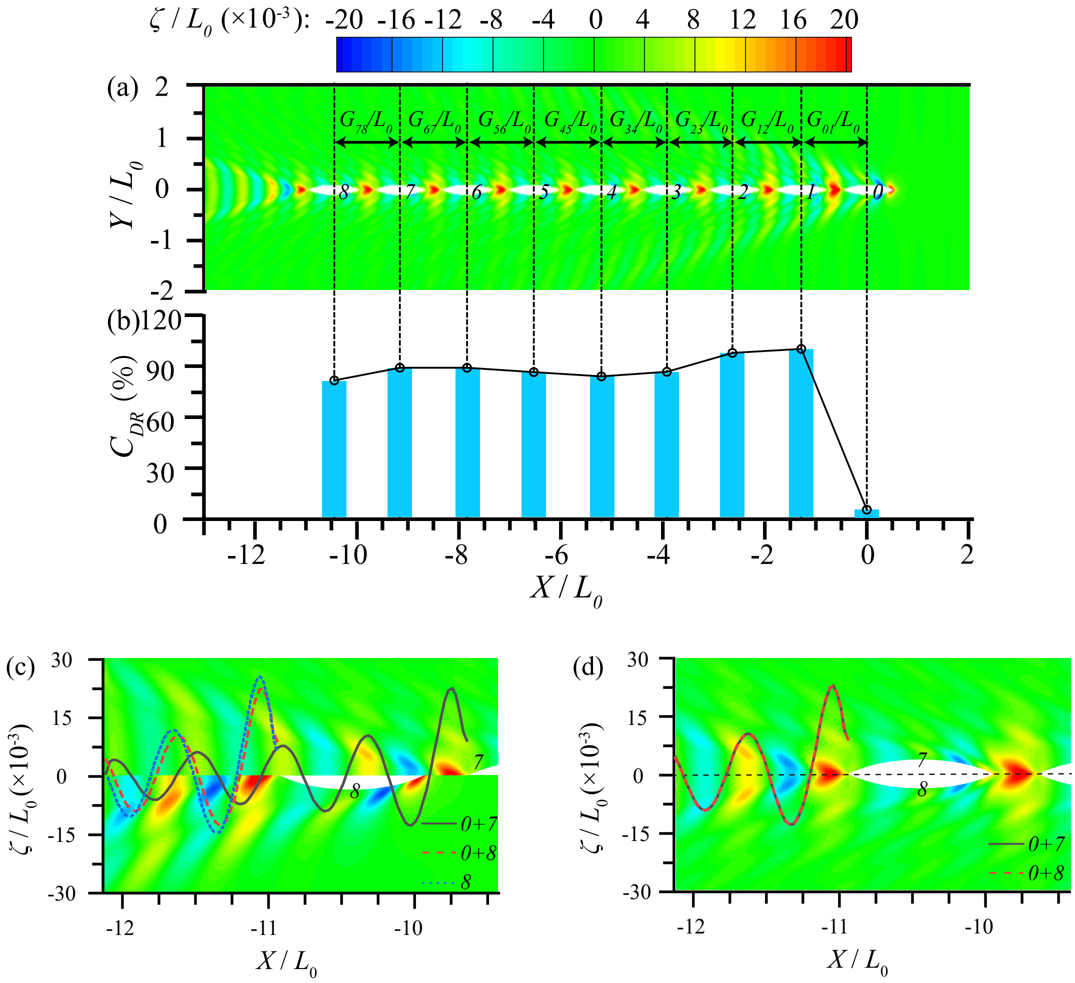

Figure 4.11: Optimum formation of ships moving in a single-file at $F_r = 0.3$: (a) Wave patterns of a leading ship followed by eight trailing ships. (b) Wave drag reduction of each individual ship. (c) Superposition of wave patterns for the entire formation. (d) Comparison of wave patterns between a formation with a leading ship followed by seven ships and one with eight ships.

4.6.1 Waves generated by different leading ships

In designing ship formations, the size of the leading ship is an important factor that influences how much drag reduction can be achieved by the trailing ship. Consequently, in varying ship formations, the leading ship's size is altered while the dimensions of the trailing vessels are maintained constant. The scale of the leading ship relative to the trailing ship is denoted by the ratio L_0/L_1. Since the size of the leading ship is variable, the moving speed is nondimensionalized by the trailing ship's size, with $F_r = 0.3$. The wave drag reduction coefficient C_{DR} of the leading ship and its trailers is shown in Figure 4.12(a). Adjusting the size of the leading ship does not significantly reduce its own drag, with a notable exception for the size ratio $L_0/L_1 = 2.5$. In such a case, the leading ship can receive a wave drag reduction of 25%, whereas its first follower does not achieve similar energy savings compared to other formation arrangement, with the C_{DR} value being 72%. As shown in Figure 4.12(d), a high-pressure zone emerges between the stern of the leading ship and the bow of the trailing ship, because of wave superposition. This situation is advantageous for the leading ship, which rides across four waves, whereas the benefits to the first trailing ship are somewhat diminished.

When the size of the leading ship is smaller than its trailers, e.g. $L_0/L_1 = 0.5$, the leading ship receives a very small pushing force from its trailer with $C_{DR} \approx 5\%$. In such a case, the first trailing ship can receive a wave drag reduction of more than 50%, indicating that it still needs to consume energy to overcome the remaining 50% of wave drag. As shown in Figure 4.12(b), compared with other ship configurations, fewer waves are generated by the leading ships that can be harnessed by the first trailing ship.

It is also observed that the size of the leading vessel could affect the drag of the first few ships. As the trailing number increases, the drag reduction coefficient will ultimately turn to be a steady value. Figures 4.12(b) to (d) illustrate the wave patterns of different formations with L_0/L_1 being 0.5, 1 and 2.5, respectively. The wave patterns observed behind the first few ships in varying formations exhibit significant differences. Conversely, the wave patterns behind the last few trailing ships in any given formation tend to be similar, regardless of the size of the leading ship. These wave patterns

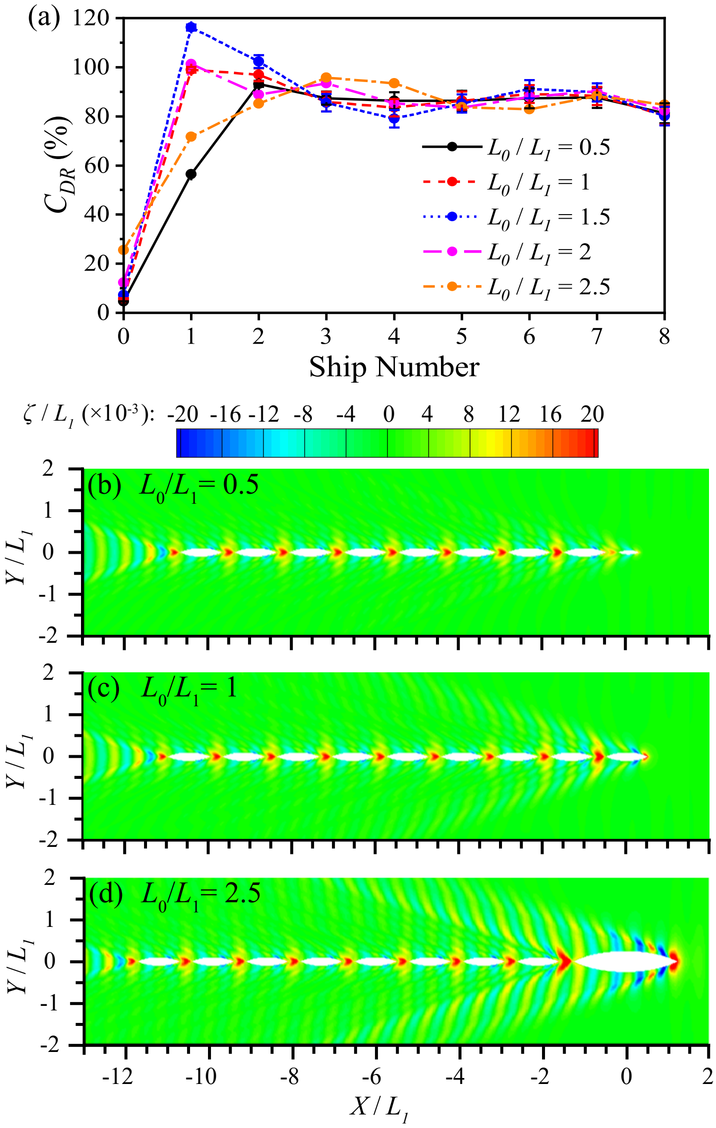

Figure 4.12: Effect of leading ship's size on wave-passing. (a) Variations in wave drag reduction for each ship across various ship formations with different sizes of the leading ship at $F_r = 0.3$. Wave patterns of ship formations with L_0/L_1 being (b) 0.5, (c) 1 and (d) 2.5, respectively. The symbol "0" represents the leading ship, while the symbols "1, 2, . . . " represent the first, second, and subsequent trailing ships.

indicate that enlarging the leading vessel will exert a localized impact on the wave-passing amongst vessels.

For a ship with an infinite parallel section, the wave-making resistance arises from its bow and stern, while the mid-body does not generate waves. In a single-file formation, when the wave drag reduction of the trailing ships is 100%, they do not generate any waves while moving on the water surface. Under such a case, the wave resistance of a single infinitely long ship will be the same as multiple ships in a single-file formation. However, the wave drag reduction coefficient is not always 100%. The wave drag reduction of ships in formations is determined by the moving speed and ship hull design. As shown in Figure 4.12, the wave drag reduction coefficient of each trailing ship is around 90% when dynamic equilibrium is achieved. This indicates that the trailing ships can save about 90% of the energy compared to a single ship moving independently. A 10% gap remains to fully overcome the total wave drag.

4.6.2 Sensitivity study of the first trailing ship's position

It was found that each trailing ship could find its unique optimum position to achieve the maximum wave drag reduction. A dynamic equilibrium status was observed, where the distance between each trailing ship is the same. A question arises: what happens if one of the trailing ships does not stay in its optimum position? Here we adjust the position of the first trailing ship and calculate the drag reduction of each individual in the formation movement. The position of the first trailing ship is normalized by its own length and denoted by X_1/L_1. The results are given in Figure 4.13(a) when the trailing ship moves at $F_r = 0.3$, with L_0/L_1 being 1.5. At the optimal position where $X_1/L_1 = 1.6$, the first trailing ship reaps a significant reduction in drag, indicating an effective harnessing of the leading ship's wave energy. As the position of the first trailing ship shifts afterwards, its wave drag reduction diminishes and can even be negative, suggesting an overshoot of the optimal wave interaction zone.

When the first trailing ship stays at $X_1/L_1 = 1.85$, its C_{DR} drops to -84%, which is the lowest value observed across all configurations. However, this repositioning creates a wave energy pattern that is highly advantageous for the second trailing ship. This ship achieves a C_{DR} of 110%, the highest amongst all configurations. This suggests that while the first trailing ship incurs a significant drag penalty for itself at this spacing, it simultaneously enhances the wave energy conditions for its follower. As shown in Figure 4.13(c), the constructive interference of waves between the leading ship and the

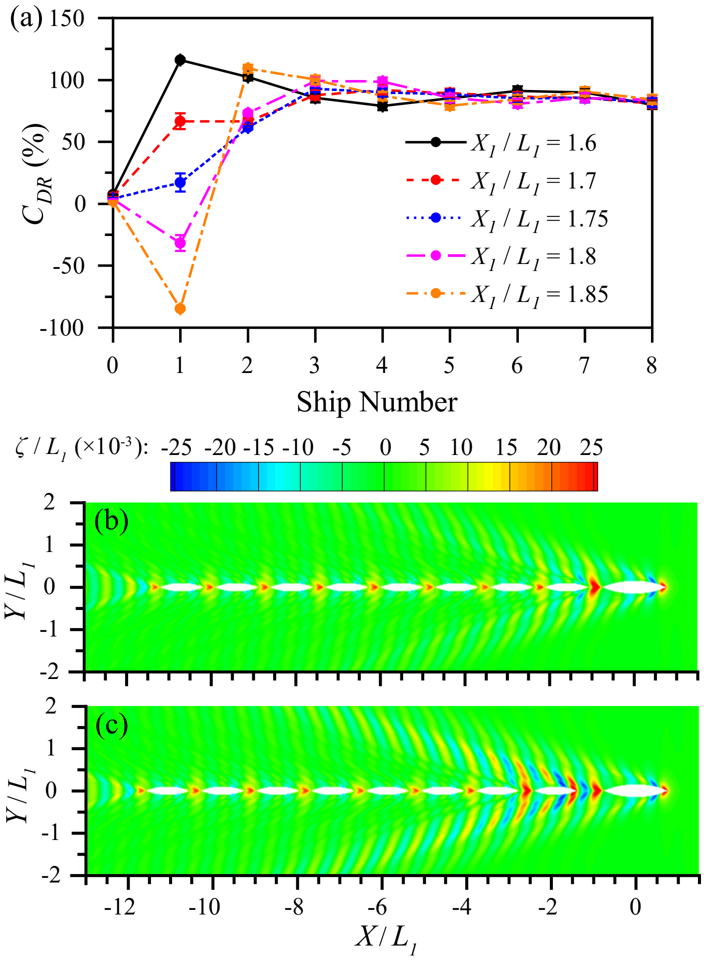

Figure 4.13: Effect of the position of the first trailing ship on wave-passing. (a) Variations in wave drag reduction of each ship in different ship formations with changes of the first trailing ship's position at $F_r = 0.3$, and the position of the leading ship normalized by the length of the leading ship is denoted by X_1/L_1. (b) and (c) Wave patterns of ship formations with X_1/L_1 of 1.6 and 1.85, respectively.

first trailing ship at this specific spacing amplifies the wave energy available to the second trailing ship. The second trailing ship is positioned in such a way that it can effectively ride on the enhanced wave system, resulting in an optimal condition for drag reduction.

The wave patterns depicted in Figures 4.13(b) and (c) reveal that while the wave patterns of the initial ships in two separate formations differ, the patterns of the final ships within these formations are remarkably similar. This observation aligns with

Figure 4.13(a), which demonstrates a trend of convergence in drag reduction across different formations. The proximity of the first trailing ship to the leading ship markedly influences its own drag reduction, as well as that of its immediate followers. However, this impact lessens with distance, leading the entire formation to achieve a dynamic equilibrium.

4.6.3 The stability of wave-passing

By decoupling the overall wave pattern into components produced individually and those generated collectively by other entities, Yuan et al. (2021) explored how wave-passing can be achieved when a delicate phase difference exists between two wave systems. To achieve a dynamic equilibrium, each trailing ship must occupy the optimum position, where the C_{DR} value reaches its maximum. As illustrated in Figure 4.5(a), in addition to the maximum value of C_{DR} there exist several other peak positions that can be exploited to diminish resistance.

Is it possible to still achieve wave-passing when trailing ships occupy alternative peak positions? The optimum position, along with other peak positions for trailing ships within the ship formation, are selected to construct various combinations of positions. The optimum position is marked by '1', while the second and third peak positions are labelled '2' and '3', respectively.

Figure 4.14(a) illustrates the reduction in wave drag experienced by each vessel within various ship formations, travelling at $F_r = 0.3$. When each trailing ship occupies the optimum, second, and third peak positions, respectively denoted as '1-1-1-1-1-1-1-1', '2-2-2-2-2-2-2-2', and '3-3-3-3-3-3-3-3', the drag reduction coefficient for various formations converges to distinct values. This suggests that the wave-passing can be attained when trailing ships are positioned at peak positions other than the optimum position. As illustrated in Figure 4.14(d) and (e), the wave patterns behind each trailing ship can be repeated. Compared to the optimum position, the second and third peak positions shift back by one and two wavelengths, respectively, with the phase differences between the two wave systems increasing by 2π and 4π, respectively. Consequently, the requisite condition for a dynamic equilibrium is still satisfied. In addition, a significantly greater number of radiated waves are observed when the trailing ships occupy third peak positions, as opposed to those positioned at second peaks, which explains why the C_{DR} values of second peak positions than those of third peak positions. The C_{DR} values in these three formations converge to 88%, 60% and 53%, respectively, closely approximating the three peak values depicted in Figure 4.5(a). Thus, based on Figure 4.5(a), the converged values of C_{DR} can be inferred when the trailing vessel occupies different peak positions.

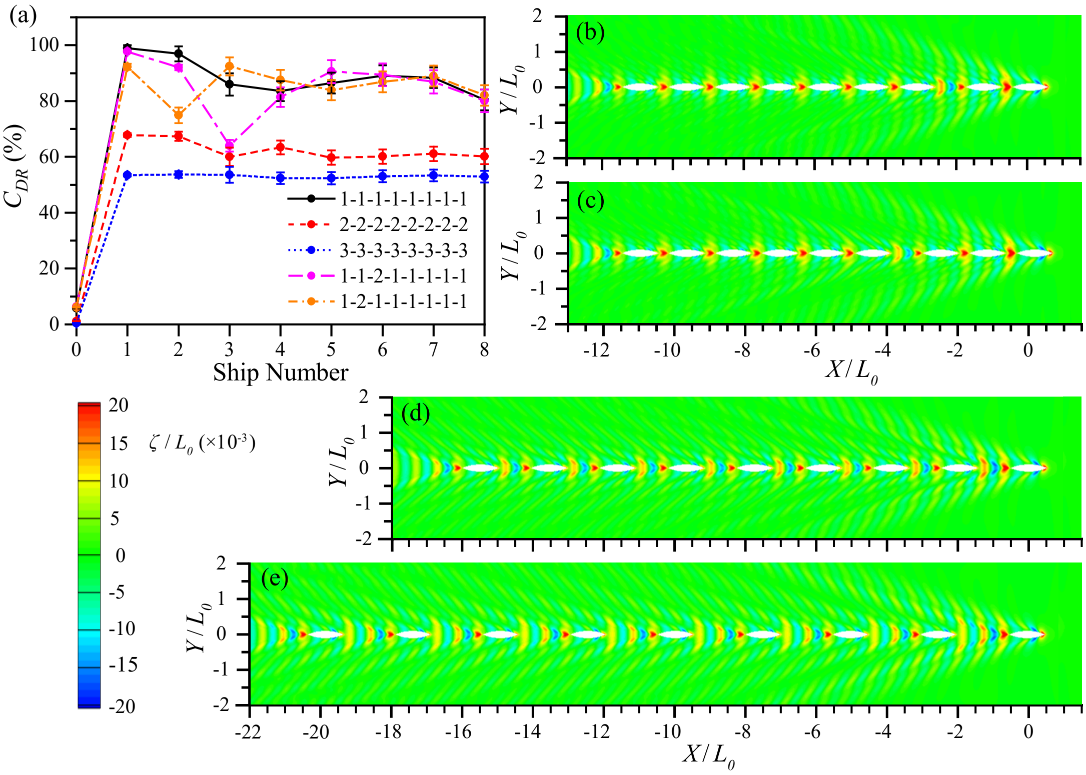

Figure 4.14: Effect of optimal positions of each trailing ship on wave-passing. (a) Variations in wave drag reduction of each ship at different peak positions. The optimum, second and third peak positions are denoted by 1, 2, 3, respectively. Wave patterns of ship formations configured as (b) '1-2-1-1-1-1-1-1', (c) '1-1-2-1-1-1-1-1', (d) '2-2-2-2-2-2-2-2' and (e) '3-3-3-3-3-3-3-3', respectively.

When trailing ships within the one formation occupy varying peak positions, e.g. '1-2-1-1-1-1-1-1' and '1-1-2-1-1-1-1-1', the C_{DR} values will exhibit fluctuations but will ultimately converge to the same value as observed in '1-1-1-1-1-1-1-1'. The C_{DR} values at the second peak position in these two formations closely align with those in the

'2-2-2-2-2-2-2-2' configuration. In both formations, as shown in Figure 4.14(b) and (c), the wave patterns observed behind the last few trailing ships are similar, which is also noticeably akin to the wave patterns in the '1-1-1-1-1-1-1-1' formation depicted in Figure 4.14(c). Figure 4.15 illustrates the wave profiles along y=0 for different ship formations. It shows that the wave profiles around each trailing ship are identical across different formations, indicating that the systems have reached dynamic equilibrium.

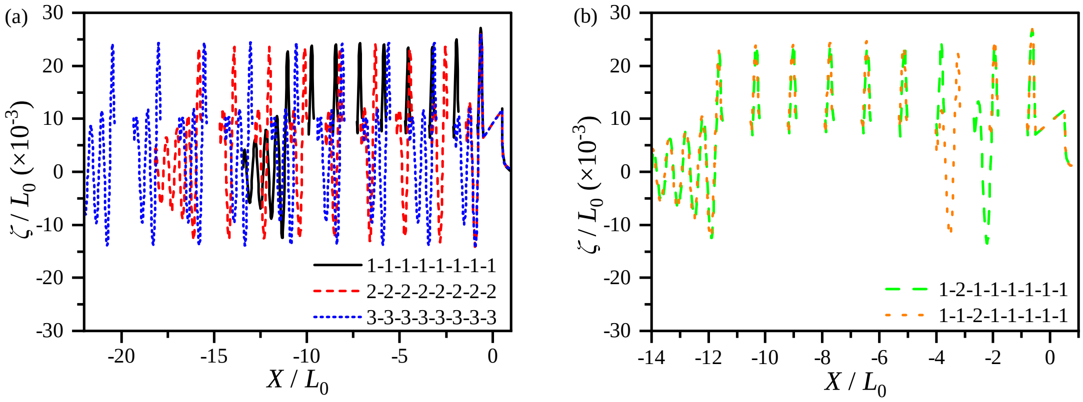

Figure 4.15: Wave profiles along y = 0 for different ship formations. (a) "1-1-1-1-1-1-1-1", "2-2-2-2-2-2-2-2" and "3-3-3-3-3-3-3-3". (b) "1-2-1-1-1-1-1-1" and "1-1-2-1-1-1-1-1".

4.7 Summary

Drawing on the discovery that ducklings use the benefits of wave-riding and wave-passing to reduce wave drag, this chapter analyses the ships moving in a single-file formation. To solve the steady wave interference problems, a 3D boundary element method combined with linearized free-surface boundary condition is adopted. he primary objective of this thesis is to explore the wave drag and wave patterns of ships within different configurations. The blunt Wigley hull model is employed in numerical calculation. After numerical simulations and analyses, some of the main findings of this thesis are summarized as follows.

(1) The position of the first trailing ship determines whether wave drag can be reduced. When positioned at a point of destructive wave interference, a win-win situation arises. The trailing vessel can utilize wave cancellation to reduce drag,

while the leading vessel also experiences a slight reduction in wave drag. Conversely, at a position of constructive wave interference, the wave drag on the trailing ship increases. When the two ships are in close proximity, the leading ship can gain the maximum benefit, whilst the trailing ship may have to sacrifice its own advantage.

(2) Increasing the size of the trailing vessel facilitates a reduction in the wave resistance of the leading vessel by generating a larger high-pressure zone between the two vessels. This effect of wave-riding by the leading ship is more pronounced at relatively low speed states. As speed increases, the effect of increasing the size of the trailing vessel on the wave drag reduction of the leading vessel becomes less significant.

(3) Within a formation, enlarging the leading ship has a localized effect on minimizing the drag experienced by the trailing ships. As the number of trailing ships increases, the ship formation tends to a dynamic equilibrium state.

(4) Changes in the position of individual trailing ships in a formation can have a localized effect on wave-passing. Constructive wave interference detrimentally affects the trailing ship's own drag reduction, requiring more energy to be expended to generate waves. However, this is extremely beneficial to the trailing ship immediately behind, with a more noticeable wave-riding effect.

(5) To achieve wave-passing or to reach dynamic equilibrium, each individual only needs to make sure to occupy the peak positions, which can be the second, third or any other peak position, it doesn't have to be the optimum position.

Chapter 5

Experiments of a Leader-Follower Ship Formation

5.1 Introduction

A comprehensive understanding of the mutual interference between ships, encompassing not only wave interference but also the effects induced by fluid viscosity, is critically important for advancing the study of drag reduction in ship formations. The drag reduction of a ship in formations may be influenced by its hull form; for example, transom sterns and sharp sterns may experience different hydrodynamic interference. Streamlined ships are designed to reduce resistance, while transom stern designs are widely used for commercial vessels due to their ease of construction. The flow separation behind a transom stern is usually accompanied by wave breaking, air entrainment, and bubble plumes (Hendrickson et al., 2019). In addition to utilizing wave interference to reduce drag, the trailing ship may exploit other interferences, such as bubbles or turbulence flow in the wake of the leading ship, to save energy. Motivated by these interesting phenomenon, some critical questions are raised:

- Can we quantify the contributions of wave interference and viscous interference to the total drag reduction?
- How much drag reduction in total can be achieved for formations with different

configurations when considering the viscous effect?

- Does the transom stern design more effectively contribute to drag reduction in ship formations compared to other stern designs?
- What role does the bubble flow generated by a leading ship play in reducing the drag of a trailing ship?

In this chapter, wave and viscous interferences in a leader-follower formation are investigated through a series of experimental tests. It focuses on analysing the resistance of ships in calm water, with the effects of ambient waves on resistance excluded from consideration. The resistance components of each ship in the formation are determined using the form factor method. Furthermore, the total resistance of three different ship models is compared, and the resistance components of one particular model are analyzed with the aid of the in-house code MHydro and the ITTC (1957) correlation line. The complex interference between ships is finally revealed by examining three formations with different configurations, identifying three critical zones in the wake of the leading ship.

5.2 Estimation of resistance components

5.2.1 Resistance components of a single ship

According to the ITTC (1978), the total resistance of a single ship moving steadily on calm water can be expressed by

$$C_T^s = (1 + k) \cdot C_F + C_W + \Delta C_F + C_{AA} \tag{5.1}$$

where C_T^s is the total resistance coefficient, $(1+k)$ is the form factor, C_F is the frictional resistance coefficient, C_W is the wave-making resistance coefficient, ΔC_F is the frictional resistance coefficient caused by roughness, and C_{AA} is the air resistance coefficient. In the experiment, the ship surface is smooth, thereby ΔC_F is zero. The air resistance is also negligible, thus the total resistance can be simplified to

$$C_T^s = (1 + k) \cdot C_F + C_W \tag{5.2}$$

The frictional resistance coefficient C_F can be obtained using ITTC (1957) correction line

$$C_F = \frac{0.075}{(\log Re - 2)^2} \tag{5.3}$$

where Re is the Reynolds number, defined as

$$Re = \frac{UL}{\nu} \tag{5.4}$$

in which U is the ship speed, L is the ship length, and ν is the kinematic viscosity of the water.

When the ship moves at very low speeds, the wave-making resistance becomes negligible. Thus, the form factor can be calculated by:

$$1 + k = \lim_{Fr \to 0} \frac{C_T^s}{C_F} \tag{5.5}$$

The form factor is independent of the scale effect and moving speed (ITTC, 1978). Even though some researchers have challenged this point (Min and Kang, 2010), the method is still adopted in this thesis.

5.2.2 Resistance components of ship formations

The resistance components in a single-file formation are more complicated than those of single ships. Insel (1990) conducted an in-depth analysis of the resistance components of high-speed displacement catamarans, which is helpful for the investigation of ships arranged in a single-file formation. The interaction effect can be divided into two parts:

(1) Viscous interference: The bow waves generated by the trailing ship induce variations in the perturbation velocity field behind the leading ship, consequently modifying the form factor. Furthermore, as the waves from one vessel propagate to another, the

wetted surface area changes, subsequently affecting the skin frictional resistance.

(2) Wave interference: The superposition or cancellation of waves generated by the two ships can result in constructive or destructive interference, significantly impacting the wave resistance experienced by each vessel.

Taking the interference effects into account, the total resistance of the n-th ship in a formation can be expressed by (Insel, 1990)

$$C_T^n = (1 + \alpha k)\beta C_F + \gamma C_W \tag{5.6}$$

where α is the form resistance interference factor, β is the frictional resistance interference factor, and γ is the wave resistance interference factor.

Wave interference refers to the interaction between waves, including wave cancellation or superposition, occurring between bow and stern waves or between waves generated by ships in formations. Generally, "drag" is commonly used in studies involving animals and aerodynamics, while "resistance" is more frequently employed in ship design and naval architecture. In this thesis, the terms "wave drag" and "wave resistance" are used interchangeably and have the same meaning. Based on the definition of the wave drag reduction, the total drag reduction is defined as:

$$C_{DR}^T = \left(1 - \frac{C_T^n}{C_T^s}\right) \times 100\%, \quad n = 0 \text{ and } 1, \tag{5.7}$$

In a leader-follower ship formation, there are only two ships, with n=0 and 1 representing leading and trailing ship, respectively.

5.3 Experimental study of total resistance

5.3.1 Experimental set-up

A series of resistance tests were conducted in the towing tank at the Kelvin Hydrodynamics Laboratory (KHL), University of Strathclyde. The main dimensions of the tank are 76m in length, 4.6m in width, and 2m in depth, respectively. The sloping beach is located at the other end to absorb the reflected waves. In the experimental tests, the ship models were towed by a carriage equipped with a computer-controlled digital drive system, achieving a maximum towing speed of 5m/s.

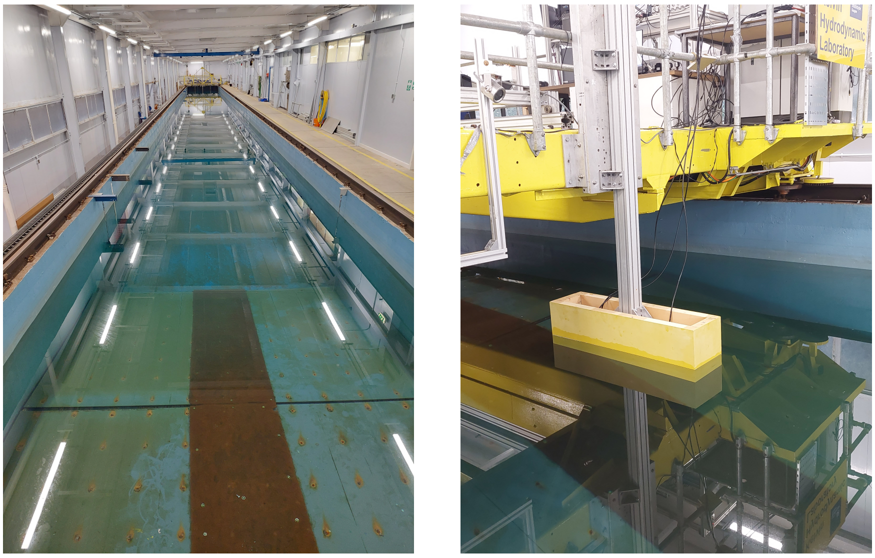

Figure 5.1: The towing tank and the carriage in KHL.

The total resistance measurements were carried out using the CCDXYZ-250KG-US load cells, manufactured by Applied Measurements Ltd. The load cell was mounted on the model's underside, aligning with its centreline. The leading ship model was securely fixed to the front of the carriage, while the trailing ship model was designed to be adjustable by being attached to a sliding frame. When the two ships are mechanically connected, their trim and sinkage motions are influenced by the constraints imposed by the connection, which further impacts their resistance. However, in the experimental tests, both the leading and trailing ships were rigidly fixed, and the effects of trim and sinkage motions were not investigated.

The ship models were accelerated by the carriage from one end of the towing tank, reaching the designed speed after 20 meters. The satisfactory test distance was approximately 30 meters, during which the captured total resistance remained constant. An interval of 15 minutes was allocated between tests to allow for the dissipation of disturbances on the water surface. The PC-based data acquisition system achieved sampling rates of up to 60kHz. Subsequent data analysis and processing were conducted using the commercial software Spike.

Figure 5.2: The load cell mounted on the model and the sliding frame for adjusting the trailing ship.

Figure 5.3 illustrates a leader-follower ship formation advancing in a towing tank with a width of 4 m. The half angle of the Kelvin wave generated at point A is 19.47°, causing the reflected wave from the tank's sidewall to converge at point B. The distance between A and B is calculated to be 11.2 meters. Given that the ship model is approximately 1.5 meters long, the effective gap between the two ships is 8.2 meters. This distance ensures that the trailing ship is not influenced by the reflected waves from the tank walls.

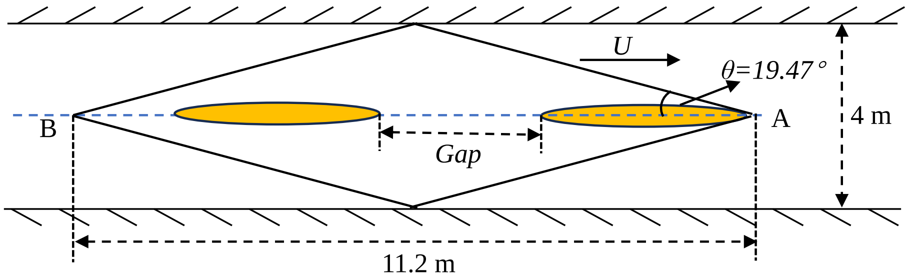

Figure 5.3: A leader-follower ship formation advancing in a towing tank.

5.3.2 Measurement uncertainties

To ensure the reliability of the experimental measurements, the measurement uncertainties are examined. These uncertainties primarily include bias uncertainties resulting from systematic inaccuracies and precision uncertainties arising from individual measurement variations (Forgach and MD, 2002; Stern, 1999).

The bias uncertainties may arise from the following factors:

(1) During the load cell calibration process, different weights are incrementally placed on the weight pan to simulate the load. However, each weight may have its own specific bias error, potentially leading to an overall discrepancy in the total weight measurement.

(2) The drift of the load cell leads to inconsistent results when weighing the same object. It can be challenging to identify as the drift affects all measurements.

(3) Both the leading ship and the trailing ship should be installed along the centerline; however, the installation process might introduce a slight angle between the two ships.

(4) Due to the limitations of the digital drive system's accuracy, the actual movement speed of the carriage may slightly differ from the set-up speed.

(5) During the data acquisition process, bias errors can be introduced by the instability of the analog-to-digital converter (ADC).

The precision uncertainties may include the following elements:

(1) The calibration factors may be influenced by the curve for each measured weight value.

(2) The distance measurement can introduce errors with each adjustment of the separation between the two vessels.

(3) The total resistance of each vessel for specific cases is obtained using the Spike software. This process relies entirely on manual operation, which may introduce measurement errors.

During load cell calibration, each data point is recorded as weight is incrementally added or removed from the calibration stand. The calibration factor is derived by determining the slope representing the relationship between the output voltages and the corresponding applied weights. Figures 5.4(a) and (c) illustrate the measured weight and voltage data by load cells A and B, respectively, along with linear fittings to these data. The calibration factors for load cells A and B are determined to be 13.98155 and 13.9496, respectively. The uncertainty associated with these factors at a 95% confidence level are 0.006656 for load cell A and 0.022304 for load cell B. Figures 5.4(b) and 3(d) show the weight calibration data, with the 95% confidence intervals for load cell A and B being 0.006976 and 0.016224, respectively. These values fall below the recommended threshold of 2 for this confidence level.

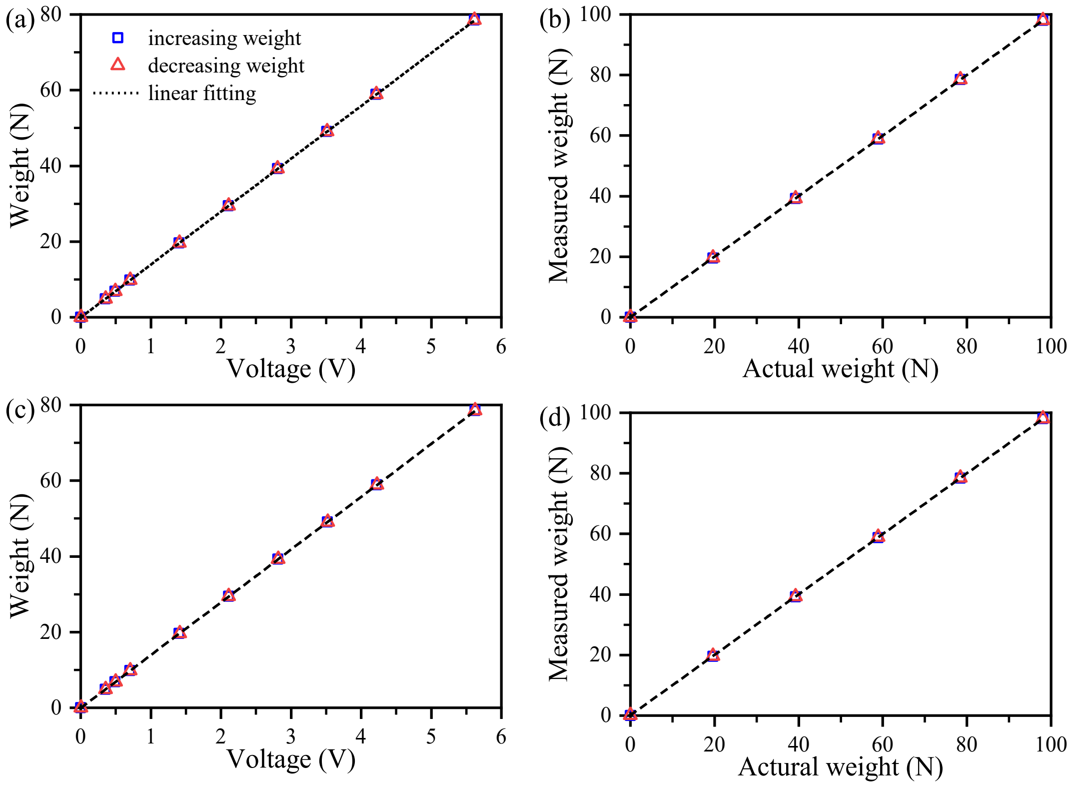

Figure 5.4: Voltmeter calibration and weight calibration. The voltmeter calibration of (a) load cell A and (b) B, respectively. The weight calibration of (c) load cell A and (d) B, respectively.

5.3.3 Models and test matrix

To simplify processing and fabrication, the ship models were designed primarily with combinations of rectangular and triangular prisms. Three distinct models were employed in the experiment, with their detailed parameters and shapes illustrated in Figure 5.5. Model A is a simple cuboid, Model B comprises a cuboid combined with a right triangular prism, and Model C integrates a cuboid with two right triangular prisms. The mid-section of these models features a length of 1 m and a width of 0.25

m, with the edge length of the orthotropic prism measuring 0.25 m. The designed draft of these models is 0.15 m, while the height of the superstructure above the waterline is 0.2 m. The total resistance of these three models, as well as Model B in reverse motion, traveling at different speeds, was measured in single model tests. These shapes are considered to analyse the effect of bow and stern shapes on the resistance of a single vessel and ship formations.

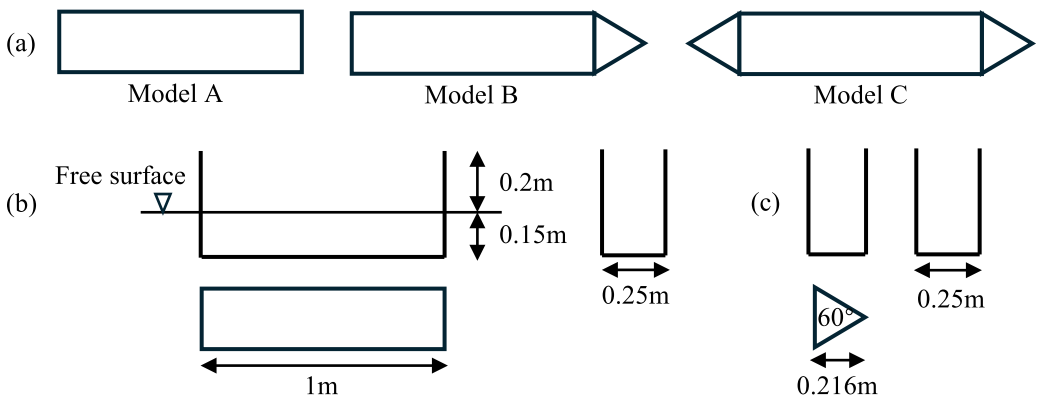

Figure 5.5: Comparison of different ship models and their three-view drawings. (a) Different ship models. Three-views drawing of (b) the mid-body and (c) the bow or the stern.

Three distinct ship formations were configured by incorporating various models, as illustrated in Figure 5.6. Formation A integrates Model A and Model B, Formation B comprises two instances of Model B, and Formation C consists of two instances of Model C. Due to the adjustment range limitations of the sliding frame, the gap between the two models in Formation A ranges from 0.1m to 2.5m. For Formation B, the gap varies from 0.1m to 2.3m, while for Formation C, it extends from 0m to 2m. Given the intensification of interference between the two models at closer separation distances, the initial adjustment interval is set to 0.05 m. As the distance between the models increases, this interval is adjusted to 0.1 m or more. The maximum testing speed is limited to avoid the impact of “green water”. In ship formation tests, the movement speeds were set at 1.036 m/s, 1.209 m/s, 1.382 m/s, 1.554 m/s, 1.727 m/s, and 1.9 m/s, which correspond to Froude numbers of 0.3, 0.35, 0.4, 0.45, 0.5, and 0.55 for Model B, respectively.

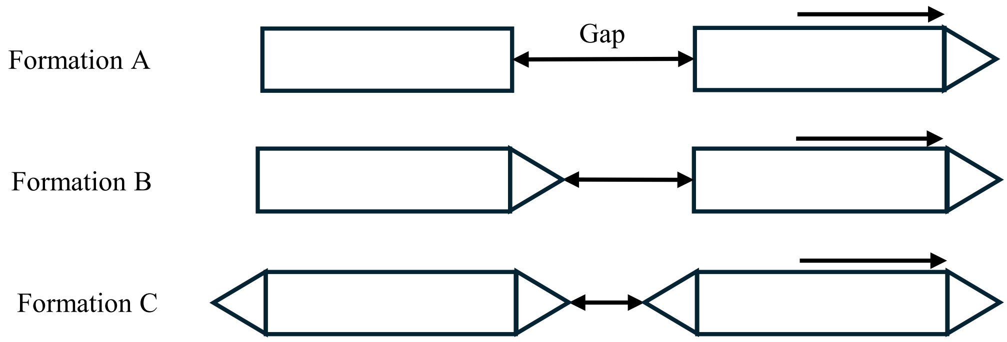

Figure 5.6: Different ship formations.

5.4 Results and discussions

5.4.1 Resistance of a single ship

Understanding the wake field of a single ship with a transom stern is beneficial for analyzing the hydrodynamic interference between ships. As shown in Figure 5.7(a), when a ship moves in calm water, two sets of right-handed coordinate systems are employed. The first one is a global reference system, designated as $O - XYZ$. In this system, the positive Z-axis points upwards and remains stationary relative to the calm water surface. The second is a local reference system, denoted as $o - xyz$, which is fixed to the center of gravity of the model. The ship moves at a speed U along the negative X-axis. The wake field of a transom stern can be segmented into three distinct regions along the flow direction: the converging wave corner region, the rooster tail region, and the divergent wave region (Hendrickson et al., 2019). Figure 5.7(b) illustrates the wake field of a ship with a transom stern moving at 1.9 m/s. The flow separation behind the transom stern leads to stern ventilation, resulting in a nearly dry stern state. A dry transom stern lead to hydrostatic resistance due to the absence of hydrostatic pressure on the transom face. This resistance is often referred to as the hydrostatic drag. A hollow is observed behind the transom stern, with ridges rising from the lower corner. These ridges angle toward the stern centerline, entraining some air and generating significant spray. As the wake spreads laterally, the divergent wave train maintains a steady V-shape. Due to air entrainment and turbulent disturbance, a "whitewater zone" with numerous bubbles forms within the surrounding flow field (Chen et al., 2024).

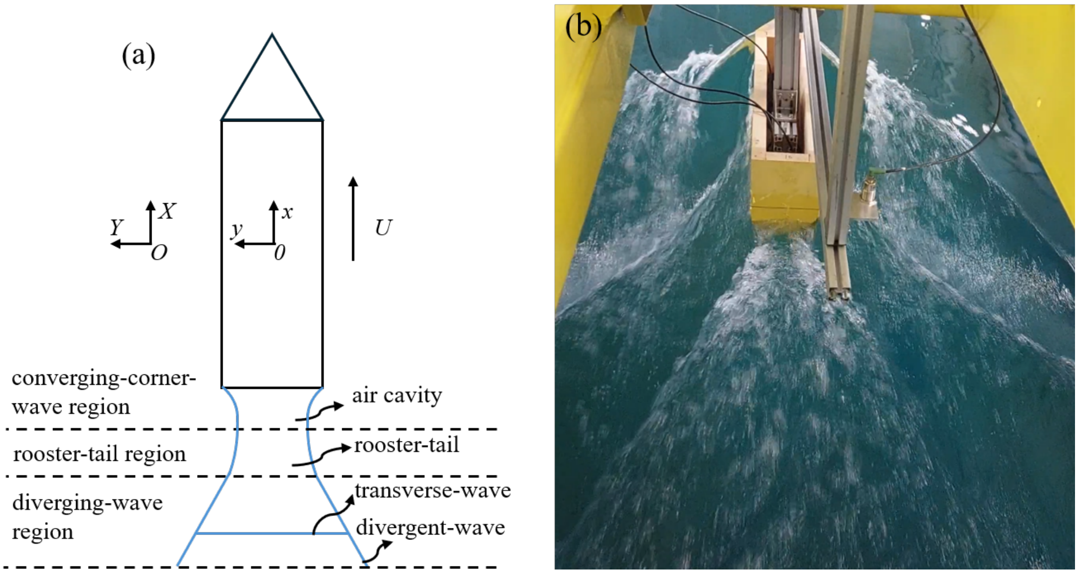

Figure 5.7: Wake field behind a ship with a transom stern. (a) Characteristics of the wake filed behind a transom stern. (b) The wake field of a ship with transom stern moving at 1.9 m/s.

Since the transom-draft Froude number was first proposed by Saunders (1957) to quantify the transom ventilation, it has become a crucial parameter in the study of transom stern issues. The transom-draft Froude number is defined as

$$F_T = \frac{U}{\sqrt{gT_d}} \tag{5.8}$$

where T_d is the transom draft and U is the movement speed.

Figure 5.8 illustrates the total resistance of various single ship models. To evaluate the uncertainty of resistance measurements, several speeds were tested two or three times for different models. The resistance measurements demonstrate good repeatability, with a measured error of 6.25%, which remains within acceptable limits. The total resistance of Model A is nearly equivalent to that of Model B when operating in reverse at all speeds. Similarly, the total resistance of Model C closely aligns with that of Model B when moving forward. Both sets of models feature an identical bow design

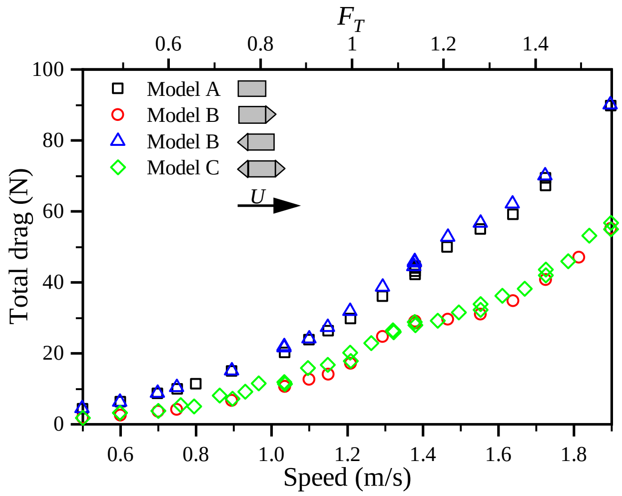

Figure 5.8: Total resistance of various individual ship models.

but differ in their stern configurations. Doctors (1999) pointed out that the formation of a hollow behind the transom creates a virtual extension of the vessel's length. This phenomenon is evident in the present experiments, where models with transom sterns, despite being shorter than those with sharp forms, demonstrate comparable hydrodynamic performance.

The total resistance of Models A and B in reverse is significantly higher than that of Models C and B moving forward. Models with a flat bow generate more frontal waves compared to those with a sharp bow, resulting in higher wave-making resistance, especially at high speeds. Due to the interference between waves generated by the bow and stern, a hump in the resistance is observed near 1.4 m/s for Models C and B moving forward. However, this effect is insignificant for Models A and B in reverse. The stagnation pressure at the forebody hull is significantly higher for models with a flat bow compared to those with a sharp bow. Consequently, the hydrostatic resistance is also greater for models with a flat bow than for those with a sharp bow. The variation caused by wave interference between the bow and stern may be negligible compared to the substantial hydrostatic pressure resistance for models with a flat bow.

Figure 5.9 illustrates the total resistance and its individual components for Model C. The frictional resistance can be calculated by

$$R_F = \frac{1}{2}\rho S U^2 C_F \tag{5.9}$$

where S is the wetted body surface and ρ is the water density. The form factor is determined using formulation 5.5, with C_T and C_F substituted by by R_T and R_F, where R_T is the measured total resistance. Based on the drag data obtained at 0.597 m/s and 0.699 m/s, a form factor of 4 is obtained. This value is much higher than that of streamlined vessels, primarily due to the insentive flow separation caused by its sharp cross-section.

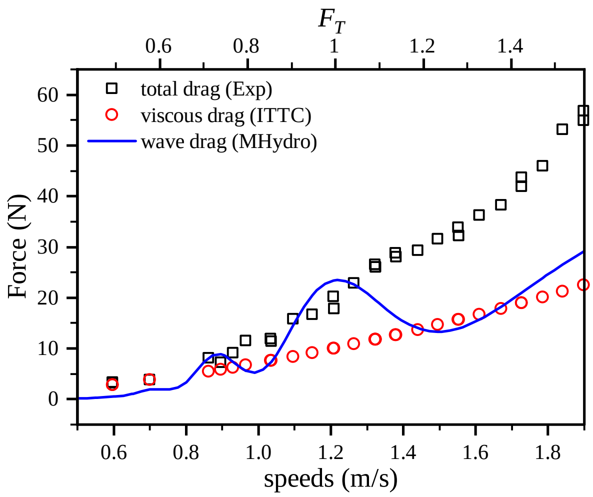

Figure 5.9: The total resistance and individual resistance components of Model C.

The in-house code MHydro is employed to predict the wave resistance of Model C. When moving speed is below 0.8 m/s, the wave drag is consistently lower than the drag due to viscosity, which includes both frictional and form drag. Afterwards, they are at the same level, and in some velocity regions, wave drag is higher than viscous drag. The wave drag is observed to exceed the total drag at approximately 1.2 m/s, which is not reasonable. The wave drag is calculated by integrating the pressure over the wet surface within the framework of linear potential flow theory. However, the impact of nonlinear waves and flow separation on the prediction of wave drag cannot be ignored in this thesis, which could lead to the discrepancy.

5.4.2 Resistance of ships with different formations

In formation tests, Formation B is used as a comparison group. When compared with Formation A, both formations feature the same leading ship, Model B. However, the trailing ship differs: Formation A uses Model A, while Formation B uses Model B. In comparison with Formation C, both formations have identical leading and trailing ships, but Formation B uses Model B for both, whereas Formation C uses Model C.

Comparison between formations A and B

Figure 5.10 illustrates the reduction in total drag for each ship in Formations A and B across various speeds. When the gap is less than 0.5 m, the C_{DR}^{T} values for both the leading and trailing ships in Formation A are generally higher than those in Formation B. Especially, the trailing ship in Formation A consistently achieves a significant total drag reduction, reaching approximately 70% at most speeds. As the gap widens from 0.1 m to 0.5 m, the C_{DR}^{T} values for the leading ship in Formation B decrease more significantly than those in Formation A. On one hand, the trailing ship with a flat bow in Formation A generates more frontal waves compared to the trailing ship with a sharp bow in Formation B. These waves can fill the cavity behind the transom stern of the leading ship, significantly decreasing the hydrostatic pressure resistance of the leading ship. On the other hand, a flat bow more effectively prevents cross-flow from concentrating at the center, thereby avoiding wave overturning and breaking. Additionally, it better utilizes the low-pressure area in the cavity region to reduce the stagnation pressure on the bow surface compared to a sharp bow.

The turning point of the C_{DR}^{T} values for the trailing ship in Formation B is observed when the gap is approximately 0.5 m. At this point, the bow of the trailing ship enters the high-pressure zone in the rooster tail region of the leading ship, which is unfavorable for drag reduction. However, this effect is insignificant for the trailing ship in Formation A, as the bow waves from the trailing ship destroy the formation of the rooster tail. When the gap exceeds 0.5 m, the C_{DR}^{T} values for the trailing ship in Formation B gradually increase, with wave interference beginning to dominate the interaction between the two ships in the diverging wave region of the leading ship. The

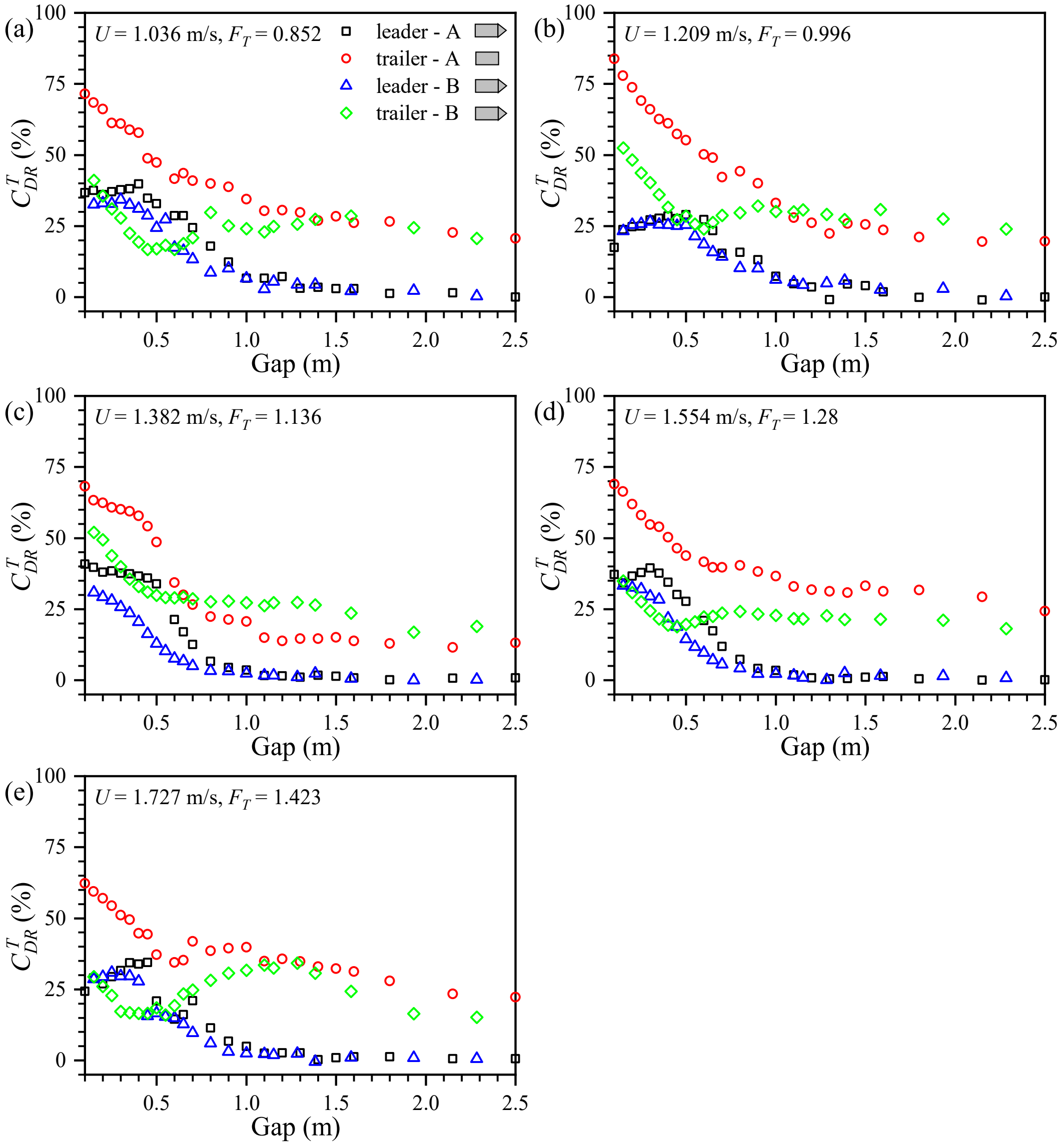

Figure 5.10: Comparison of total drag reduction between Formations A and B.

wave interference between the two ships becomes more intensive as speed increases. At higher speeds, the wave magnitude increases significantly, resulting in the C_{DR}^T values of the trailing ship following a sinusoidal pattern, as illustrated in Figure 5.10 (e).

As the gap increases further, it becomes challenging for the leading ship to receive benefits from the interference, and the C_{DR}^T values for the leading ship in both formations gradually approach zero. Simultaneously, the wave interference between the two ships weakens, and the C_{DR}^{T} values for the trailing ships in both formations converge to constant values when the gap exceeds 2m across various speeds. Within the turbulent-bubble mixed flow region, the drag reduction primarily arises from the decrease in form drag, as flow separation around the bow and behind the transom stern of the trailing ship is weakened when moving within the turbulent flow generated by the leading ship. This is analogous to the phenomenon where free-stream turbulence can shorten the separation bubble in a wind tunnel (Nakamura and Ozono, 1987). Additionally, drag reduction is also achieved through a decrease in skin friction. When the trailing ship moves within the bubble flow, the local average fluid density and relative flow velocity are both decreased compared to moving independently. The microbubbles may also enter the turbulent boundary layer near the hull surface, reducing the shear force.

Comparison between Formations B and C

Figure 5.11 illustrates the reduction in total drag for ships in Formations B and C at various speeds. When the gap is less than 0.5m, the C_{DR}^{T} values for the leading ship in Formation C are generally lower than those in Formation B. Additionally, the C_{DR}^{T} values for the leading ship in Formation C consistently decrease, while those in Formation B remain nearly constant. At most speeds, the C_{DR}^{T} values for the trailing ship in Formation C are also lower than those in Formation B. The sharp stern can prevent the formation of cavities. However, this design can induce the flow to concentrate towards the center, generating a high-pressure region. Therefore, the transom stern design is more beneficial for total drag reduction compared to the sharp stern when the gap is less than 0.5 m.

When the gap exceeds 0.5 m, the C_{DR}^{T} values for the leading ship in Formation C decrease to zero earlier than those in Formation B. Additionally, the trailing ships in Formation C enter the wave-interference-dominated region earlier than those in Formation B. This occurs because the flow evolution in the wake of the leading vessel in Formation C completes earlier due to the sharp stern. As illustrated in Figure 5.11 (e), the phase of the C_{DR}^{T} values for the trailing ship in Formation C is significantly ahead of those in Formation B.

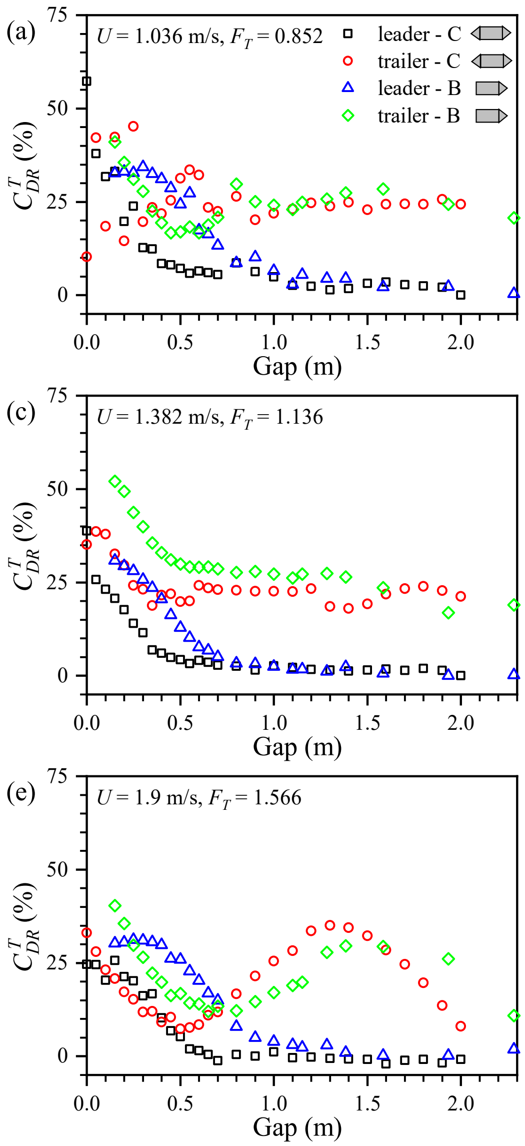

Figure 5.11: Comparison of total drag reduction between Formations B and C.

Figure 5.12 illustrates the flow fields for three typical gaps at a speed of 1.554 m/s within Formation B. At a gap of 0.15 m, both the leading and trailing ships experience reduced hydrostatic resistance. The transom ventilation of the leading ship is nearly eliminated, and the frontal waves generated by the trailing ship are minimal. When the gap increases to 0.7 m, the trailing ship enters the divergent wave zone, benefiting from wave interference between the two ships and significantly contributing to overall drag reduction. As the gap widens to 1.6 m, wave interference weakens, making the reduction in form drag and frictional drag the dominant factor in total drag reduction. These three positions represent different zones where the mechanisms contributing to total drag reduction vary. It should be noted that the lengths of these zones depend on the moving speed, so there are no absolute boundaries, especially for the length of the wave-interference-dominated zone.

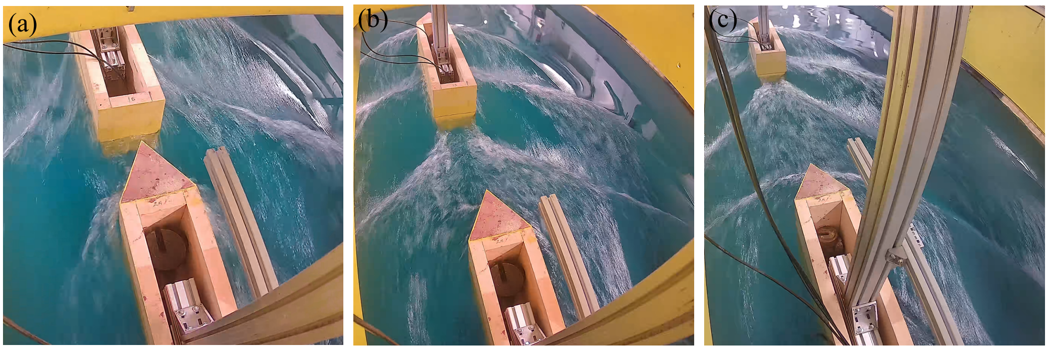

Figure 5.12: The flow fields of three different gaps in Formation B when the velocity is 1.554m/s. (a) 0.15m; (b) 0.7m; (c) 1.6m.

Comparison between total drag reduction and wave drag reduction

Figure 5.13 illustrates the reduction in total drag measured in experiments and the wave drag predicted by MHydro for both leading and trailing ships in Formation C. When the gap is less than 0.5m, the drag reduction values due to total interference for the leading ship are greater than those caused by wave interference alone. Additionally, as the gaps widen, the wave drag reduction for the leading ship decreases more rapidly compared to the total drag reduction. Within potential flow theory, flow separation due to viscosity is not considered. In the real world, energy loss due to flow separation is unavoidable, especially for bluff bodies. In the experiments, this energy loss of the leading ship is effectively supplemented by the frontal waves from the trailing ship.

The wave drag reduction values of the trailing ship oscillate around zero, while the total drag reduction values of the trailing ship oscillate around a positive value. Thus, the drag reduction due to viscous interference varies nearly linearly, with a slow decrease as the distance increases. This suggests that the trailing ship periodically benefits from wave interference while consistently gaining from viscous interference when moving in the turbulent flow of the leading ship. There is a phase difference between the total drag reduction and the wave drag reduction because the wave patterns are influenced by the turbulent disturbance, which further impacts the wave interference between the two ships. When the gap is approximately 1.2m, wave interference predominantly contributes to the total interference, while viscous interference remains relatively low. As a result, the peak value of wave drag reduction higher than that of the total drag reduction for the trailing ship.

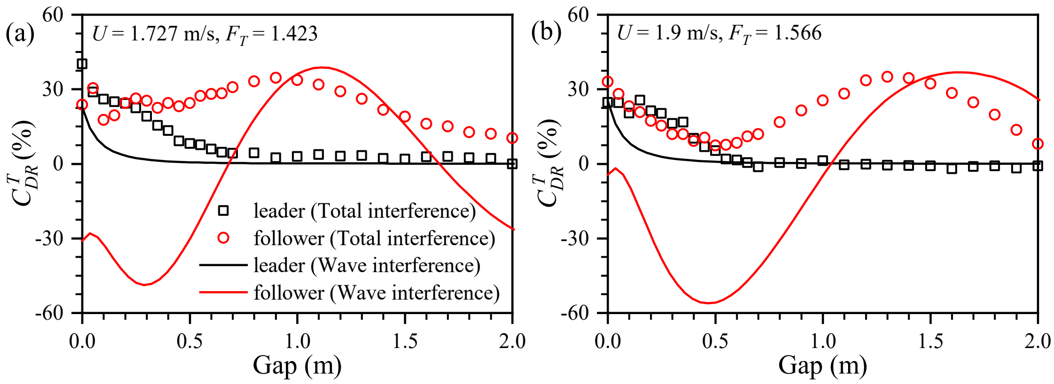

Figure 5.13: Comparison of total drag reduction between experimental and numerical results in Formation C.

5.5 Summary

The total drag reduction of the ship formation benefits not only from wave interference but also from viscous interference. To fully understand the mechanism behind this total drag reduction in ship formations, resistance experiments are conducted on both single ships with different configurations and ship formations with various combinations. In the decomposition of the total drag, the form factor method is employed for the single ships and further extended to the ship formations. The ship form significantly influences its own flow field and, consequently, the flow fields of other ships in the formation. The flow separation of the transom stern is more intense than that of the sharp stern, thus the resistance of these two stern forms is examined. Additionally, the ship bows with flat and sharp forms are also considered in the tests. By comparing the resistance results and analyzing the flow fields, the following conclusions are obtained:

(1) For single ships with the same bows, there is little difference in total resistance between the transom stern and the sharp stern. This is because the flow separation behind the transom stern induces transom ventilation and the formation of an air hollow, which effectively elongates the ship's length.

(2) The total resistance of a ship with a flat bow is significantly higher than that of a ship with a sharp bow, with the hydrostatic drag component being substantially greater for the flat bow. This is because the stagnation pressure on the surface of a flat bow is higher than that on a sharp bow, leading to increased hydrostatic drag.

(3) The turbulent flow behind the transom stern is intense, leading to wave breaking and overturning, which induces air entrainment. The whitewater in the wake is observed due to the formation of air bubbles.

(4) When two ships are in close proximity, a transom stern on the leading ship significantly aids in drag reduction for both vessels. The flow separation at the transom stern creates a low-pressure hollow. The bow waves from the trailing ship can fill this hollow, thereby reducing the hydrostatic pressure resistance of the leading ship. Simultaneously, the trailing ship benefits by releasing some of the high pressure on its bow surface, which also reduces its hydrostatic pressure resistance. For a trailing ship with a flat bow, the mutual benefit is more significant than with a sharp bow.

(5) As the gap between two ships increases, the bow waves from the trailing ship hardly influence the leading ship, thus the leading ship receives significantly less benefit. By contrast, the trailing ship enters the divergent wave zone in the wake of the leading ship, where wave interference significantly affects the total drag, especially at high speeds.

(6) As the gap between the two ships continues to widen, the wave amplitude diminishes, making wave interference negligible. The wave drag reduction values of the trailing ship converge to a nearly constant value within the turbulent-bubble mixed flow region. This drag reduction can be attributed to two factors: the flow separation weakens when the trailing ship moves in the turbulent flow, reducing form resistance; and frictional resistance decreases as the trailing ship moves through the bubble flow, which alters the turbulent boundary layer on the hull surface, further reducing the viscous shear force.

Chapter 6

Hydrodynamic Responses of Marine Trains in Waves

6.1 Introduction

Marine trains, also known as "tug and tow" configurations, are designed to enhance the efficiency and versatility of water transport. This system involves multiple ships or barges interconnected through specific mechanical connections, with the leading ship, often a tugboat, providing the propulsion for the entire assembly, as shown in Figure 6.1. This design is particularly prevalent in inland waterway transport, offering several advantages such as flexibility in cargo handling, cost-effectiveness, and the ability to navigate through narrow and shallow waterways. Moreover, marine trains have great promise for enhancing the overall logistics and operational efficiency of maritime transport systems. However, harsh marine environments pose significant challenges to the safe operation of marine trains. One major concern in the development of marine trains is the large motion response between interconnected barges. Additionally, the mechanical connections can be fragile due to the enormous wave loads. To the best of the author's knowledge, few studies have focused on this research topic. Thus, based on these concerns, some critical problems are proposed:

- What are the differences in motion response between a single ship and a marine train?

- What type of mechanical connection is most suitable for marine trains, considering the reliability of joints in wave conditions?
- How do advancing speeds impact the motion responses of marine trains?
- Do the installation position of joints and the gap between ships significantly impact the motion responses of the marine train?

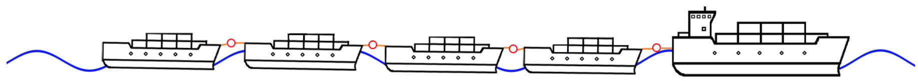

Figure 6.1: Schematic of a marine train.

In this chapter, the hydrodynamic responses of marine trains are investigated by examining various mechanical joints and marine train configurations. It begins with defining the problem and developing the mathematical model for constrained multibody systems operating with forward speed in wave conditions. It then validates the numerical method by analyzing two hinged barges and a single ship advancing in waves. Following this validation, the study compares the motion responses and shear forces at the joints of ships connected by different types of mechanical joints within a two-ship system. Finally, the chapter explores the effects of forward speed, joint positions, and gaps between tow ships on the motion responses in a marine train configuration involving four barges.

6.2 Problem definition and mathematical model

Figure 6.1 illustrates a schematic diagram of a marine train advancing through waves, comprising an engine ship and multiple barges joined by mechanical connections. The hydrodynamic modeling primarily involves analyzing diffraction and radiation interactions between ships and representing multibody dynamic constraints. The hydrodynamic problems for ships advancing in waves without constraints are solved to obtain the wave excitation forces, added mass, and damping coefficients induced by both the ship itself and other ships. Then, the dynamic coupling due to different connections is incorporated into the motion equations.

The motion equation 3.41 considers only the hydrodynamic interactions among ships without physical connections. To account for the dynamic coupling effects introduced by mechanical connections, this equation is reformulated as follows:

$$\begin{aligned}&\left[-\omega_e^2\left(M^n+\mu_{jj}^{nn}\right)+i\omega_e\lambda_{jj}^{nn}+K^n\right]\eta_j^n\\&+\sum_{n'=0,n'\neq n}^{N}\left\{\left[-\omega_e^2\mu_{jj'}^{nn'}+i\omega_e\lambda_{jj'}^{nn'}\right]\eta_j^n\right\}=F_{exj}^n+F_{coj}^n.\end{aligned} \tag{6.1}$$

Where vectors F_{exj}^n and F_{coj}^n are the vectors of force and moment due to wave-induced loads and the connection between ships, respectively. For convenience, the motion equation can be simplified as:

$$\mathbf{A}\boldsymbol{\eta}=\mathbf{F}, \tag{6.2}$$

where $\mathbf{A}$ is the stiffness matrix and $\mathbf{F}$ is the external forces on the system.

For multi-body constrained systems, the dynamic coupling due to different connections should be incorporated into the motion equations. A comprehensive discussion on the derivation of constrained dynamic systems is provided by Shabana (2009). According to Hamiltonian formalism Vinogradov and Krasil'shchik (1975), the constrained system can be expressed as

$$\Pi=\frac{1}{2}\boldsymbol{\eta}^T\mathbf{A}\boldsymbol{\eta}-\boldsymbol{\eta}^T\mathbf{F}. \tag{6.3}$$

Considering there are rigid constrains between some of the degrees of freedom, the constraint equation is given by

$$\mathbf{D}\boldsymbol{\eta}=0. \tag{6.4}$$

By means of the method of Lagrange multipliers method, the Eq. 6.3 can be modified as

$$\Pi = \frac{1}{2}\boldsymbol{\eta}^T\mathbf{A}\boldsymbol{\eta} - \boldsymbol{\eta}^T\mathbf{F} + \boldsymbol{\gamma}^T\mathbf{D}\boldsymbol{\eta}. \tag{6.5}$$

The sizes of $\{\mathbf{F}\}$ and $\{\boldsymbol{\eta}\}$ are $(6n \times 1)$; $[\mathbf{A}]$ is $(6n \times 6n)$; $[\mathbf{D}]$ is $(m \times 6n)$; $\{\boldsymbol{\gamma}\}$ is $(m \times 1)$, where n represents the number of ships, and m represents the total number of constraints at all joints. By simultaneously taking the variations of both sides of Equation 6.5, we obtain:

$$\begin{bmatrix} [A]_{6n\times 6n} & [D]^T_{6n\times m} \\ [D]_{m\times 6n} & [0]_{m\times m} \end{bmatrix} \begin{Bmatrix} \{\eta\}_{6n\times 1} \\ \{\gamma\}_{m\times 1} \end{Bmatrix} = \begin{Bmatrix} \{F\}_{6n\times 1} \\ \{0\}_{m\times 1} \end{Bmatrix} \tag{6.6}$$

where Lagrange multipliers $\{\boldsymbol{\gamma}\}$ represents the generalized force associated with the constraints in a system.

For example, when the two barges are hinged (only allowing rotation around the y-axis), the displacement continuity conditions should be:

$$\xi_{n_1} = \xi_{n'_1},\ \xi_{n_2} = \xi_{n'_2},\ \xi_{n_3} = \xi_{n'_3},\ \xi_{n_4} = \xi_{n'_4},\ \xi_{n_6} = \xi_{n'_6}, \tag{6.7}$$

where ξ_n and $\xi_{n'}$ are the displacements of barge n and n' at the joint point, respectively.

$$\begin{aligned} \xi_{n_1} &= \eta_{n_1} + Z_n \times \eta_{n_5} - Y_n \times \eta_{n_6}, \\ \xi_{n'_1} &= \eta_{n'_1} + Z_{n'} \times \eta_{n'_5} - Y_{n'} \times \eta_{n'_6} \end{aligned} \tag{6.8}$$

where (X_n, Y_n, Z_n) and $(X_{n'}, Y_{n'}, Z_{n'})$ are the coordinates of the hinge joint in the two body-fixed coordinate systems, respectively. The matrix $[D]$ can be expressed as:

$$[D]_{5\times 12} = \begin{bmatrix} 1 & 0 & 0 & 0 & Z_n & -Y_n & -1 & 0 & 0 & 0 & -Z_{n'} & Y_{n'} \\ 0 & 1 & 0 & -Z_n & 0 & X_n & 0 & -1 & 0 & Z_{n'} & 0 & -X_{n'} \\ 0 & 0 & 1 & Y_n & -X_n & 0 & 0 & 0 & -1 & -Y_{n'} & X_{n'} & 0 \\ 0 & 0 & 0 & 1 & 0 & 0 & 0 & 0 & -1 & 0 & 0 & 0 \\ 0 & 0 & 0 & 0 & 0 & 1 & 0 & 0 & 0 & 0 & 0 & -1 \end{bmatrix} \tag{6.9}$$

Table 6.1 illustrates various types of mechanical connections and their corresponding constrained and released degrees of freedom.

Table 6.1: Different connection styles

Connections	**Surge**	**Sway**	**Heave**	**Roll**	**Pitch**	**Yaw**
Free	✓	✓	✓	✓	✓	✓
Hinged	–	–	–	–	✓	–
Rigid	–	–	–	–	–	–
Sliding-hinged	–	✓	–	–	✓	✓

where "–" and "✓" denote constrained and released states, respectively.

6.3 Numerical validations

6.3.1 Two interconnected barges in head sea

Newman (1994) employed the mode expansion technique, and Sun et al. (2011) utilized the Lagrange multipliers method to analyze the wave-induced motion and loads of two interconnected barges. This scenario is used to validate present code, with the relevant parameters provided in Table 6.2.

Table 6.2: Main dimensions of interconnected barges

Parameter	**Value**
Length, L (m)	40
Breadth, B (m)	10
Draught, T (m)	5
Gap between barges (m)	10
Water depth, h (m)	$+\infty$

Figure 6.2 illustrates the vertical and rotational motions at the hinge when two barges are connected in linear regular waves, with no forward speed (i.e., the barges are stationary). The results from Mhydro generally align well with those of Newman (1994) and Sun et al. (2011), though the magnitude is slightly smaller, likely due to the mesh scheme employed. A notable difference between the mode expansion and Lagrange multipliers methods is observed: the Lagrange multipliers method shows a

small peak at $\lambda/L = 1.125$, corresponding to the combined length of one barge and half the gap, whereas no such peak appears with the mode expansion method. Similarly, the second peak occurs at $\lambda/L = 1.75$, corresponding to the combined length of one and a half barges plus one gap. Resonance occurs at these two characteristic lengths. The phase angles between heave and pitch are identical, as these two motions are coupled.

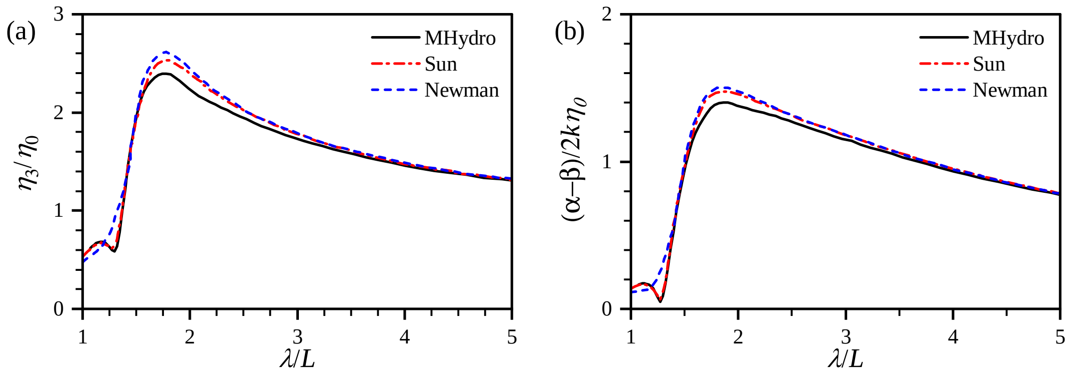

Figure 6.2: Validation of the motion of two barges in head sea. (a) Vertical motion at the hinge; (b) Rotation of the hinge.

Figure 6.3 (a) illustrates the heave motion of two barges under rigid connection, with the results once again indicating a satisfactory agreement. The motion response for the rigid connection is markedly different from that of the hinged connection, with the heave motion being significantly smaller in the rigid configuration. Additionally, the characteristic wavelengths at $\lambda/L = 1.5$ and $\lambda/L = 2.5$ correspond to the peak and trough of the response, respectively. When the two barges are connected by a rigid connection, they can be treated as a single, longer barge. At $\lambda/L = 1.5$, this longer barge spans approximately 1.5λ, which can easily induce significant heave motion. In contrast, at $\lambda/L = 2.5$, the barge spans nearly 1λ, which is favourable for the stability of the heave motion.

Figure 6.3 (b) shows the vertical shear force for both the hinged and rigid connections, which are identical. The vertical forces at the connection between the barges consist of wave excitation forces, inertia forces, and hydrodynamic radiation forces. The wave forces are the same for both connections. The other forces can be divided into symmetric and anti-symmetric modes, with only the anti-symmetric modes influencing the vertical force. However, the vertical force remains unchanged regardless of whether the connection is rigid or hinged.

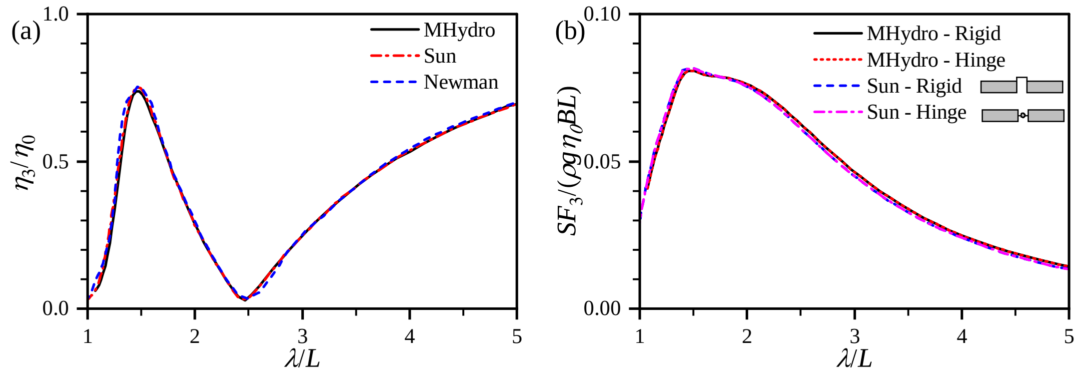

Figure 6.3: Heave motion and vertical shear force. (a) Heave response amplitude operator of rigid connection; (b) Vertical shear force at the joints.

6.3.2 Single ship moving in head sea

Figure 6.4 illustrates the motion responses of a single Wigley model in waves. The numerical results from MHydro closely match the experimental data reported by Journee (1992). At $F_\mathrm{r} = 0.2$, the heave and pitch motions are generally higher than those at zero speed. Motion peaks in heave and pitch are observed at λ/L values of 1 and 1.2, corresponding to the resonant frequency, which poses a risk to safe operation and should be avoided.

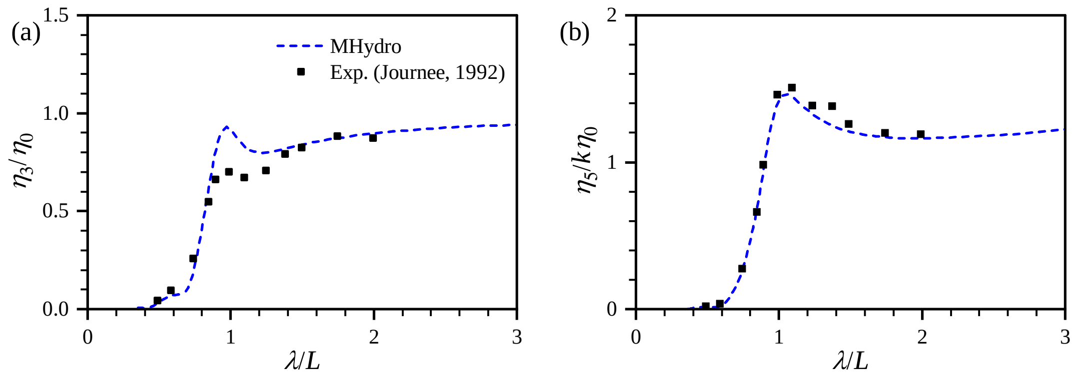

Figure 6.4: Response amplitude operators at $F_\mathrm{r} = 0.2$ in comparison with laboratory measurements of Journee (1992). (a) Heave; (b) Pitch.

6.4 Two ships with different connections in waves

6.4.1 Free connection

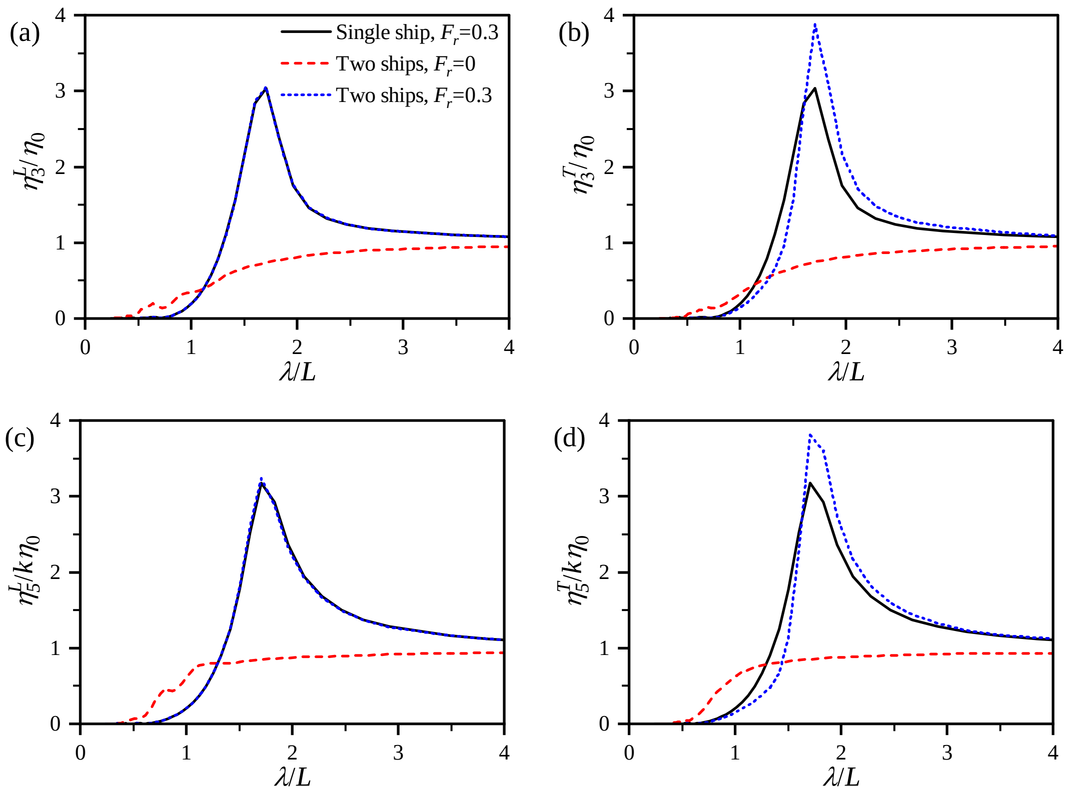

Figure 6.5: RAOs for free connection between two ships with different speeds in head sea. Heave: (a) Leading ship; (b) Trailing ship; Pitch: (c) Leading ship; (d) Trailing ship. Here, L represents the leading ship and T represents the trailing ship.

The "free connection" in this case means there is no physical connection between the two ships, allowing for relative motion in all six degrees of freedom. The Brard number τ is commonly used to compare the relationship between the ship's speed and the wave propagation speed it generates. Here, the Brard number is defined as

$$\tau = \frac{U\omega_e}{g}. \tag{6.10}$$

Figure 6.5 illustrates the heave and pitch response amplitude operators (RAOs) for both a single ship and two ships advancing with or without forward speed in head seas, with a gap of $0.1L$ between the ships. The RAOs of the single ship are identical to those of the leading ship in a formation at $F_r = 0.3$, as the trailing ship has minimal influence on the wave field of the leading ship at this speed. At $\lambda/L = 0.5$, the Brard number is equal to 2.16, while the Brard number is 0.48 at $\lambda/L = 4$. When the Brard number is greater than 0.25, the forward propagation velocity of the waves generated by the trailing ship is lower than the ship's advancing speed. This is further supported by Figure 6.6 and Figure 6.7, which show that the added mass and potential damping of the leading ship induced by the motion of the trailing ship are nearly zero. However, since the trailing ship is in the wake of the leading ship, its RAOs are significantly influenced by the leading ship. Notably, the peaks for the heave and pitch motions of the trailing ship are significantly higher than those of the leading ship when resonance occurs at $\lambda/L = 1.7$, due to wave superposition.

In addition, the RAOs of the leading and trailing ships are nearly identical when the forward speed is zero, except when the λ/L ratio is less than 1, as shown in Figure 6.5. This similarity can be explained by examining both the hydrodynamic coefficients and the wave excitation forces. As illustrated in Figures 6.6 (a) and (c) and 6.7 (a) and (c), the hydrodynamic coefficients for both ships at zero speed are identical for heave-induced heave and pitch-induced pitch added mass and potential damping. Conversely, in Figures 6.6 (b) and (d) and 6.7 (b) and (d), the coefficients for self-induced pitch-heave and heave-pitch added mass and potential damping are nearly zero. However, when these coefficients are induced by the other ship, they are equal in magnitude but opposite in sign. Therefore, the hydrodynamic coefficients do not account for the observed differences. Instead, these discrepancies primarily arise from variations in the wave excitation forces acting on the two ships. As shown in Figure 6.8, the wave excitation force on the leading ship exhibits oscillations when the λ/L ratio is less than 1, corresponding to the oscillations observed in its heave and pitch motions at these ratios. Although the wave excitation forces and moments are higher for the leading ship compared to the trailing ship when the λ/L ratio exceeds 3, there is no notable difference in the motion responses of the two ships. Both ships exhibit similar RAOs

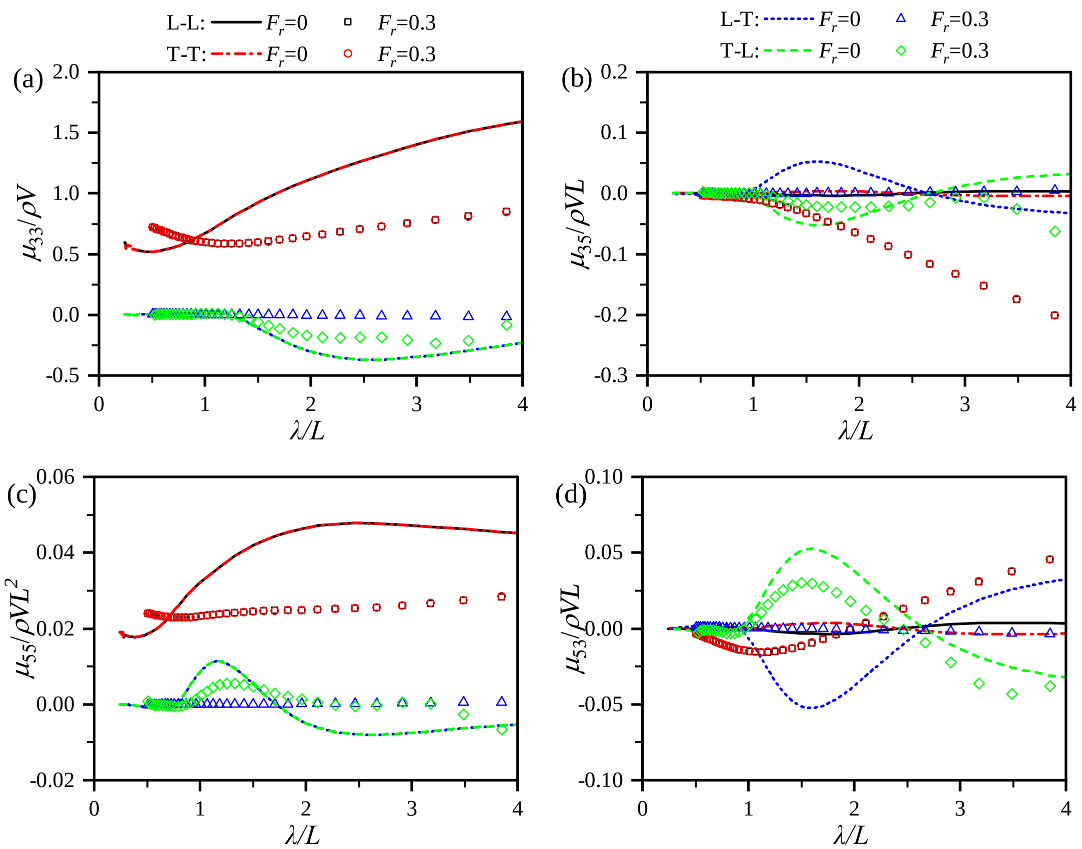

Figure 6.6: Added mass of two ships in head sea. (a) Heave added mass induced by heave motion; (b) Heave added mass induced by pitch motion; (c) Pitch added mass induced by pitch motion; (d) Pitch added mass induced by heave motion. Here, L-L indicates the effect of the leading ship on itself, T-T indicates the effect of the trailing ship on itself, L-T indicates the effect of trailing vessels on leading vessels, and T-L indicates the effect of the leading ship on the trailing ship.

close to 1, as they move in sync with the incident waves.

Furthermore, the RAOs of the two ships at zero speed are significantly different from those of the two ships at $F_r = 0.3$, as illustrated in Figure 6.5. When the λ/L ratio is less than 1, the RAOs at zero speed are higher than those at $F_r = 0.3$. Additionally, there is no resonance observed for the ships when they are at zero speed. The wave excitation forces and moments between the ships at zero speed and those at $F_r = 0.3$ do not show significant differences, as shown in Figure 6.8. Therefore, the observed differences in RAOs are mainly due to variations in hydrodynamic coefficients caused by radiation waves.

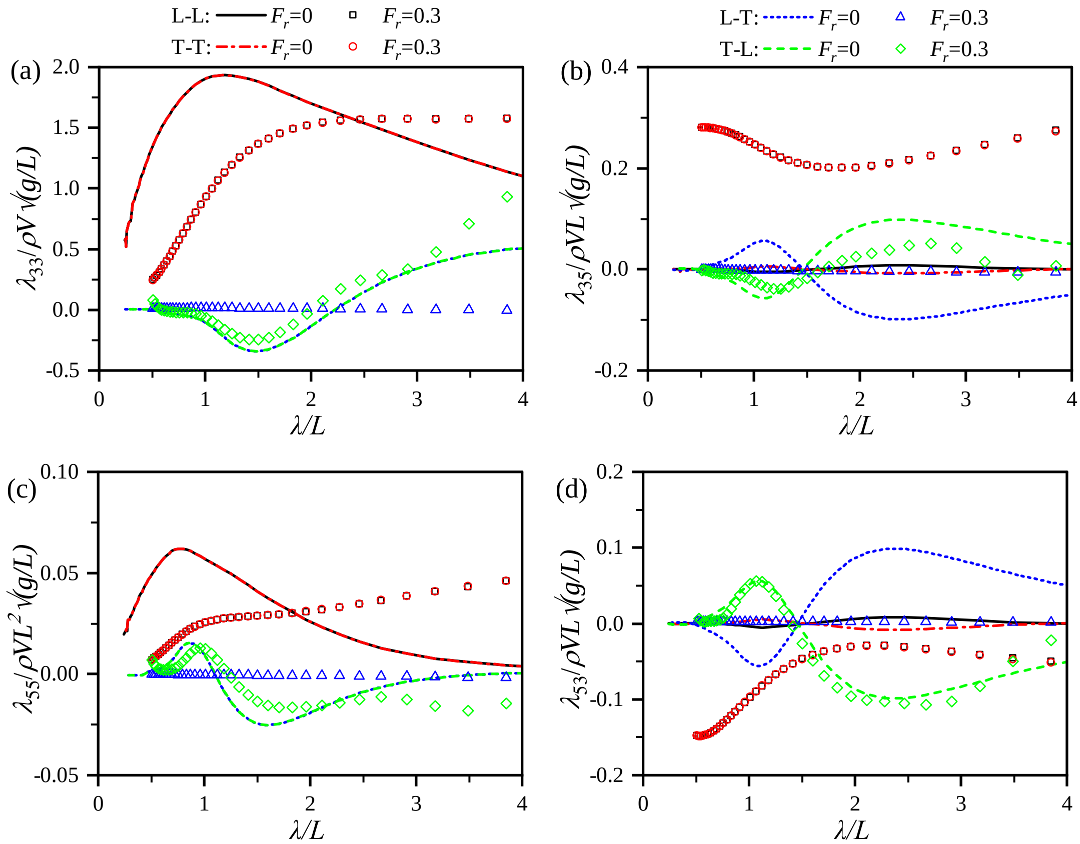

Figure 6.7: Potential damping of two ships in head sea. (a) Heave damping induced by heave motion; (b) Heave damping induced by pitch motion; (c) Pitch damping induced by pitch motion; (d) Pitch damping induced by heave motion.

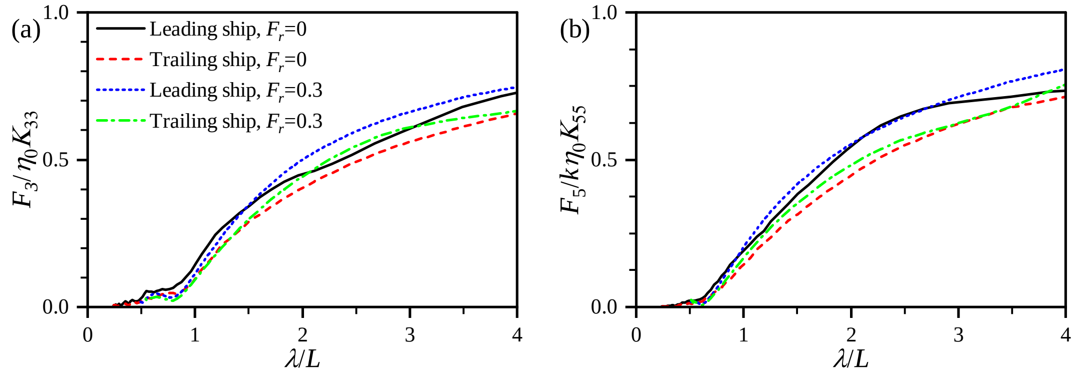

Figure 6.8: Wave excitation forces of two ships in head sea. (a) Heave force; (b) Pitch moment.

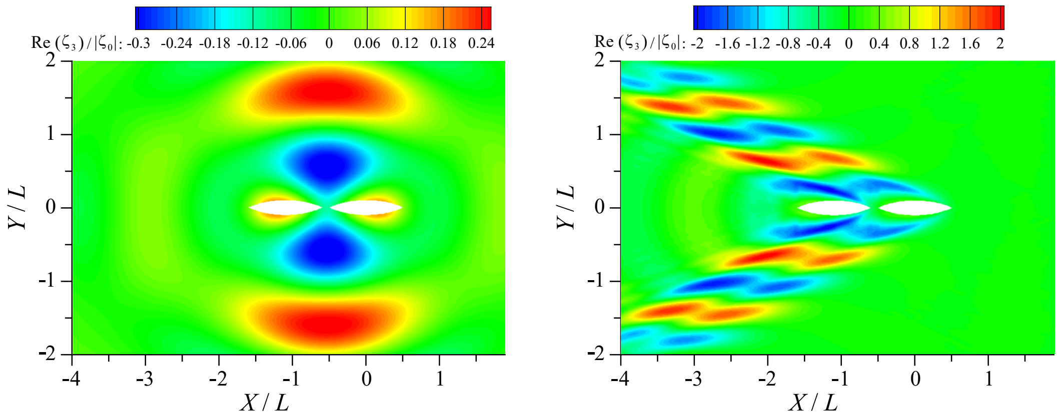

Figure 6.9: Real part of radiation wave pattern for unit heave motion at $\lambda/L = 1.83$. (a) $F_r = 0$; (b) $F_r = 0.3$.

Figure 6.9 illustrates the real part of radiated wave patterns generated by the unit heave motion of two ships advancing at different forward speeds in a head sea, with $\lambda/L = 1.83$. The wave patterns for $F_r = 0$ exhibit good symmetry, indicating that the added mass or potential damping in heave, induced by the heave motion of the other ship, is identical for both vessels. This observation aligns with the results shown in Figures 6.6(a) and 6.7(a). Additionally, at $F_r = 0.3$, the waves are convected downstream in a distinct V-shape distribution. Similarly, in the diffraction fields, the waves are also convected downstream, with the effect being significantly more pronounced at $F_r = 0.3$ compared to $F_r = 0$, as shown in Figure 6.10.

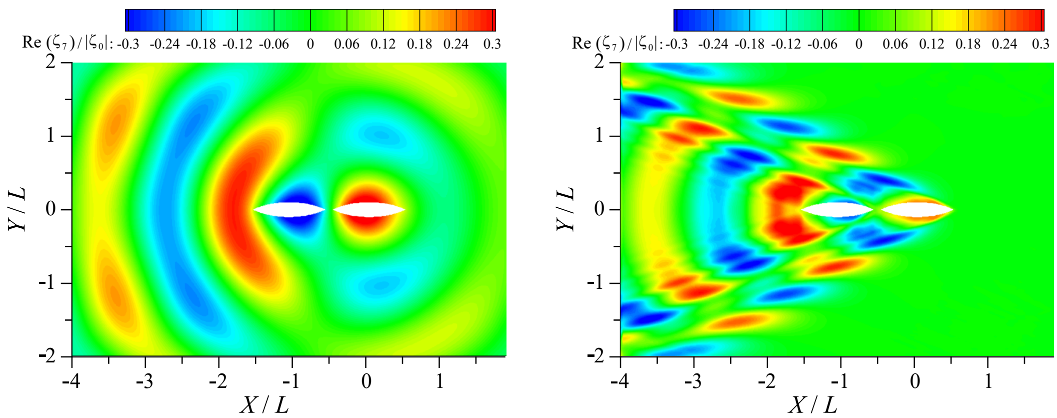

Figure 6.10: Real part of diffraction wave pattern at $\lambda/L = 1.83$. (a) $F_r = 0$; (b) $F_r = 0.3$.

6.4.2 Rigid and hinged connection

A rigid connection fully constrains all six degrees of freedom between two ships, causing them to behave as a single, rigid body. A hinged connection allows relative pitch motion between the ships, while the other five degrees of freedom remain continuous at the hinge point. Figure 6.11 illustrates the RAOs for different connection types when the ships are advancing at $F_r = 0.3$ in head sea, with a gap of $0.1L$ between the ships. The heave and pitch motions of the two ships with a rigid connection are significantly smaller compared to those with hinged and free connections. For the hinged connection, the heave and pitch motions of the leading ship are nearly the same as those with the free connection. However, the heave and pitch motions of the trailing ship with the hinged connection are notably smaller compared to those with the free connection. This suggests that both rigid and hinged connections can effectively restrain the motions of the trailing ship. Additionally, resonance in the heave motion is observed around $\lambda/L = 1.7$ for all three connection types for the leading ship, although the magnitude of the resonance differs among them. This indicates that wave loading governs the overall motion pattern of the vessels, while connection constraints influence the magnitude of the motion response.

Figure 6.12 illustrates the vertical shear forces at the joints for both rigid and hinged connections at zero speed and $F_r = 0.3$. As observed in hinged barges in waves, the vertical shear forces for both connection types are identical when the speed is zero. The peaks of the vertical shear forces for both connection types at $F_r = 0.3$ are higher than those observed at zero speed, because the wave excitation forces at $F_r = 0.3$ are generally higher than at zero speed. For the rigid connection at $F_r = 0.3$, a single peak in vertical shear force is observed, whereas the hinged connection shows two distinct peaks. The shared peak at $\lambda/L = 1.3$ for both connections is attributed to the phase difference in motion between the two ships in waves. The second peak, observed in the hinged connection at $\lambda/L = 1.7$, can be explained by the resonance in the motion response, as demonstrated in Figure 6.11. For this peak, the magnitude of motion is the dominant factor. It is important to note that the peaks of the vertical shear force reach up to half the weight of the ship itself, which could easily lead to damage of the

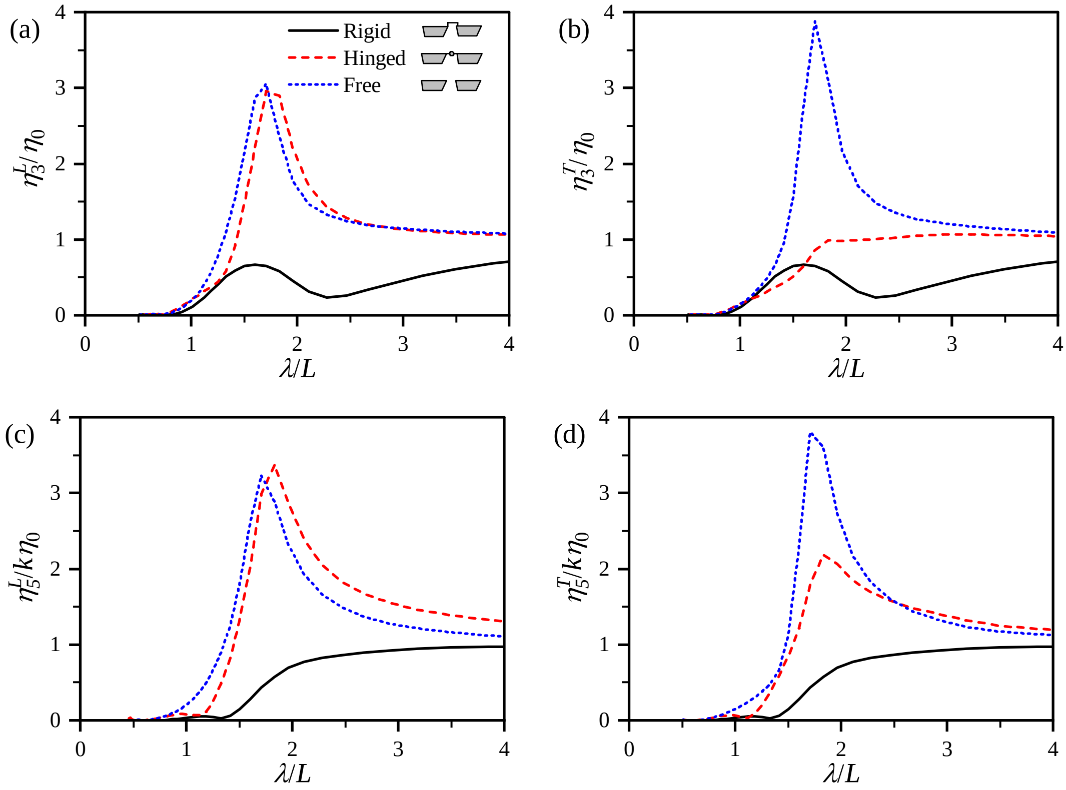

Figure 6.11: RAOs for different connections between two ships advancing at $F_r = 0.3$ in head sea. Heave: (a) leading ship; (b) trailing ship. Pitch: (c) leading ship; (d) trailing ship.

mechanical connections, posing significant risks to their overall integrity.

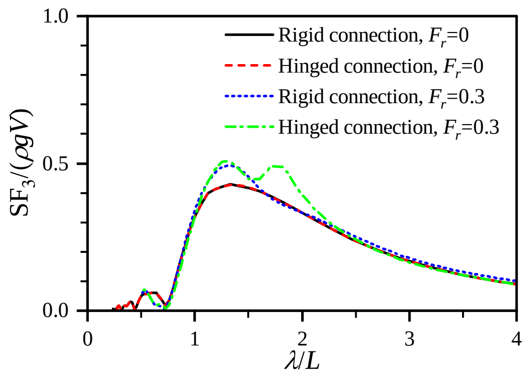

Figure 6.12: Vertical shear force at the joints for rigid and hinged connections.

6.4.3 Sliding-hinged connection

Given the significant shear forces at both rigid and hinged connections, it is crucial to mitigate these forces to reduce the risk of damage to the joints and ensure operational safety. To address this, a combined sliding-hinged connection is adopted. This design releases the heave, pitch, and yaw motions, enabling relative movement along these axes, while constraining the surge, sway, and roll motions at the joint, ensuring their continuity. In this thesis, since the turning operations are not investigated, the effect of constraining or releasing yaw motion is not discussed. Figure 6.13 illustrates the RAOs for different connections between two ships advancing at $F_r = 0.3$ in head sea, with a gap of $0.1L$ between them. The heave and pitch motions of ships with a sliding-hinged connection are identical to those observed with a free connection. This is because, in head sea conditions, the ship motions of surge, heave, and pitch are coupled, with no interaction with the sway, roll, and yaw motions. Since the heave and pitch constraints are released in the sliding-hinged connection, this setup is effectively equivalent to a free connection in terms of the constraint relationship.

Figure 6.14 illustrates the RAOs for different connections between two ships advancing at $F_r = 0.3$ in oblique sea conditions. Notably, the heave motions of both ships with a sliding-hinged connection are identical to those observed with a free connection. However, the roll motions of both ships with a sliding-hinged connection differ from those observed with a free connection, as the sliding-hinged connection does not release the roll constraints between the two ships. The roll motions of both ships with free connections are significantly higher in magnitude than those with the sliding-hinged connection, despite all configurations exhibiting resonance at the same wavelength. Additionally, for the sliding-hinged configuration, the roll motion of the leading and trailing ships is nearly identical, suggesting that the influence of the leading ship on the wave field of the trailing ship is minimal at this gap. A similar behavior is observed in the case of free connections.

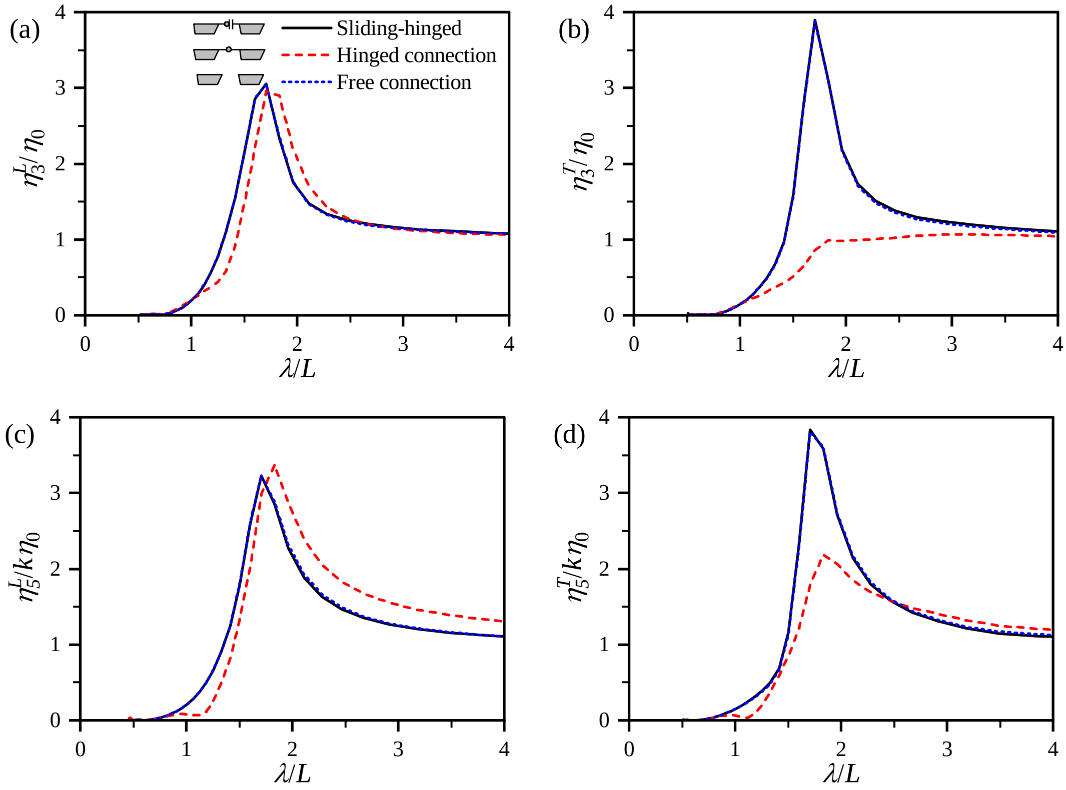

Figure 6.13: RAOs for different connections between two ships advancing at $F_r = 0.3$ in head sea. Heave: (a) leading ship; (b) trailing ship. Pitch: (c) leading ship; (d) trailing ship.

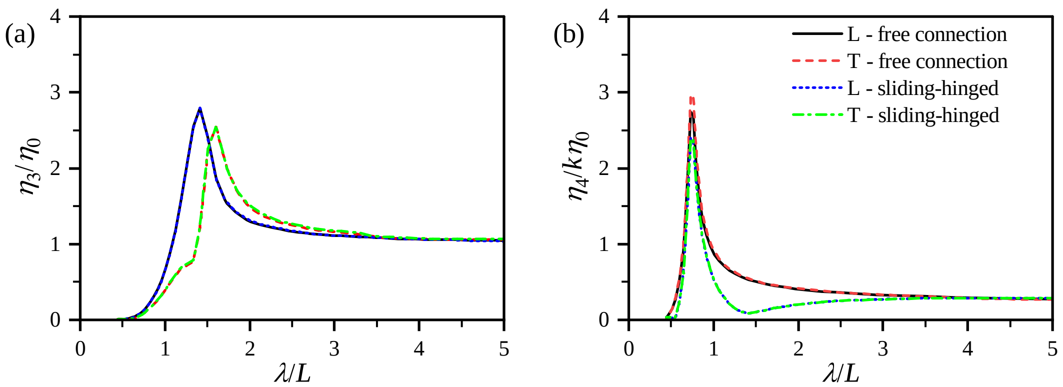

Figure 6.14: RAOs for different connections at $F_r = 0.3$ in oblique sea, with a gap of $0.1L$ between two ships. (a) Heave; (b) Roll.

6.5 A marine train with four carriages advancing in head sea

A marine train, consisting of an engine ship and four barges connected by sliding-hinged joints, is analyzed in a head sea scenario. The RAOs exhibit no significant difference between the free connection and sliding-hinged connection configurations. The sliding-hinged connections, however, provide a critical advantage: they enable the engine ship to power the entire marine train, whereas a free connection system would necessitate each unit having its own power source. Furthermore, the sliding-hinged joints are beneficial in minimizing vertical shear forces, unlike rigid or fully hinged connections.

6.5.1 Effect of advancing speeds

Figure 6.15 illustrates the RAOs for various advancing speeds with a gap of $0.1L$. The results demonstrate a notable increase in RAOs as the advancing speed rises. Additionally, the resonance frequency progressively shifts towards longer wavelengths with increasing speed. This shift can be attributed to the Doppler effect: as the ship advances, the incident waves at the bow are compressed and effectively slow down, resulting in shorter wavelengths. Consequently, the resonance condition is met at longer wavelengths as speed increases. Furthermore, as the ship moves faster, more energy accumulates around the hull, leading to higher motion responses at resonance.

It is also observed that the RAOs of the ships at the same advancing speed exhibit distinct patterns. When the wavelength is shorter than the resonance wavelength, the RAOs gradually decrease from the leading ship (or engine) to the last barge. Conversely, when the wavelength is longer than the resonance wavelength, the RAOs gradually increase from the leading ship to the last barge. This behavior can be attributed to the phase superposition of waves generated by the different ships. In the case of shorter wavelengths, destructive interference occurs, leading to a reduction in RAOs along the convoy. On the other hand, for wavelengths longer than the resonance wavelength, constructive interference dominates, resulting in an increase in RAOs from the leading

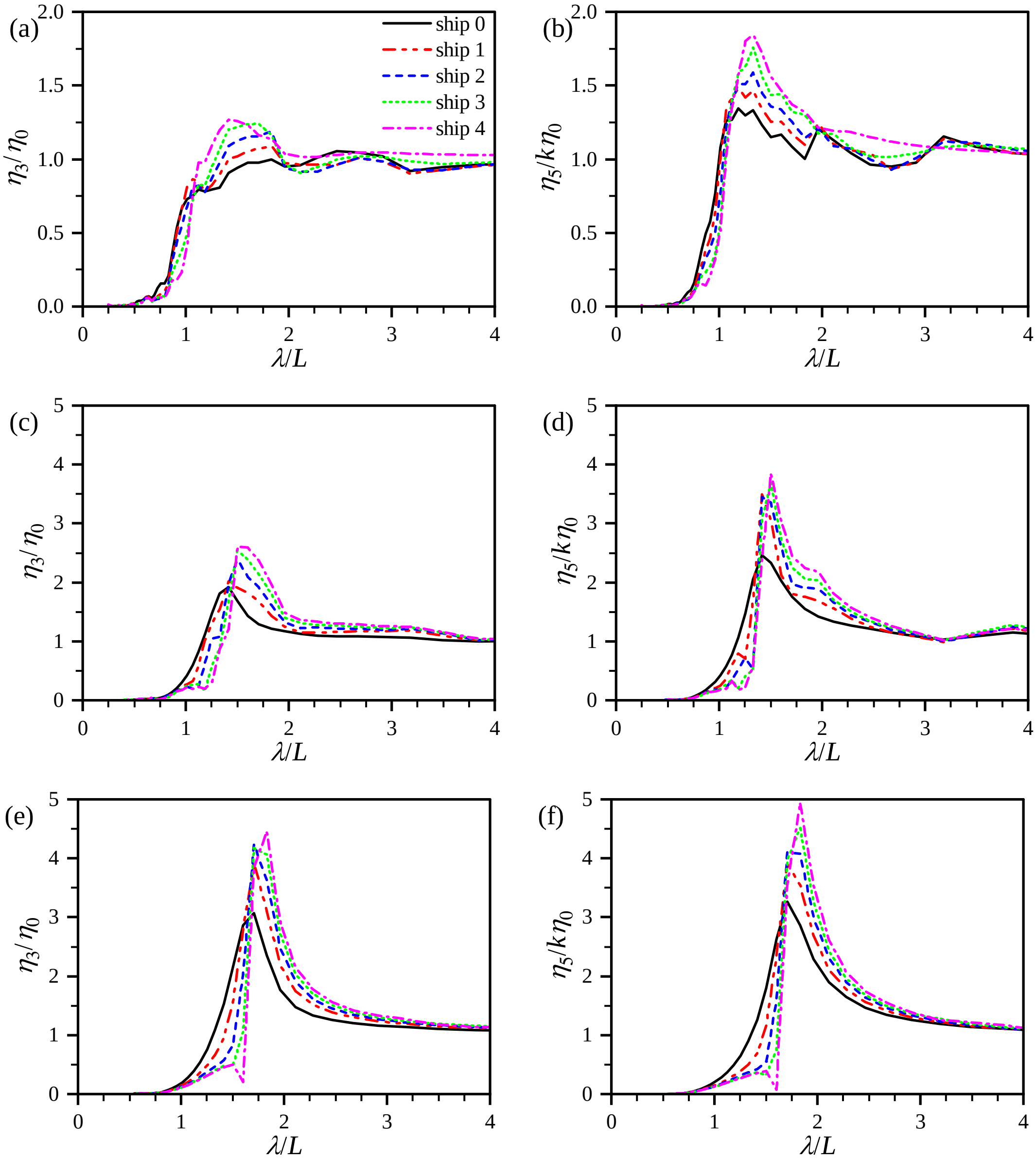

Figure 6.15: RAOs at different speeds with a gap of $0.1L$. Heave: (a) $F_r = 0.1$; (c) $F_r = 0.2$; (e) $F_r = 0.3$. Pitch: (b) $F_r = 0.1$; (d) $F_r = 0.2$; (f) $F_r = 0.3$.

ship to the last barge.

Figure 6.16 illustrates the wave fields for different incident wavelengths at $F_r = 0.3$. The total wave magnitude around each ship effectively explains the RAOs observed for the corresponding vessel. For instance, at $\lambda/L = 1.6$, the wave amplitude around the leading ship is significantly higher than that around the trailing ships, resulting in

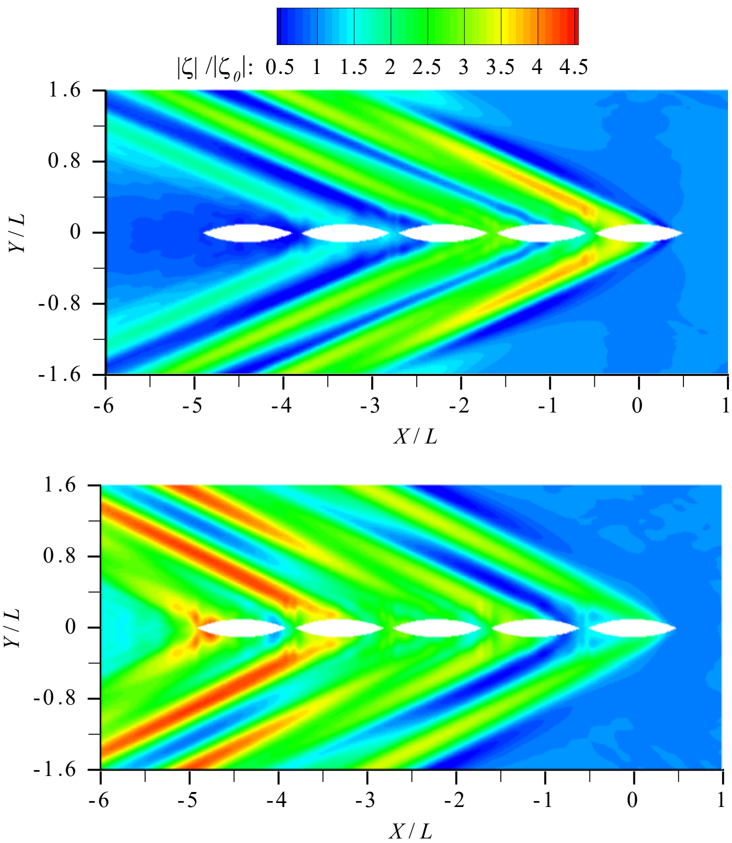

Figure 6.16: Wave magnitude for different wavelengths at $F_r = 0.3$. (a) $\lambda/L = 1.6$; (b) $\lambda/L = 1.83$.

greater heave and pitch motions for the leading ship compared to the trailing vessels. At $\lambda/L = 1.83$, resonance occurs, progressively amplifying the motion responses along the convoy, with the last trailing ship experiencing the largest and most unexpected motion responses. Beyond the resonance wavelength, the wave amplitude quickly decreases as the incident wavelength increases. Therefore, to ensure operational safety, it is recommended to avoid resonance wavelengths at different speeds.

6.5.2 Effect of installation position of joints

The installation positions of the joints are considered at three locations, all on the waterplane in a hydrostatic state along the centerline in the moving direction: one positioned midway between the two ships and the others at the bow and stern of the

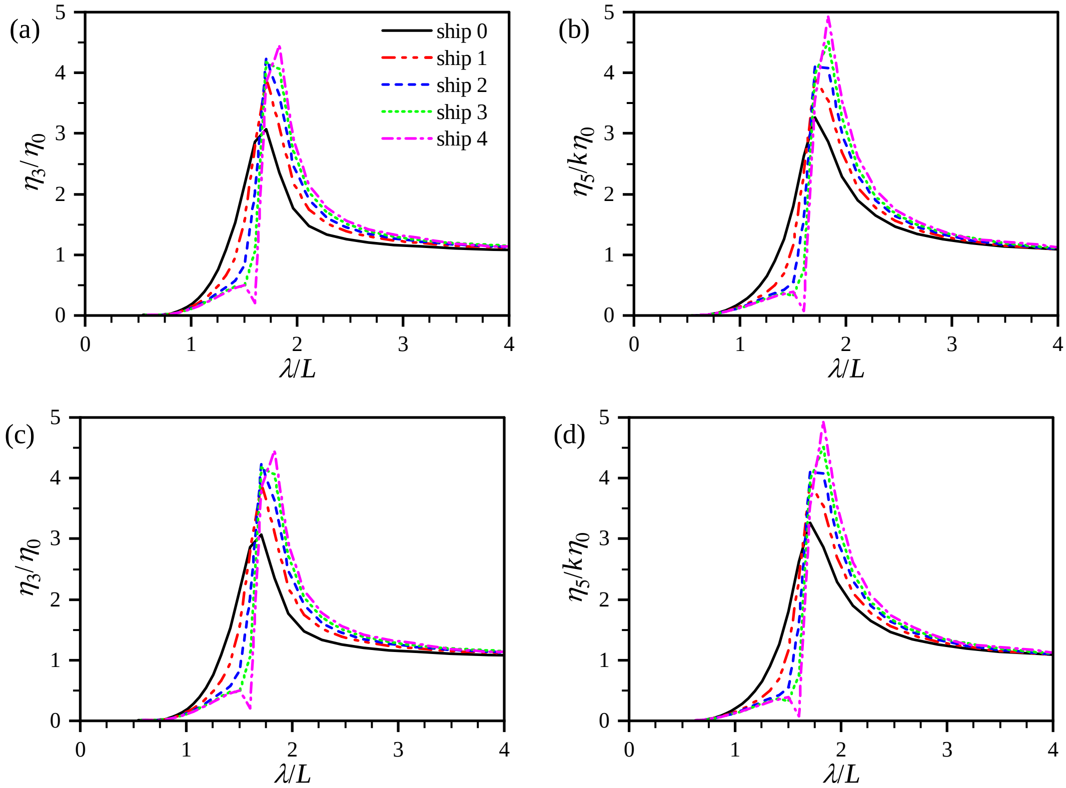

Figure 6.17: RAOs for different positions of joints with a gap of $0.1L$ at $F_r = 0.3$. Heave: (a) midway; (c) stern. Pitch: (b) midway; (d) stern.

ships. Due to position symmetry, the stern is chosen for the numerical calculation. Figure 6.17 illustrates the RAOs for these different joint positions between the ships. Notably, there is no significant difference in the heave and pitch motions, regardless of whether the joint is positioned midway or at the stern. This is because the sliding-hinged connection allows for the release of heave and pitch motions, with only the surge motion constrained in head seas, resulting in the heave and pitch motions being uncoupled in the constraint matrix. Additionally, the surge motion is insensitive to changes in the position of the joints along the x-axis.

6.5.3 Effect of gap between two ships

The spacing between two ships plays a crucial role in ensuring safe operations in waves, particularly in preventing collisions. The gap between two ships may influence

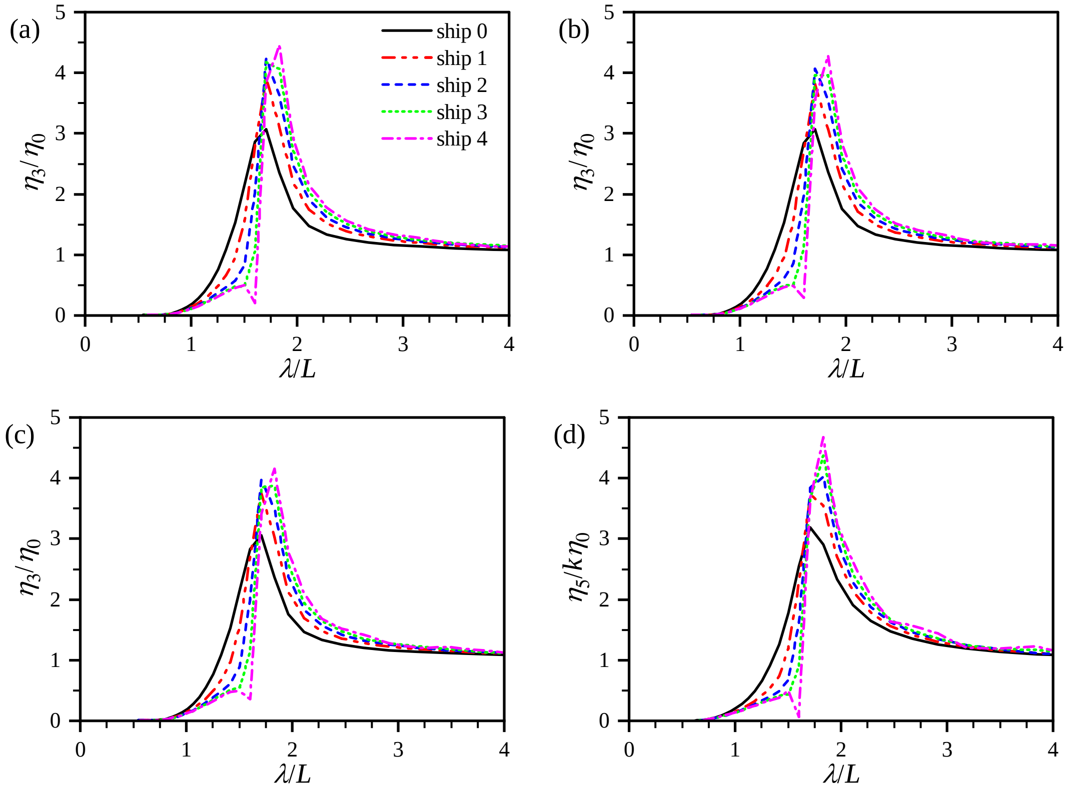

Figure 6.18: Heave motions for different gaps between ships at $F_r = 0.3$. (a) Gap = $0.1L$; (b) Gap = $0.2L$; (c) Gap = $0.3L$; (d) Gap = $0.4L$.

their motion responses by wave superposition or cancellation. In this analysis, the gaps considered range from $0.1L$ to $0.4L$ in increments of $0.1L$. Figures 6.18 and 6.19 illustrate the heave and pitch motions, respectively, for these varying gaps. The results indicate that the motion responses of the ships exhibit minimal variation across gaps $0.1L$, $0.2L$, and $0.3L$. This consistency is likely due to the relatively small difference in gap size compared to the wavelength. However, when the gap increases to $0.4L$, the magnitude of the heave motion increases compared to the other three gaps, while the magnitude of the pitch motion decreases. When designing a marine train with barges connected by joints, the gap between two ships should remain relatively small from an engineering perspective. As a result, the effect of gaps on ship motions is generally minimal, except in conditions with very short wavelengths, where the gap may have a more significant impact.

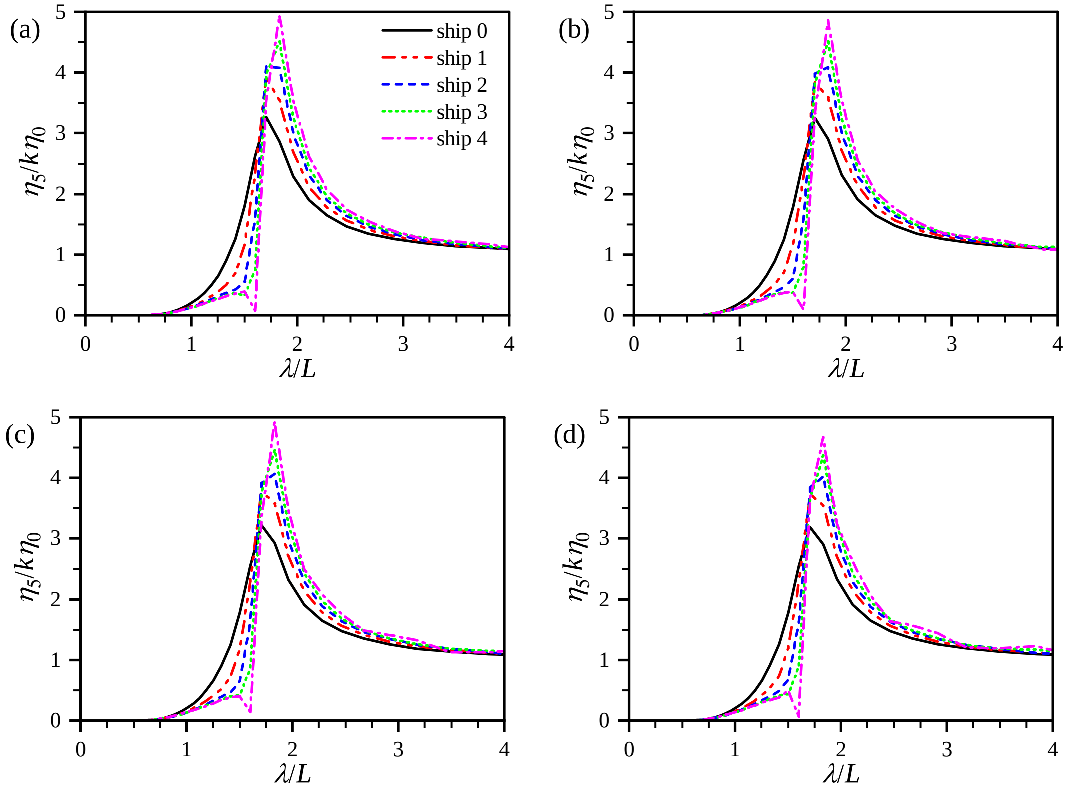

Figure 6.19: Pitch motions for different gaps between ships at $F_r = 0.3$. (a) Gap = $0.1L$; (b) Gap = $0.2L$; (c) Gap = $0.3L$; (d) Gap = $0.4L$.

6.6 Summary

This thesis analyzes the hydrodynamic response of marine trains in waves by extending the coupled motion equations for ships to include mechanical connections between carriages, utilizing the constraint matrix method. The approach is validated through two test cases: two hinged barges in head seas and single ships advancing in waves. The results show good agreement with previously published data. The key findings of the numerical simulations and analyses are summarized as follows:

(1) When two ships advance in a head sea with a free connection, the RAOs of the leading ship remain consistent with those of a single ship at the same speed, particularly at higher speeds. This is because the waves generated by the trailing ship have minimal impact on the wave field encountered by the leading ship.

Conversely, the RAOs of the trailing ship are significantly influenced by the waves generated by the leading ship.

(2) When two ships are connected by either a rigid or hinged joint, significant vertical shear forces can develop at the connection points, potentially damaging the joints.

(3) To release the vertical shear force at the joints, a sliding-hinged connection is employed to the marine train. In head sea conditions, the RAOs for both ships with a sliding-hinged connection are identical to those observed with a free connection. However, the advantage of the sliding-hinged connection is that it allows the leading ship to power the entire marine train, whereas a free connection system would require each unit to have its own power source.

(4) As the advancing speed increases, the RAOs of ships in a marine train rise significantly, particularly around the resonance zone.

(5) The installation position of the joints and the gap between the two ships have minimal effects on their motion responses in marine train configurations.

Chapter 7

Conclusions and Future Work

7.1 Conclusions

Ducklings swimming in a single-file formation can save energy by riding waves generated by the mother duck and passing waves to their siblings. Drawing inspiration from this phenomenon, this thesis investigated ships moving in a single-file formation. To investigate the hydrodynamic interactions among ships, an in-house code MHydro is utilised, integrating the boundary value technique and the Rankine source method within the framework of linearised potential flow theory. Additionally, a series of experiments are conducted to consider the viscous interference between ships.

The wave-riding and wave-passing mechanisms have been successfully applied to vessels moving in single file formation. When destructive wave interference occurs, both the leading and trailing ships can benefit from the wave-riding effect, reducing overall resistance. However, when constructive wave interference occurs, the leading ship may benefit at the expense of the trailing ship. The wave-passing can be achieved by maintaining uniform spacing between neighbouring vessels. However, there is a localized effect on wave-passing when the size of the leading vessel is changed or the position of the first trailing vessel is adjusted. Additionally, wave-passing can still be achieved when the trailing vessels move backward an integer number of wavelengths rather than occupying an optimal position.

The complex interference between ships moving in calm water includes not only wave interference but also viscous interference. A series of experiments are conducted to measure the resistance of ships moving individually and in formations. It is found that the trailing ship periodically benefits from wave interference while consistently gaining from viscous interference when moving in the wake of the leading ship. In addition, three critical zones are divided behind the transom stern. When two ships are in close proximity, the hydrostatic drag of both ships decreases significantly. With the gap between the two ships increasing, wave interference significantly affects the total drag. As the gap continues to widen, wave interference diminishes, making the reduction in form drag and frictional drag the dominant factor in the total drag reduction.

When ships are mechanically joined together, a marine train is constructed. Accurate prediction of the motion responses of marine trains in waves is crucial for ensuring both safety and operational efficiency. To achieve this, a two-step numerical approach is developed to conduct their hydrodynamic responses, initially solving the hydrodynamic interaction problem, followed by mechanical coupling using the constraint matrix method. The results showed that when two ships are either hinged or rigidly connected, the motion RAOs are significantly reduced compared to those of free ships; however, both connection types experience substantial vertical shear forces at the joints. In contrast, the sliding-hinged connection presents a viable solution for marine trains, as it does not increase motion responses while significantly reducing vertical shear forces. Moreover, the responses of a marine train configuration with five moving ships with sliding-hinged connections were analyzed to investigate the effect of advancing speed, joint position, and adjacent gap. The motion RAOs of the vessels increased significantly with rising advancing speed, while remaining relatively insensitive to variations in joint position and the gap between ships.

7.2 Future work

This thesis investigates the hydrodynamic interactions between ships in a single-file formation through the development of the MHydro code, based on potential theory, and supported by experimental research to account for viscous effects. However, several areas merit further exploration in future studies, including:

1. To improve the accuracy of predicting ship resistance and wave patterns, it is crucial to account for nonlinear free surface boundary conditions. Additionally, a comprehensive treatment of the m-term is necessary to accurately capture the coupled effects between steady and unsteady flow in seakeeping problems.

2. Future studies should utilize computational fluid dynamics (CFD) tools to calculate the total drag of ships, both with and without considering the propeller's wake effects.

3. In the experimental analysis, the resistance reduction effect remains significant when the trailing ship is positioned within the turbulent-bubble mixed region. Further experiments are needed to quantify the contributions of both bubble drag reduction and the reduction due to turbulent flow.

4. In the experiments, the ship models were fixed, but sinkage and trim motions may influence ship resistance and wave interference between two ships. It is essential to consider these effects by allowing for sinkage and trim motions in future experiments.

5. In the numerical study, viscous damping is not considered, which may impact the accuracy of motion response predictions, particularly near resonance. To address this, further CFD simulations should be conducted to provide viscous damping coefficients.

6. When designing a marine train, motion responses can be controlled by appropriately imposing stiffness and damping at the joints. It is important to explore the effects of stiffness and damping on the motions of the ships. Additionally, this concept could be further developed into a wave energy converter to provide power for ship devices.

Bibliography

Zhi-Ming Yuan, Minglu Chen, Laibing Jia, Chunyan Ji, and Atilla Incecik. Wave-riding and wave-passing by ducklings in formation swimming. *Journal of Fluid Mechanics*, 928:R2, 2021.

Zhi-Ming Yuan. Wave-passing by ships in a single file formation. In *Proceedings of the 37th International Workshop on Water Waves and Floating Bodies*. IWWWFB, 2022.

Simen Å Ellingsen. Getting the ducks in a row. *Journal of Fluid Mechanics*, 932:F1, 2022.

DARPA. Sea train. `https://www.darpa.mil/program/sea-train`, 2020.

ITTC. Report of skin friction and turbulence simulation. *Proceedings 8th International Towing Tank Conference*, 1957.

D Weihs. Hydromechanics of fish schooling. *Nature*, 241(5387):290–291, 1973.

James C Liao, David N Beal, George V Lauder, and Michael S Triantafyllou. Fish exploiting vortices decrease muscle activity. *Science*, 302(5650):1566–1569, 2003.

Daniel Weihs. The hydrodynamics of dolphin drafting. *Journal of Biology*, 3:1–16, 2004.

Liang Li, Máté Nagy, Jacob M Graving, Joseph Bak-Coleman, Guangming Xie, and Iain D Couzin. Vortex phase matching as a strategy for schooling in robots and in fish. *Nature communications*, 11(1):5408, 2020.

Robert M May. Flight formations in geese and other birds. *Nature*, 282(5741):778–780, 1979.

Dietrich Hummel. Aerodynamic aspects of formation flight in birds. *Journal of theoretical biology*, 104(3):321–347, 1983.

F Reed Hainsworth. Precision and dynamics of positioning by canada geese flying in formation. *Journal of Experimental Biology*, 128(1):445–462, 1987.

Christopher J Cutts and John R Speakman. Energy savings in formation flight of pink-footed geese. *Journal of experimental biology*, 189(1):251–261, 1994.

Malte Andersson and Johan Wallander. Kin selection and reciprocity in flight formation? *Behavioral Ecology*, 15(1):158–162, 2004.

Joo-Sung Maeng, Jae-Hyung Park, Seong-Min Jang, and Seog-Young Han. A modeling approach to energy savings of flying canada geese using computational fluid dynamics. *Journal of theoretical biology*, 320:76–85, 2013.

Steven J Portugal, Tatjana Y Hubel, Johannes Fritz, Stefanie Heese, Daniela Trobe, Bernhard Voelkl, Stephen Hailes, Alan M Wilson, and James R Usherwood. Upwash exploitation and downwash avoidance by flap phasing in ibis formation flight. *Nature*, 505(7483):399–402, 2014.

Frank E Fish. Energy conservation by formation swimming-metabolic evidence from ducklings. *Mechanics and physiology of animal swimming*, page 193, 1994.

Frank E Fish. Kinematics of ducklings swimming in formation: consequences of position. *Journal of Experimental Zoology*, 273(1):1–11, 1995.

B Bilodeau, B Roy, and MR Boulay. Effect of drafting on work intensity in classical cross-country skiing. *International journal of sports medicine*, 16(03):190–195, 1995.

GP Millet, R Geslan, R Ferrier, R Candau, and A Varray. Effects of drafting on energy expenditure in in-line skating. *Journal of sports medicine and physical fitness*, 43(3): 285–290, 2003.

Bert Blocken, Thijs Defraeye, Erwin Koninckx, Jan Carmeliet, and Peter Hespel. Cfd simulations of the aerodynamic drag of two drafting cyclists. *Computers & Fluids*, 71:435–445, 2013.

Bert Blocken, Thijs van Druenen, Yasin Toparlar, Fabio Malizia, Paul Mannion, Thomas Andrianne, Thierry Marchal, Geert-Jan Maas, and Jan Diepens. Aerodynamic drag in cycling pelotons: New insights by cfd simulation and wind tunnel testing. *Journal of Wind Engineering and Industrial Aerodynamics*, 179:319–337, 2018.

Guillaume Polidori, Fabien Legrand, Fabien Bogard, Farouk Madaci, and Fabien Beaumont. Numerical investigation of the impact of kenenisa bekele's cooperative drafting strategy on its running power during the 2019 berlin marathon. *Journal of Biomechanics*, 107:109854, 2020.

Hao Su, Haoran Meng, Timing Qu, and Liping Lei. Wind tunnel experiment on the influence of array configuration on the power performance of vertical axis wind turbines. *Energy Conversion and Management*, 241:114299, 2021.

Carlo Cossu. Replacing wakes with streaks in wind turbine arrays. *Wind Energy*, 24 (4):345–356, 2021.

AD De Andrés, R Guanche, L Meneses, C Vidal, and IJ Losada. Factors that influence array layout on wave energy farms. *Ocean Engineering*, 82:32–41, 2014.

Weixing Chen, Feng Gao, Xiangdun Meng, and Jianxun Fu. Design of the wave energy converter array to achieve constructive effects. *Ocean Engineering*, 124:13–20, 2016.

Pareecha Rattanasiri, Philip A Wilson, and Alexander B Phillips. Numerical investigation of a fleet of towed auvs. *Ocean Engineering*, 80:25–35, 2014.

Dong Zhang, Liming Chao, and Guang Pan. Analysis of hydrodynamic interaction impacts on a two-auv system. *Ships and Offshore Structures*, 14(1):23–34, 2019.

Yangying He, Junmin Mou, Linying Chen, Qingsong Zeng, Yamin Huang, Pengfei Chen, and Song Zhang. Will sailing in formation reduce energy consumption? numerical prediction of resistance for ships in different formation configurations. *Applied Energy*, 312:118695, 2022.

Zhenpeng Dong, Xiao Liang, Xiawei Guan, and Wei Li. Formation optimization of various spacing configurations for a fleet of unmanned surface vehicles based on a hydrodynamic energy-saving strategy. *Ocean Engineering*, 266:112824, 2022.

Chao Ma, Xiaosa Zhao, Xide Cheng, Yuntao Yang, and Li Fan. The wave interference and the wave drag of a leader–follower ship fleet. *Ocean Engineering*, 274:114089, 2023.

Zhengyuan Liu, Changming Dai, Xiaohui Cui, Yu Wang, Hui Liu, and Bo Zhou. Hydrodynamic interactions between ships in a fleet. *Journal of Marine Science and Engineering*, 12(1):56, 2023.

William Froude and Edmund Froude. *The resistance of ships.* Number 23. US Government Printing Office, 1888.

John Henry Michell. Xi. the wave-resistance of a ship. *The London, Edinburgh, and Dublin Philosophical Magazine and Journal of Science*, 45(272):106–123, 1898.

WCS Wigley. Ship wave resistance. a comparison of mathematical theory with experimental results. *Trans. Inst. Nav. Architects*, 68:124–137, 1926.

Thomas Henry Havelock. The theory of wave resistance. *Proceedings of the Royal Society of London. Series A, Containing Papers of a Mathematical and Physical Character*, 138(835):339–348, 1932.

Georg Weinblum. Applications of wave resistance theory to problems of ship design. Technical report, 1959.

R Guilloton. L'étude théorique du bateau en fluide parfait. *Bull. Assoc. Tech. Maritime Aero. 64, 537*, 552, 1964.

John V Wehausen. *Use of Lagrangian Coordinates for Ship Wave Resistance:(first-and Second-order Thin-ship Theory).* University of California, College of Engineering, 1967.

Chi-Chao Hsiung. Optimal ship forms for minimum wave resistance. *Journal of Ship Research*, 25(02):95–116, 1981.

Francis Noblesse, Gerard Delhommeau, Hyun Yul Kim, and Chi Yang. Practical green function for thin-ship theory. In *ISOPE International Ocean and Polar Engineering Conference*, pages ISOPE–I. ISOPE, 2008.

Ernest O Tuck. The wave resistance formula of jh michell (1898) and its significance to recent research in ship hydrodynamics. *The ANZIAM Journal*, 30(4):365–377, 1989.

A Kriloff. A new theory of the pitching motion of ships on waves, and of the stresses produced by this motion. *(No Title)*, 1896.

Georg Weinblum and M St Denis. On the motions of ships at sea. *David W Taylor Model Basin, Navy Department, Paper 2 of The Society of Naval Architects and Marine Engineers, SNAME Transactions, 1950, Paper: T1950-1 Transactions.*, 1950.

Winnifred R Jacobs, J Dalzell, and P Lalangas. Guide to computational procedure for analytical evaluation of ship bending-moments in regular waves. Technical report, Stevens Institute of Technology, 1960.

T Francis Ogilvie and Ernest O Tuck. A rational strip theory of ship motions: part i. Technical report, University of Michigan, 1969.

Odd Faltinsen. A rational strip theory of ship motions: Part ii. Technical report, University of Michigan, 1971.

R Beck. Motions in waves. *Principles of naval architecture*, 1989.

Volker Bertram. *Practical ship hydrodynamics*. Elsevier, 2011.

John Nicholas Newman. *Marine hydrodynamics*. The MIT press, 2018.

John Nicholas Newman. A slender-body theory for ship oscillations in waves. *Journal of Fluid Mechanics*, 18(4):602–618, 1964.

John L Hess and Apollo Milton Olin Smith. Calculation of nonlifting potential flow about arbitrary three-dimensional bodies. *Journal of ship research*, 8(04):22–44, 1964.

F Thomas Korsmeyer, C-H Lee, and JN Newman. Computation of ship interaction forces in restricted waters. *Journal of Ship Research*, 37(04):298–306, 1993.

Jo A Pinkster. The influence of a free surface on passing ship effects. *International Shipbuilding Progress*, 51(4):313–338, 2004.

Xu Xiang and Odd M Faltinsen. Maneuvering of two interacting ships in calm water. *Marine Systems & Ocean Technology*, 6:65–73, 2011a.

Xueqian Zhou, Serge Sutulo, and C Guedes Soares. Computation of ship hydrodynamic interaction forces in restricted waters using potential theory. *Journal of Marine Science and Application*, 11(3):265–275, 2012.

Zhi-Ming Yuan, Atilla Incecik, Saishuai Dai, Day Alexander, Chun-Yan Ji, and Xinshu Zhang. Hydrodynamic interactions between two ships travelling or stationary in shallow waters. *Ocean Engineering*, 108:620–635, 2015.

Hamid Sadat-Hosseini, Ping-Chen Wu, Pablo M Carrica, Ho Kim, Yasuyuki Toda, and Frederick Stern. Cfd verification and validation of added resistance and motions of kvlcc2 with fixed and free surge in short and long head waves. *Ocean Engineering*, 59:240–273, 2013.

Ruosi Zha, Haixuan Ye, Zhirong Shen, and Decheng Wan. Numerical study of viscous wave-making resistance of ship navigation in still water. *Journal of Marine Science and Application*, 13(2):158–166, 2014.

Malte Riesner and Ould el Moctar. A time domain boundary element method for wave added resistance of ships taking into account viscous effects. *Ocean Engineering*, 162: 290–303, 2018.

Momchil Terziev, Tahsin Tezdogan, and Atilla Incecik. A geosim analysis of ship resistance decomposition and scale effects with the aid of cfd. *Applied Ocean Research*, 92:101930, 2019.

A Olivieri, F Pistani, A Avanzini, F Stern, and R Penna. Towing tank experiments of resistance, sinkage and trim, boundary layer, wake, and free surface flow around a naval combatant insean 2340 model. 2006.

Soizic Annick Gabrielle Joncquez, Harry Bingham, Poul Andersen, and David Kring. Validation of added resistance computations by a potential flow boundary element method. In *27th Symposium on Naval Hydrodynamics, Seoul, Korea*, pages 1400–1410, 2008.

Ould el Moctar, Sebastian Sigmund, Jens Ley, and Thomas E Schellin. Numerical and experimental analysis of added resistance of ships in waves. *Journal of Offshore Mechanics and Arctic Engineering*, 139(1):011301, 2017.

Masashi Kashiwagi, Hidetsugu Iwashita, Soma Miura, and Munehiko Hinatsu. Study on added resistance with measured unsteady pressure distribution on ship-hull surface. *Proceedings of 34th IWWWFB (Noah's on the Beach, Newcastle, NSW, Australia)*, pages 81–84, 2019.

JN Newman. The determination of wave resistance from wave measurement along a parallel cut. In *International Seminar on Theoretical Wave Resistance, Ann Arbor, Michigan*, 1963.

KWH Eggers. An assessment of some experimental methods for determining the wavemaking characteristics of a ship form. *Sname Transactions*, 75:112–157, 1967.

DD Moran and L Landweber. A longitudinal-cut method for determining wavemaking resistance. *Journal of Ship Research*, 16(01):21–40, 1972.

C-E Tsai and L Landweber. Further development of a procedure for determination of wave resistance from longitudinal-cut surface-profile measurements. *Journal of Ship Research*, 19(02):65–75, 1975.

F Lalli, F Di Felice, P Esposito, A Moriconi, and R Piscopia. Some remarks on the accuracy of wave resistance determination from wave measurements along a parallel cut. In *Proceedings, 22nd Symposium on Naval Hydrodynamics, Washington, DC, August*, pages 9–14, 1998.

F Lalli, F Di Felice, PG Esposito, A Moriconi, and R Piscopia. Longitudinal cut method revisited: A survey on main error sources. *Journal of ship research*, 44(02):120–139, 2000.

Karl Ernest Schoenherr. Resistance of flat surfaces moving through a fluid. *Trans. Soc. Nav. Arch. Mar. Eng.*, pages 279–313, 1932.

GRIGSON CWB. A planar friction algorithm and its use in analysing hull resistance. *Trans RINA*, 1999.

Tokihiro Katsui. The proposal of a new friction line. In *Fifth Osaka colloquium on advanced CFD applications to ship flow and hull form design, Osaka, Japan, 2005*, 2005.

Odd M Faltinsen. *Hydrodynamics of high-speed marine vehicles*. Cambridge university press, 2005.

G Hughes. Friction and form resistance in turbulent flow, and a proposed formulation for use in model and ship correlation. *National Physical Laboratory, NPL, Ship Division, Presented at the Institution of Naval Architects, Paper No. 7, London, April, RINA Transactions 1954-16*, 1954.

ITTC. Report of performance committee. *Proceedings 15th International Towing Tank Conference*, 1978.

MB Wilson, CC Hsu, and DS Jenkins. Experiments and predictions of the resistance characteristics of a wave cancellation multihull ship concept. In *SNAME American Towing Tank Conference*, page D011S004R001. SNAME, 1992.

Kazuo Suzuki and Mitsuhisa Ikehata. Studies on minimization of wave making resistance for high speed trimaran with small outriggers. *Journal of the Society of Naval Architects of Japan*, 1995(177):113–122, 1995.

Ernest O Tuck and Leo Lazauskas. Optimum hull spacing of a family of multihulls. *Ship Technology Research-Schiffstechnik*, 45(4):180, 1998.

Hongxuan Peng. Numerical computation of multi-hull ship resistance and motion. 2001.

Dongchi Yu, Pierre Lecointre, and Ronald W Yeung. Experimentally-based investigation of effects of wave interference on the wave resistance of asymmetric di-hulls. *Applied Ocean Research*, 65:142–153, 2017.

Burak Yildiz, Bekir Sener, Suleyman Duman, and Raju Datla. A numerical and experimental study on the outrigger positioning of a trimaran hull in terms of resistance. *Ocean Engineering*, 198:106938, 2020.

H Soding. Drastic resistance reduction in catamarans of staggered hulls. *Proceedings of FAST97*, 1997.

Ronald W Yeung and Hui Wan. Multihull and surface-effect ship configuration design: a framework for powering minimization. 2008.

Stefano Zaghi, Riccardo Broglia, and Andrea Di Mascio. Analysis of the interference effects for high-speed catamarans by model tests and numerical simulations. *Ocean Engineering*, 38(17-18):2110–2122, 2011.

Riccardo Broglia, Boris Jacob, Stefano Zaghi, Frederick Stern, and Angelo Olivieri. Experimental investigation of interference effects for high-speed catamarans. *Ocean Engineering*, 76:75–85, 2014.

Wei He, Teresa Castiglione, Manivannan Kandasamy, and Frederick Stern. Numerical analysis of the interference effects on resistance, sinkage and trim of a fast catamaran. *Journal of marine science and technology*, 20:292–308, 2015.

Ronald W Yeung, Gregoire Poupard, Jean O Toilliez, Heinrich SÖDING, A Sh Gotman, and Hendrik F VAN HEMMEN. Interference-resistance prediction and its applications to optimal multi-hull configuration design. discussion. *Transactions-Society of Naval Architects and Marine Engineers*, 112:142–168, 2004.

Thomas Mynard, Prasanta K Sahoo, Jon Mikkelsen, and Dan McGreer. Numerical and experimental study of wave resistance for trimaran hull forms. *Australian Maritime College, Australia*, pages 117–132, 2008.

SM Wang, WY Duan, QL Xu, F Duan, GZ Deng, and Y Li. Study on fast interference wave resistance optimization method for trimaran outrigger layout. *Ocean Engineering*, 232:109104, 2021.

Amin Nazemian and Parviz Ghadimi. Cfd-based optimization of a displacement trimaran hull for improving its calm water and wavy condition resistance. *Applied Ocean Research*, 113:102729, 2021.

LJ Doctors and RF Beck. The separation of the flow past a transom stern. In *First International Conference on Marine Research and Transportation (ICMRT'05), Ischia, Italy*, 2005.

Kevin J Maki, Lawrence J Doctors, Robert F Beck, and Armin W Troesch. Transom-stern flow for high-speed craft. *Australian Journal of Mechanical Engineering*, 3(2): 191–199, 2006.

Lawrence J Doctors. Influence of the transom-hollow length on wave resistance. In *International Workshop on Water Waves and Floating Bodies*, volume 21, 2006.

Lawrence J Doctors and University of New South Wales. A numerical study of the resistance of transom-stern monohulls. *Ship Technology Research*, 54(3):134–144, 2007.

Kevin J Maki, Lawrence J Doctors, and R Beck. On the profile of the flow behind a transom stern. In *9th Int. Conf. on Num. Ship Hydrodynamics, Ann Arbor, Michigan*, 2007.

Marshall P Tulin and CC Hsu. Theory of high-speed displacement ships with transom sterns. *Journal of ship research*, 30(03):186–193, 1986.

Dimitris E Nakos and PD Sclavounos. Kelvin wakes and wave resistance of cruiser-and transom-stern ships. *Journal of Ship Research*, 38(01):9–29, 1994.

Andrea Mola, Luca Heltai, and Antonio DeSimone. Wet and dry transom stern treatment for unsteady and nonlinear potential flow model for naval hydrodynamics simulations. *Journal of Ship Research*, 61(01):1–14, 2017.

Kelli Hendrickson, Gabriel D Weymouth, Xiangming Yu, and Dick K-P Yue. Wake behind a three-dimensional dry transom stern. part 1. flow structure and large-scale air entrainment. *Journal of Fluid Mechanics*, 875:854–883, 2019.

Kelli Hendrickson and Dick K-P Yue. Wake behind a three-dimensional dry transom stern. part 2. analysis and modelling of incompressible highly variable density turbulence. *Journal of Fluid Mechanics*, 875:884–913, 2019.

Eric J Terrill and Genevieve RL Taylor. Entrainment of air at the transoms of full-scale surface ships. *Journal of Ship Research*, 59(01):49–65, 2015.

Mohammad Abbaszadeh, Mohammad Mehdi Alishahi, and Homayoun Emdad. Experimental investigations on the bubbly wake of a transom stern model using optical laser beam scattering characteristics. *Applied Ocean Research*, 104:102380, 2020.

Steven L Ceccio. Friction drag reduction of external flows with bubble and gas injection. *Annual Review of Fluid Mechanics*, 42(1):183–203, 2010.

Xiaosong Zhang, Jianhua Wang, and Decheng Wan. Euler–lagrange study of bubble drag reduction in turbulent channel flow and boundary layer flow. *Physics of Fluids*, 32(2), 2020.

Hiroharu Kato, Tomoaki Iwashina, Masaru Miyanaga, and Hajime Yamaguchi. Effect of microbubbles on the structure of turbulence in a turbulent boundary layer. *Journal of Marine Science and Technology*, 4:155–162, 1999.

Yassin A Hassan, Claudia C Gutierrez-Torres, and Jose A Jimenez-Bernal. Temporal correlation modification by microbubbles injection in a channel flow. *International communications in heat and mass transfer*, 32(8):1009–1015, 2005.

Javier Ortiz-Villafuerte and Yassin A Hassan. Investigation of microbubble boundary layer using particle tracking velocimetry. 2006.

Ichiro Kumagai, Yoshiaki Takahashi, and Yuichi Murai. Power-saving device for air bubble generation using a hydrofoil to reduce ship drag: Theory, experiments, and application to ships. *Ocean Engineering*, 95:183–194, 2015.

Yuichi Murai, Haruki Sakamaki, Ichiro Kumagai, Hyun Jin Park, and Yuji Tasaka. Mechanism and performance of a hydrofoil bubble generator utilized for bubbly drag reduction ships. *Ocean Engineering*, 216:108085, 2020.

Wendy C Sanders, Eric S Winkel, David R Dowling, Marc Perlin, and Steven L Ceccio. Bubble friction drag reduction in a high-reynolds-number flat-plate turbulent boundary layer. *Journal of Fluid Mechanics*, 552:353–380, 2006.

Brian R Elbing, Eric S Winkel, Keary A Lay, Steven L Ceccio, David R Dowling, and Marc Perlin. Bubble-induced skin-friction drag reduction and the abrupt transition to air-layer drag reduction. *Journal of Fluid Mechanics*, 612:201–236, 2008.

Keary A Lay, Ryo Yakushiji, Simo Makiharju, Marc Perlin, and Steven L Ceccio. Partial cavity drag reduction at high reynolds numbers. *Journal of Ship Research*, 54(02):109–119, 2010.

RS Langley. Random dynamic analysis of multi-body offshore structures. *Ocean engineering*, 11(4):381–401, 1984.

Mícheál Ó'Catháin, Bernt J Leira, John V Ringwood, and Jean-Christophe Gilloteaux. A modelling methodology for multi-body systems with application to wave-energy devices. *Ocean Engineering*, 35(13):1381–1387, 2008.

Liang Sun, R Eatock Taylor, and Yoo Sang Choo. Responses of interconnected floating bodies. *The IES Journal Part A: Civil & Structural Engineering*, 4(3):143–156, 2011.

BJ Koo and MH Kim. Hydrodynamic interactions and relative motions of two floating platforms with mooring lines in side-by-side offloading operation. *Applied Ocean Research*, 27(6):292–310, 2005.

Liang Sun, R Eatock Taylor, and Yoo Sang Choo. Multi-body dynamic analysis of float-over installations. *Ocean Engineering*, 51:1–15, 2012.

XY Feng and W Bai. Hydrodynamic analysis of marine multibody systems by a nonlinear coupled model. *Journal of Fluids and Structures*, 70:72–101, 2017.

Wei Huang, Binbin Li, Xiaobo Chen, and Rodrigo Araujo. Numerical and experimental studies on dynamic gangway response between monohull flotel and fpso in non-parallel side-by-side configuration. *Ocean Engineering*, 149:341–357, 2018.

John Nicholas Newman. Wave effects on deformable bodies. *Applied ocean research*, 16 (1):47–59, 1994.

C-H Lee and JN Newman. An assessment of hydroelasticity for very large hinged vessels. *Journal of fluids and structures*, 14(7):957–970, 2000.

Reza Taghipour and Torgeir Moan. Efficient frequency-domain analysis of dynamic response for the multi-body wave energy converter in multi-directional wave. In *ISOPE International Ocean and Polar Engineering Conference*, pages ISOPE–I. ISOPE, 2008.

SY Hong, JH Kim, SK Cho, YR Choi, and YS Kim. Numerical and experimental study on hydrodynamic interaction of side-by-side moored multiple vessels. *Ocean Engineering*, 32(7):783–801, 2005.

RP Gao, ZY Tay, CM Wang, and CG Koh. Hydroelastic response of very large floating structure with a flexible line connection. *Ocean Engineering*, 38(17-18):1957–1966, 2011.

Nianxin Ren, Chi Zhang, Allan Ross Magee, Øyvind Hellan, Jian Dai, and Kok Keng Ang. Hydrodynamic analysis of a modular multi-purpose floating structure system with different outermost connector types. *Ocean Engineering*, 176:158–168, 2019.

IBS Bispo, SC Mohapatra, and C Guedes Soares. Numerical analysis of a moored very large floating structure composed by a set of hinged plates. *Ocean Engineering*, 253: 110785, 2022.

Deqing Zhang, Junfeng Du, Zhiming Yuan, Shuangrui Yu, and Huajun Li. Motion characteristics of large arrays of modularized floating bodies with hinge connections. *Physics of Fluids*, 35(7), 2023.

Zhiqiang Li, Dengshuo Chen, and Xingya Feng. Hydroelastic and expansibility analysis of a modular floating photovoltaic system with multi-directional hinge connections. *Ocean Engineering*, 289:116218, 2023.

E.M. Anderson. Seasnake: A versatile concept. *www.seasnake.net*, 2013.

Robert Brown and Nicole Runyon. A study of energy efficiency in articulating tug and barge design. 2022.

Amitava Guha, Abhilash Somayajula, and J Falzarano. Analysis of causeway ferry dynamics for safe operation of improved navy lighterage system. In *Proceedings of the 13th International Ship Stability Workshop*, pages 1–8, 2013.

Gabor Karafiath, Bryson Metcalf, and Jesse Geisbert. Seatrain for high-capacity high-speed ocean transport. In *Proceedings of FAST 2009, International Conference on Fast Sea Transportation*, 2009.

Igor Mizine and Gabor Karafiath. Model test evaluation of high speed trimaran (hst) sea train concept. In *SNAME International Conference on Fast Sea Transportation*, page D011S003R004. SNAME, 2015.

Li Zhang, Lei Xing, Mingyu Dong, and Weimin Chen. Resistance tests of an articulated pusher barge system in deep and shallow water. In *International Conference on Offshore Mechanics and Arctic Engineering*, volume 85161, page V006T06A035. American Society of Mechanical Engineers, 2021.

David K Mumford. *Vertical forces on the coupling of a pusher tug-barge*. PhD thesis, University of British Columbia, 1993.

AD Miller, J Barbosa, and R Latorre. Analysis of tug-barge connection force measurements. *Marine technology and SNAME news*, 38(02):130–137, 2001.

Yan Qin, Qing Wang, Guohua Dong, Chaobang Yao, and Dakui Feng. Hydrodynamic performance of a conceptional seatrain in heading wave based on small water plane area trimaran. In *International Conference on Offshore Mechanics and Arctic Engineering*, volume 86878, page V005T06A082. American Society of Mechanical Engineers, 2023.

Zhi-Ming Yuan, Liang Li, and Ronald W Yeung. Free-surface effects on interaction of multiple ships moving at different speeds. *Journal of Ship Research*, 63(04):251–267, 2019.

Odd Faltinsen. *Sea loads on ships and offshore structures*, volume 1. Cambridge university press, 1993.

Lin Li. Numerical seakeeping predictions of shallow water effect on two ship interactions in waves. 2001.

Yoshiyuki Inoue and Md Kamruzzaman. Analysis of hydrodynamic characteristics for arbitrary multihull ships advancing in waves. *Journal of marine science and technology*, 13:231–243, 2008.

MC Fang and CH Kim. Hydrodynamically coupled motions of two ships advancing in oblique waves. *Journal of Ship Research*, 30(03):159–171, 1986.

Larry L Erickson. Panel methods: An introduction. Technical report, 1990.

Alexander von Graefe, Vladimir Shigunov, and Ould el Moctar. Rankine source method for ship–ship interaction problems. *Journal of Offshore Mechanics and Arctic Engineering*, 137(2):021601, 2015.

Yifeng Huang. *Nonlinear ship motions by a Rankine panel method.* PhD thesis, Massachusetts Institute of Technology, 1997.

T Bunnik. Seakeeping calculations for ships, taking into account the non-linear steady waves. *PhD Thesis, Technical University Delft*, 1999.

Zhi-Ming Yuan. Hydrodynamic interaction between ships travelling or stationary in shallow waters. *PhD Thesis, University of Strathclyde*, 2014.

Arnold Sommerfeld. *Partial differential equations in physics.* Academic press, 1949.

Suvabrata Das and Kwok Fai Cheung. Scattered waves and motions of marine vessels advancing in a seaway. *Wave Motion*, 49(1):181–197, 2012.

Zhi-Ming Yuan, Atilla Incecik, and Laibing Jia. A new radiation condition for ships travelling with very low forward speed. *Ocean Engineering*, 88:298–309, 2014.

Johan MJ Journee. Experiments and calculations on four wigley hullforms. *TUDelft, Faculty of Marine Technology, Ship Hydromechanics Laboratory, Report No. 909*, 1992.

Xu Xiang and Odd M Faltinsen. Time domain simulation of two interacting ships advancing parallel in waves. In *International Conference on Offshore Mechanics and Arctic Engineering*, volume 44380, pages 357–369, 2011b.

ITTC. In *Proceedings of the 17th ITTC Conference Resistance Committee*, 1984.

Francis Noblesse, Fuxin Huang, and Chi Yang. The neumann–michell theory of ship waves. *Journal of Engineering Mathematics*, 79(1):51–71, 2013.

Yonghwan Kim, Dick KP Yue, and Benjamin SH Connell. Numerical dispersion and damping on steady waves with forward speed. *Applied Ocean Research*, 27(2):107–125, 2005.

Thomas Henry Havelock. The propagation of groups of waves in dispersive media, with application to waves on water produced by a travelling disturbance. *Proceedings of the Royal Society of London. Series A, Containing Papers of a Mathematical and Physical Character*, 81(549):398–430, 1908.

Keh-Sik Min and Seon-Hyung Kang. Study on the form factor and full-scale ship resistance prediction method. *Journal of marine science and technology*, 15:108–118, 2010.

Mustafa Insel. *An investigation into the resistance components of high speed displacement catamarans.* PhD thesis, University of Southampton, 1990.

Kenneth M Forgach and NAVAL SURFACE WARFARE CENTER CARDEROCK DIV BETHESDA MD. Measurement uncertainty analysis of ship model resistance and self propulsion tests. *Technical Re-port NSWCCD-50-TR-2002/064, Naval Surface Warfare Center Carderock Division, West Bethesda, Maryland, USA*, 2002.

Fred Stern. Summary of experimental uncertainty assesment methodology with example. *IIHR Technical Report No. 406*, 1999.

Shengtao Chen, Tianyu Su, Hao Guo, Yuhan Zhang, and Han Zou. Study of "whitewater zone" optical properties in ship wake. *Ocean Engineering*, 297:117060, 2024.

Harold E Saunders. Hydrodynamics in ship design, volume one. *Captain US Navy, Published by: The Society of Naval Architects and Marine Engineering, SNAME, New York, USA*, 1957.

Lawrence J Doctors. On the great trimaran-catamaran debate. In *Proceedings of the 5th International Conference on Fast Sea Transportation, FAST'99, Seattle, Washington, USA, August 1999*, 1999.

Yasuharu Nakamura and Shigehira Ozono. The effects of turbulence on a separated and reattaching flow. *Journal of Fluid Mechanics*, 178:477–490, 1987.

Ahmed A Shabana. *Computational dynamics.* John Wiley & Sons, 2009.

Alexandre Michailovich Vinogradov and Iosif Semenovich Krasil'shchik. What is the hamiltonian formalism? *Russian mathematical surveys*, 30(1):177, 1975.